Università degli Studi di Palermo

AREA RICERCA E TRASFERIMENTO TECNOLOGICO
SETTORE DOTTORATI E CONTRATTI PER LA RICERCA
U. O. DOTTORATI DI RICERCA

PhD School of Biomedicine, Neurosciences, and Advanced Diagnostics
Dipartimento di Biomedicina Neuroscienze e Diagnostica Avanzata
Settore di Biologia Cellulare e Applicata BIOS-10/A

UNRAVELLING THE ROLE OF COLORECTAL CANCER DERIVED EXTRACELLULAR VESICLES IN DRIVING HEPATOCYTES TO ACTIVELY SHAPE HEPATIC PRE-METASTATIC NICHE: FROM *IN VITRO* INSIGHTS TO *IN VIVO* EVALUATION.

IL DOTTORE
Elisa Costanzo

IL COORDINATORE
Prof. Fabio Bucchieri

IL TUTOR
Prof.ssa Simona Fontana

CICLO XXXVIII
ANNO CONSEGUIMENTO TITOLO 2026

Summary

ABSTRACT

Colorectal cancer (CRC) is one of the leading causes of cancer-related deaths worldwide, with liver metastases representing the major cause of mortality. A crucial step preceding metastasis formation is the establishment of the hepatic pre-metastatic niche (h-PMN), a supportive microenvironment actively shaped by soluble factors released by the primary tumor, including CRC-derived small extracellular vesicles (CRC-sEVs). While much of the research to date has focused on the impact of CRC-sEVs on non-parenchymal liver cells, such as hepatic stellate cells, Kupffer cells, endothelial sinusoidal cells, and infiltrating macrophages, the contribution of hepatocytes (Heps), the liver's main parenchymal and functional cell population, remains underexplored in this context.

This project aims to unravel the multifaceted role of Heps educated by CRC-sEVs in the early stages of liver metastasis formation. First, we investigated the immunomodulatory effects of CRC-sEVs on THLE-2. Our results revealed that the CRC-sEVs' treatment induced in Heps a rapid increase of the nuclear form of the checkpoint inhibitor protein PD-L1, which, consistent with literature data, was associated with the upregulation of the alternative immunecheckpoint proteins VISTA and PD-L2. The presence of PD-L1 protein within CRC-sEVs and the absence of its regulation at mRNA level in the target cells, suggested that the observed effects were due to a sEV-mediated mechanism of nuclear delivery. This hypothesis was confirmed by exposing Heps to CRC-sEVs carrying a tagged PD-L1, which was specifically detected in the treated Heps' nuclei. According to this observation, the inhibition of nuclear import pathways of the sEV cargo abolished in the Heps the effects elicited by the CRC-sEVs treatment.

Subsequently, we addressed the pro-fibrotic potential of CRC-sEVs-educated Heps, given the crucial role of fibrosis within h-PMN establishment, by using an innovative three-dimensional (3D) Heps spheroid model. Unlike traditional 2D cultures, which require collagen or fibronectin coatings that may bias fibrosis studies, the 3D model provides a physiologically relevant system that better preserves Heps morphology and intercellular interactions. This allowed us to more accurately assess CRC-sEVs-induced fibrotic transformations, including epithelial-mesenchymal transition (EMT) and extracellular matrix (ECM) remodeling.

Finally, to validate the Heps contribution to h-PMN formation *in vivo*, we developed a zebrafish CRC xenograft model, offering a transparent, cost-effective, and ethically advantageous platform in accordance with the 3Rs (Reduction, Refinement, Replacement) and enabling real-time imaging of CRC-sEVs interactions and metastatic niche development within the liver.

Overall, this project provides new evidence for a previously underestimated role of Heps in PMN formation. By dissecting both the immunomodulatory and profibrotic roles of CRC-sEVs-educated Heps, and developing alternative models, namely spheroids and zebrafish larval xenografts to validate these findings, this work opens new avenues for early intervention and therapeutic targeting of liver metastasis in CRC.

CHAPTER 1 – Colorectal Cancer

1.1 Colorectal Cancer epidemiology and etiology

Colorectal cancer (CRC) is a type of cancer affecting the colon or rectum, belonging to the large intestine, the last part of the digestive system. According to the World Health Organization (WHO), CRC is the third most common cancer type worldwide, accounting for 9.6% of all cancer cases and is the second leading cause of cancer-related death. In the past years CRC incidence rates have been decreasing in high-income countries, as a result of effective screening programs. However, CRC is still accountable for more than 900.000 deaths per years. Although the etiology of CRC is still to unravel, it is related to some key factors, as described in *Table 1*.

Modifiable risk factors		**Non-modifiable** risk factors	
Excess body weight	[1]	Age	[2]
Diabetes mellitus, Type 2	[3]	Gender	[4]
Dietary factors	[5]	Race and ethnic background	[6]
Smoke and alcohol	[7] [8]	Genetic factors	[9]

Table 1 – Modifiable and non-modifiable risk factors for CRC.

1.2 Colorectal cancer histopathological classification

Before describing the staging and scoring system of CRC, it's important to disclose the structure of the colon or rectum wall. This structure includes several layers:

1. ***Mucosa***, the inner most layer, which includes:
    - ***Epithelium***, where the glandular epithelial cells can be found. These cells include several specialized subtypes such as Absorptive cells, responsible for water and electrolytes absorption, Goblet cells, involved in mucins secretion, Enteroendocrine cells, which secrete hormones like serotonin, somatostatin, and others to regulate motility and secretions, Paneth cells, with antimicrobial funcitonal which can be rarely found in colon, and Tuft cells, rare cells involved in immune signaling. In addition to the epithelial columnar cells just mentioned it its possible to find only in the distal rectum keratinized and non-keratinized squamous cells. In the epithelium

it is possible to observe some invaginations, extending deep into the mucosa, defined as crypts of Lieberkühn, and at the base of those crypts, we find Stem cells, continuously regenerating the epithelium.

- ***Lamina propria,*** the connective tissue below the epithelium, where it is possible to find fibroblast, immune cells (T cells, B cells, macrophages, dendritic cells, plasma cells and innate lymphoid cells), and endothelial cells.
- ***Muscolaris mucosae***, a thin muscle layer where smooth muscle cells can be found.

2. ***Submucosa***, a fibrous tissue right beneath the *mucosa*, where fibroblast, immune cells, endothelial cells, and enteric nerves from the submucosal plexus (Meissner's plexus) can be found.
3. ***Muscolaris propria***, a thick muscle layer, characterized by inner circular and outer longitudinal smooth muscle cells, and the myenteric plexus (Auerbach's plexus), consisting in enteric neurons and glial cells.
4. ***Subserosa***, loose connective tissue mainly characterized by fibroblast and adipocytes.
5. ***Serosa***, the outermost layers of connective tissue, that cover most of the colon but not the rectum, consisting in a layer of simple squamous epithelium (mesothelial cells).
6. ***Adventitia,*** the outermost layer of connecting tissue that covers the distal rectum.

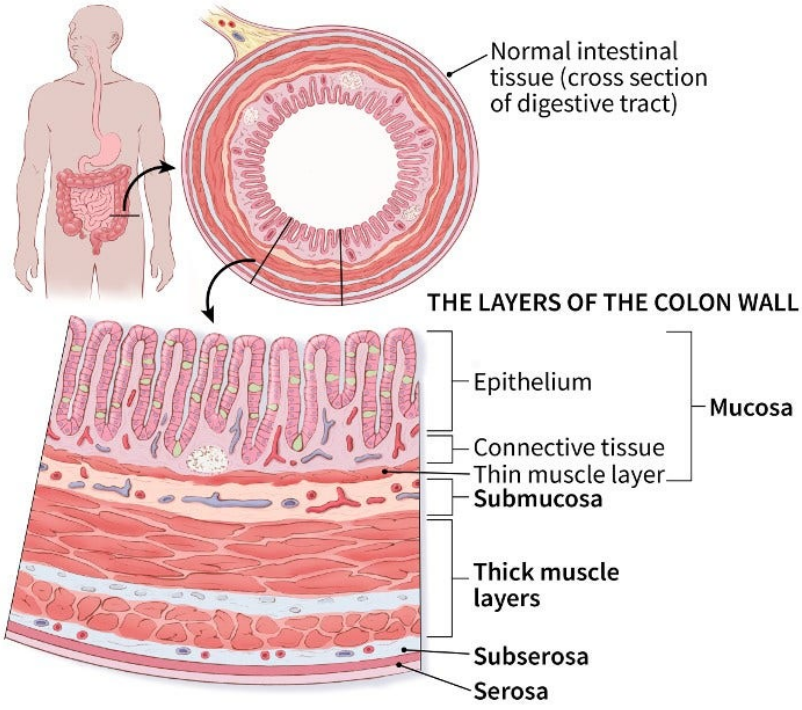

Figure 1 – Representative image of the different layers of the colon wall of normal intestinal tissue; Source: American Cancer Society (*https://www.cancer.org/cancer/types/colon-rectal-cancer/detection-diagnosis-staging/staged.html)*.

CRC is divided in several histopathological types and subtypes:

1. **Adenocarcinoma**, the most common type of CRC accounting for more than 90% of CRC cases [10]. It originates from glandular epithelial cells and can be divided in several histological subtypes:

- *Cribriform-comedo carcinoma*, characterized by cribriform (sieve-like) glandular structures with central necrosis (comedo-type), often aggressive.
- *Medullary carcinoma*, a rare subtype with sheets of poorly differentiated cells, often associated with microsatellite instability and better prognosis.
- *Micropapillary carcinoma*, characterized by small clusters of tumor cells within clear spaces, often associated to high invasiveness and poor prognosis.
- *Mucinous carcinoma*, which contains abundant extracellular mucin (>50% of the tumor), typically associated with worse response to therapy.
- *Serrated carcinoma*, which starts from serrated polyps, with a saw-tooth glandular pattern and often linked to specific genetic mutations.

- *Signet ring carcinoma*, characterized by cells containing mucin pushing the nucleus to the periphery, a rare and aggressive variant.

2. **Squamous cell carcinoma**, arising from squamous cells, which are not very common in the colorectal mucosa, making this type of CRC rare.
3. **Adenosquamous carcinoma**, which is characterized by both adenocarcinoma and squamous carcinoma components; it's quite rare and generally more aggressive.
4. **Spindle cell carcinoma**, containing elongated and spindle-shaped tumor cells, a rare variant associated to aggressiveness and poor prognosis.
5. **Undifferentiated carcinoma**, poorly differentiated tumor lacking features of glandular or squamous differentiation. It is highly aggressive and associated to poor prognosis.

1.3 Colorectal Cancer pathogenesis and staging

CRC pathogenesis is usually initiated by carcinogenic factors, responsible for the DNA structural changes, leading to the transformation of the epithelial cells of colorectal mucosa. These cells can undergo a range of proliferative changes, including hyperplasia, atypical hyperplasia (mild, moderate, severe) and adenomas, that can eventually develop into carcinoma. In 1990, Fearon and Volegestein identified the molecular events underlying the initiation and progression of CRC and proposed a genetic model for CRC tumorigenesis. According to this model, the inactivation of both alleles of the adenomatous polyposis coli (APC) gene was identified as the very first event in CRC tumorigenesis, leading to the development of polyps, benign neoplastic lesions. Subsequently, the activation of K-ras protooncogene mutation leads to the development from early adenoma to intermediate adenoma. Next in the progression from adenoma to carcinoma is the mutation of DCC correlated to the development of late adenoma. Mutation of the tumor suppressor gene p53 (TP53) is related to late-stage CRC development, allowing tumor growth by altering the regulation of cell cycle and apoptosis. These mutations together with mutations on MMR-related genes (hMLH1, hMLH3, hMSH2, hMSH3, hMSH6, hPMS1, and hPMS2) are responsible for the development of metastases [11].

Four stages are recognized in CRC pathogenesis and are based on the progressive continuum above described. The earliest stage of CRC is called stage 0 (a very early cancer), followed by a range from stages I to IV. The higher the number, the more the cancer has spread. The most used staging system for CRC is the American Joint Committee on Cancer (AJCC) TNM

system, which is based on the extent of tumor growth into the wall of colon or rectum (T), lymph nodes involvement (N), and metastases establishment (M), as described in *Table 2*.

Table 2 - AJCC Stage Grouping Summary. Tabled adapted from American Cancer Society (https://www.cancer.org/cancer/types/colon-rectal-cancer/detection-diagnosis-staging/staged.html)

Stage	T	N	M	Description
0	Tis	N0	M0	Cancer in situ; has not grown beyond inner mucosa.
I	T1–T2	N0	M0	Grown into submucosa (T1) or muscularis propria (T2); no lymph node or distant spread.
IIA	T3	N0	M0	Grown into outermost layers; no lymph node or distant spread.
IIB	T4a	N0	M0	Grown through wall (not into other organs); no node/distant spread.
IIC	T4b	N0	M0	Grown into nearby tissues/organs; no node/distant spread.
IIIA	T1–T2 or T1	N1/N1c or N2a	M0	Early tumor with 1–6 lymph nodes involved or tumor deposits in fat.
IIIB	T2–T4a or T1–T2	N1–N2b	M0	More extensive local growth with 1–7+ lymph nodes involved.
IIIC	T3–T4b	N2a–N2b or N1	M0	Extensive tumor and/or lymph node involvement (≥4 nodes or nearby tissues/organs).
IVA	Any T	Any N	M1a	Spread to 1 distant organ/set of nodes (e.g., liver or lung).
IVB	Any T	Any N	M1b	Spread to >1 distant organ/set of nodes.
IVC	Any T	Any N	M1c	Spread to peritoneum (± other distant sites).

1.4 Metastatic colorectal cancer

Despite during the last year metastatic CRC survival rates have been increasing, it still represents a lethal disease with a 5-year survival rate of approximately 14% [12]. Recently novel technologies such as whole genome and single cell sequencing, CRISPR/Cas9 system, and advanced transgenic animal models have increased the understanding of the complex mechanism underlying CRC metastasis development. Several factors have been identified as crucial for the regulation of metastasis, including tumor cell-intrinsic factors as well as the

surrounding tumor microenvironment [13].

For what concernes tumor cells intrinsic factors, **genetic abnormalities** play a crucial role. In contrast to primary CRC, the genomic landscape of metastatic CRC has not been fully elucidated. It's aknowledged that 60% of CRC patients with metastases show TP53 mutations [14], which together with APC, KRAS and PIK3CA, have been identified as the top mutateed gened in metastatic CRC [15].

Another key event in the initiation of metastasis is the **epithelial mesenchymal transition** (**EMT**), a process consisting of the loss of epithelial characteristics and the acquisition of mesenchymal properties, which allow cell motility and the development of an invasive phenotype [16]. More than 90% of CRC cell lines exhibit EMT, which prompts the formation of cell clusters during CRC dissemination [17].

Another important event in metastatic CRC is the **tumor microenvironment** (**TME**), a complex assemblage of heterogenous populations actively shaping and regulating cancer progression. As shown in Figure 2, these populations include:

1. **Cancer-associated fibroblasts** (**CAFs**), involved in extracellular matrix (ECM) deposition and remodeling, signaling interaction with cancer cells and infiltrating immune cells [18]. CAFs favor tumor progression by sustaining cell proliferation, cell death evasion, and immune cells recruitment [19].
2. **Tumor-associeated macrophages** (**TAMs**), which maintain an immunosuppressive environment by expressing checkpoint inhibitor proteins, such as protein death-ligand (PD-L1 and PD-L2), and by releasing IL-10 and TGF-β to activate regulatory T cells [20].
3. **Myeloid-derived suppressor cells** (**MDSCs**), immature myeloid cells, able to suppress immune responses and induce EMT.
4. **Regulatory T-cells** (**T-regs**), which can initiate tumor metastasis by prompting tumor dissemination and immune celle evasion [21].

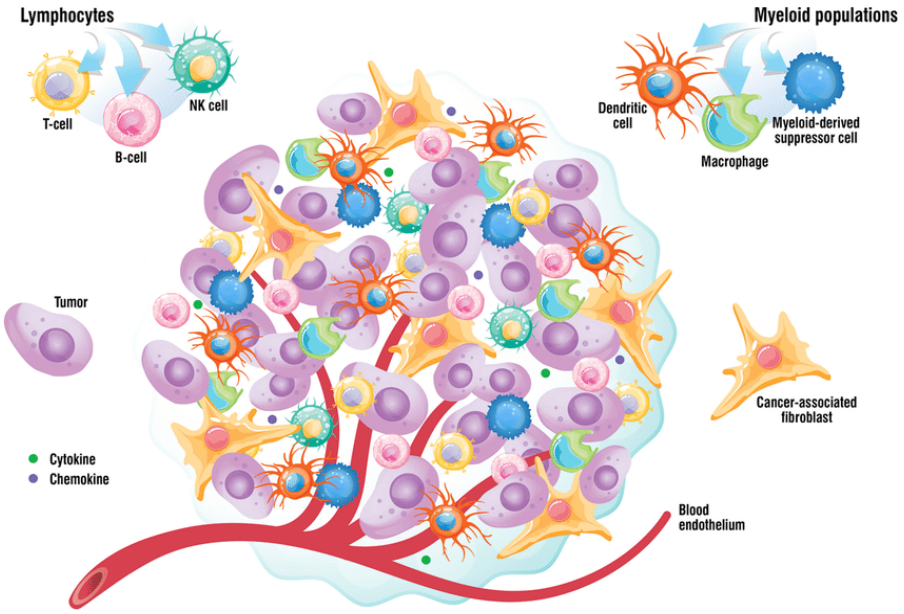

Figure 2 – Representative image of the tumor microenvironment and its cellular components. Source: Allemailem KS et al. 2023 [22].

1.5 Colorectal cancer-derived liver metastases

The liver is the most common site of CRC metastasis, largely due to the anatomical organization of the venous drainage system, in which the mesenteric veins converge into the hepatic portal vein (*Figure 3*), directing tumor cells from the colon and rectum to the liver, and due to the liver diverse cellular composition and architecture, which make the liver hospitable to tumor cells [23].

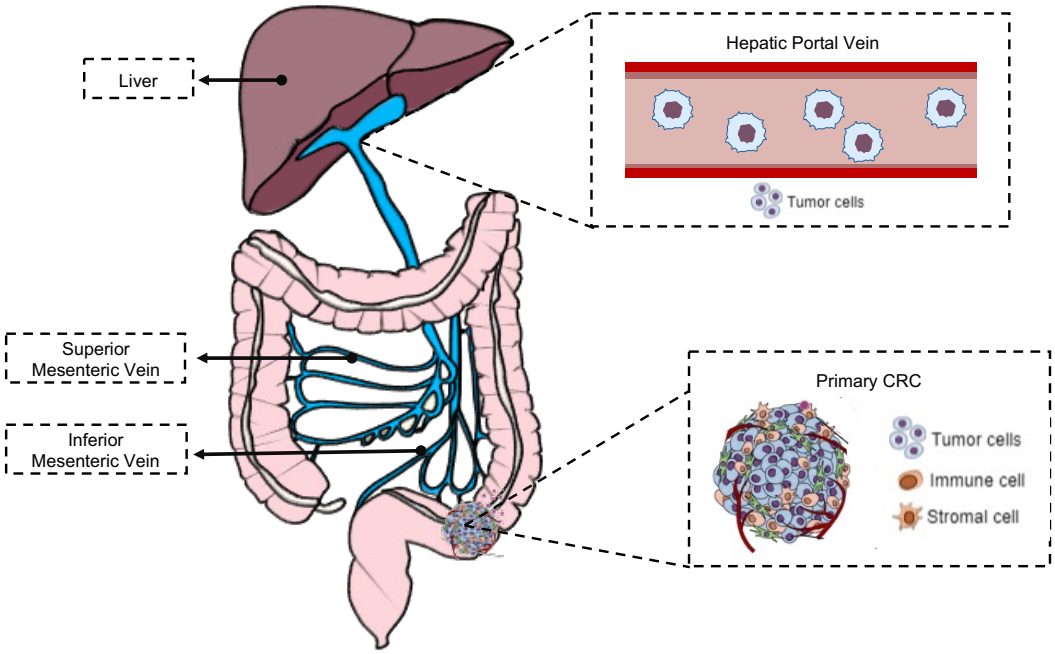

Figure 3 - Representative image illustrating the route taken by circulating tumor cells originating from primary CRC, traveling through the mesenteric veins into the portal vein, ultimately reaching the liver.

It is estimated that approximately 50% of CRC patients will develop liver metastases during their disease, and around 15% present liver metastases at the time of initial diagnosis [24]. Importantly, liver metastases represent the leading cause of CRC-related mortality [25]. Therefore, it is fundamental to identify and characterize the mechanisms driving metastasis initiation, with the ultimate goal of allowing targeted strategies, able to block this fatal evolution of tumor progression.

The hepatic metastatic cascade of CRC is a complex, multifactorial, and multistep biological process, which involves several resident hepatic cells populations:

- **Hepatic stellate cells (HSCs):** these are pericytes located in the space of Disse, capable of differentiating into myofibroblasts. HSCs are highly proliferative and mobile, and can deposit ECM in response to liver damage and inflammation. In the tumor context, excessive activation of HSCs facilitates metastatic colonization of the liver [26], promoting the secretion of matrix metalloproteinases (MMPs) to remodel existing ECM, and the production of collagen and other ECM proteins [27][28]. HSCs are also involved in angiogenesis, the recruitment of inflammatory cells, and immunosuppression within the tumor microenvironment, attenuating the function of anti-tumor T cells [29][30][31]
- **Kupffer cells:** these are liver-resident macrophages located in the lumen of liver sinusoids, and represent a key component of the first immune defense line against pathogens, toxins,

and abnormal cells. During the formation of liver metastases, particularly those from colorectal or breast origin, Kupffer cells exhibit biphasic and context-dependent functions that can either limit or promote tumor colonization [32]. In the early phase, Kupffer cells can phagocytose circulating tumor cells (CTCs), releasing pro-inflammatory cytokines (e.g., IL-1β, TNF-α) and reactive oxygen species (ROS), aiding in tumor cell clearance. However, over time, tumor cells can reprogram the immune environment, turning Kupffer cells into a pro-tumoral phenotype, similar to TAMs. In this altered context, Kupffer cells promote tumor cell adhesion and extravasation into hepatic tissue, secrete pro-angiogenic factors such as VEGF and MMP-9, and release immunosuppressive cytokines like IL-10 and TGF-β, which inhibit cytotoxic T lymphocytes and NK cells activity, thus contributing to an immunosuppressive microenvironment that supports metastatic growth.

- **Liver sinusoidal endothelial cells (LSECs):** these are specialized, fenestrated and discontinuous endothelial cells forming a barrier between hepatic circulation, the underlying space of Disse, and the liver parenchyma. LSECs are particularly permeable, support low-resistance blood flow (low shear stress), and have a thin or discontinuous basal membrane, facilitating exchange between blood and hepatic parenchyma. Due to their unique nature, LSECs play important roles in liver physiology, immunity, and pathology. During metastasis, circulating tumor cells often become trapped within the narrow hepatic vasculature, where Kupffer cells and NK cells may aid in their clearance [33]. However, LSECs can express surface proteins such as ICAM-1, E-selectin, and lectins, which increase tumor cell adhesion, extravasation, and invasion into the liver parenchyma, thus mediating progression along the metastatic cascade [34][35][36].
- **Hepatocytes (Heps):** these cells represent the main parenchymal component of the liver, responsible for the majority of hepatic metabolic functions, and account for approximately 80% of liver mass. During the actual metastatic phase, after tumor cells have arrived and adhered to hepatic tissue, the direct interaction between Heps and metastatic tumor cells becomes a crucial step in either supporting or limiting secondary growth [37][38]. It has been shown that tumor cells form dynamic protrusions (pseudopodia) to adhere to Heps' surfaces. This process is mediated by adhesion molecules such as integrins (e.g., α2β1) and claudin-2, promoting heterotypic interaction between tumor epithelial cells and Heps [37].

1.6 Hepatic pre-metastatic niche

For the circulating tumor cells (CTCs) to attach and colonize the liver, it's fundamental the presence of a receptive and supportive microenvironment, favoring their survival and proliferation. The importance of this environment has been already recognized in 1889 when Stephen Paget described for the first time the "seed and soil" theory, revealing the strict relationship between circulating tumor cells (seed) released from the primary tumor, and the microenvironment favoring their attachment in the target organs (seed) [39]. Kaplan *et al.* defined for the first time this microenvironment as Pre-Metastatic Niche (PMN), describing it as a receptive and supportive microenviroment for the colonization of CTCs and the formation of novel metastatic sites [40]. This environment, illustrated in *Figure 4*, is characterized by several key features:

- **Angiogenesis**, the formation of new blood vessels, aimed at ensuring proper oxigen and nutrients intake, thus favoring the arrival and survival of metastatic cells [41].
- **Fibrosis**, caused by the reorganization and excessive deposition of ECM, thus modifiyng the tissutal architecture and creating a favorable microenvironment for CTCs adhesion and invasion [42].
- **Inflammation**, mediated by immune cells recruitment and pro-inflammatory cytokines release [43].
- **Immune suppression**, caused by the acrivation of immunesuppressive cells, such as mieloyd suppressor cells or lymphocytes Treg, which inhibit the antitumoral immune response, allowing CTCs to evade from the immune system (*tumor immunoescape*) [44].

PMN formation is strongly influenced by the release from tumoral cells of secreted factors known as **Tumor-Derived Secreted Factors** (**TDSFs**). These molecular elements are able to impact the behavior of target cells, promoting the creation of a favorable microenvironement for CTCs colonization. Among the TDSFs we can mention:

- **Cytokines and Chemokines** such as VEGF-A, released from primary tumors to increase vascilar permeability, by disrupting endothelial tight junction, thereby facilitating later tumor cells infiltration [45], IL-6, key mediator of inflammation [46], and TGF-β, master regulator of EMT [47][48].
- **Growth factors,** such as Platelet-Derived Growth Factor (PDGF) and Fibroblast Growth factor (FGF), which support vascular remodellin and angiogenesis [49][50].

- **Matrix Remodeling Enzymes**, such as metalloproteases, which degrade and remodel ECM making the microenvironment more accessible to CTCs [51].
- **Metabolites and Reactive Molecules**, such as lactate and ROS, which can modulate immune suppression and angiogenesis [52].

In addition to TDSFs, primary tumors employ the release of **extracellular vesicles** (EVs) as a critical strategy to influence and communicate with surrounding and distant cells. **EVs** are particles enclosed by a lipid bilayer, which physically protects their internal content, including proteins, lipids, nucleic acids and metabolites. Differenly from soluble factors, which often have short half-lives due to rapid enzymatic degradation and clearance, EVs exhibit greater stability in blood and body fluids, allowing them to circulate for longer periods and reach distant sites intact, thereby efficienlty delivering their cargos in the target cells. For these reasons the tumor-derived EVs have emerged as key mediators in PMN formation and will be the focus of Chapter 2.

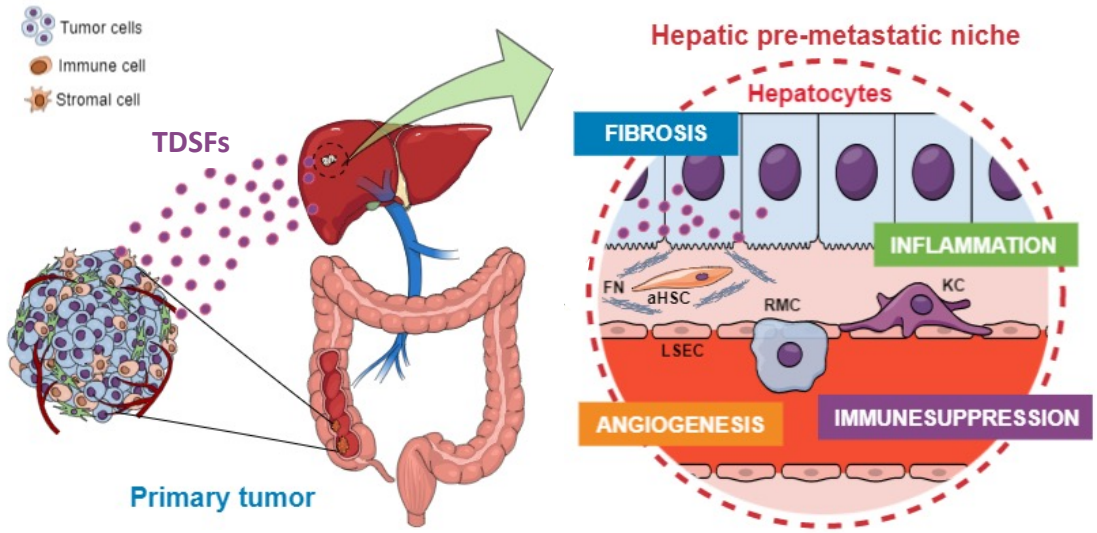

Figure 4 – Representative image depicting the release of TDSFs from primary CRC, their transport to the liver, and their impact on the hepatic microenvironment, contributing to the formation of the hepatic PMN.

1.7 Treatment of colorectal cancer

For **non-metastatic CRC** the most common treatments are:

- **Surgical resection**, followed by **adjuvant chemotherapies**, such as 5-fluorouracil (5-FU), capecitabine, or oxaliplatin.
- **Chemoradiotherapy**, applicable only for rectal cancer, which consists in a combination of chemotherapy (usually 5-FU or capecitabine) and radiation. This treatment is followed by

surgical resection and may be followed by **adjuvant chemotherapy**.

Although these treatments are well known to reduce recurrence rates and improve both survival and long-term outcomes, their toxicity to healthy cells and the resulting impact on patients' quality of life cannot be overlooked. In fact, these traditional drugs work by damaging DNA, thereby rapidly affecting dividing cells but at the same time leading to significant toxicity thus limiting a prolonged use. Additionally, CRC cells often develop resistance to chemotherapeutic agents, underscoring the urgent need for more effective and less toxic therapeutic strategies.

For the treatment of **metastatic CRC**, beyond the application of traditional chemotherapies, such as are 5-FU, capecitabine, irinotecan, and oxaliplatin, **targeted therapies** have been arising. Targeted therapies are based on the application of agents able to recognize and target tumor cells, by interacting with cancer-specific receptors or signaling pathways highly active in tumor cells. This mechanism of action minimizes the side effects on healthy cells. Among the most prominently activated pathways at metastatic sites, angiogenesis and immunosuppression remain the primary therapeutic targets.

Key targets involved in **angiogenesis** include VEGF, which is markedly upregulated in tumor cells [53], and epidermal growth factor receptor (EGFR), overexpressed in 60–80% of colorectal cancers [54].

In the context of **immunesuppression**, it's well established that several inhibitory molecules can be expressed by tumor cells to suppress immune cell activation, thereby favoring the establishment of an immunosuppressive microenvironment. Among these molecules we can mention **Programmed Death Ligand 1** (**PD-L1**), a checkpoint inhibitor protein which binds to the Programmed Death 1 (PD-1) receptor on T-cells and **Cytotoxic T-Lymphocyte Associated protein 4** (**CTLA4**) which binds the surface proteins CD80 and CD86. Activation of the PD-L1 and CTLA-4 pathways, triggered by their binding to the respective receptors, leads to T lymphocyte clonal anergy and results in suppression of the immune response. In the light of the key role of these factors in favoring tumor immune escaping, immunotherapies targeting these common immune checkpoint proteins have emerged as valuable strategy to fight cancer. Although remarkable progresses have been achieved in finding novel ways to target cancer cells, as revealed by the growing number of FDA-approved immunotherapies, however there is still the need to further unravel the mechanisms underlying metastasis development to discover new and more effective targets for tumors that are resistant to current targeted therapies

CHAPTER 2 – Extracellular vesicles

Extracellular vesicles (EVs) are nanosized particles characterized by a lipid membrane bilayer, deriving from either the plasma membrane (blebbing) or from the endo-lysosomal system. These structures are released by almost all living cells [55], including tumor cells. Despite initially considered part of a clearance mechanism for cells, these particles play a key role in intercellular communication in both physiological and pathological contexts [56]. EVs are highly abundant in body fluids (blood, urine, saliva, breast milk etc.) and mediate the transfer of several molecules including proteins, lipids, nucleic acid, metabolites, which impact the behavior and the phenotype of the recipient cells [57].

2.1 Classification and Biogenesis

Based on size, biogenetic origin, and release mechanism, EVs are classified into different subpopulations, as illustrated in *Figure 5*:

- **Small Extracellular Vesicles (sEVs):** these are particles ranging in size from 30 to 150 nm, primarily including **exosomes**. Exosomes have an **endocytic origin** and are formed within specialized endosomal organelles called **multivesicular bodies (MVBs)**. During the maturation process, small intraluminal vesicles (ILVs) form inside MVBs. Once the MVBs fuse with the plasma membrane, these ILVs are released into the extracellular space as exosomes. These vesicles play a key role in intercellular communication, transporting molecules such as proteins, lipids, RNA, and other biochemical signals. In addition to exosomes, other small vesicles may be included within the sEV category, though their origin and biogenetic mechanisms can vary and are not always fully defined. Some of these subtypes may be formed through ESCRT-independent pathways or influenced by specific cellular conditions.
- **Microvesicles:** these represent a population of larger vesicles, generally ranging from 100 to 1000 nm in size. Microvesicles originate directly from the plasma membrane through an outward budding process, in which the membrane protrudes and pinches off, releasing a vesicle into the extracellular space. The release of microvesicles is regulated by changes in the cytoskeleton and intracellular signals such as elevated calcium levels. These vesicles can carry membrane proteins, lipids, and functional molecules involved in cell signaling.
- **Apoptotic bodies:** these are much larger vesicles, with sizes ranging from 1 to 5 μm, released by cells undergoing programmed cell death (apoptosis). During this process, the

cell fragments into multiple parts through a mechanism known as blebbing, which involves the formation of bulges (blebs) on the plasma membrane that detach to form apoptotic bodies. These bodies contain cellular fragments and can be phagocytosed by surrounding cells or macrophages, contributing to the orderly removal of dead cells and the maintenance of tissue homeostasis [58].

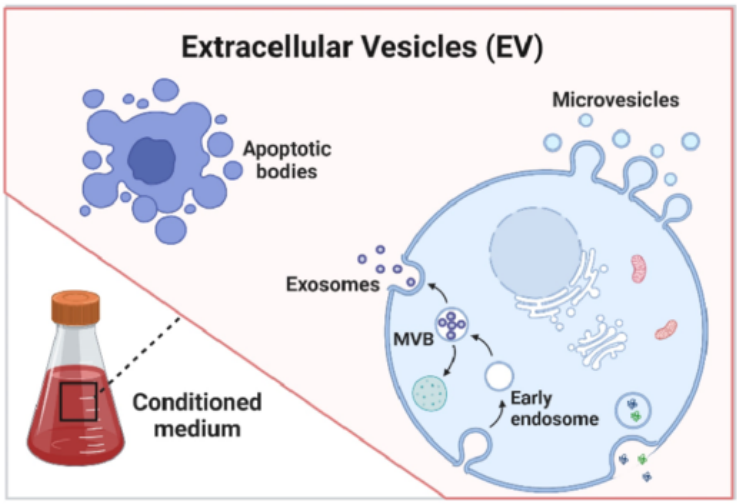

Figure 5 – Representative image of the different extracellular vesicles subpopulations, including sEVs (exosomes), microvesicles, and apoptotic bodies. Adapted from Yang G et al, 2023 [59].

2.3 Small Extracellular Vesicles Cargo

SEVs are characterized by a heterogeneous composition of numerous biomolecules, as shown in *Figure 6*. Specifically, sEVs are characterized by the presence of:

- **Nucleic acids**, such as DNA, mRNA, and various types of non-coding RNAs (microRNAs, long non-coding RNAs, circular RNAs, small nucleolar RNAs, small nuclear RNAs, transfer RNAs, and ribosomal RNAs) [60], which are transported intact by sEVs to target cells, protected from degradation in the extracellular environment [61][62].
- **Proteins**, including membrane proteins such as tetraspanins (e.g., CD9, CD63, CD81), essential for vesicle assembly, stability, and recognition by target cells and often used as specific sEVs markers. SEVs also contain proteins involved in trafficking and transport, crucial for vesicle biogenesis and cargo selection, such as ESCRT (Endosomal Sorting Complex Required for Transport) proteins, Alix, and TSG101. Similarly to tetraspanins these proteins are often used as specific sEV markers.

Additionally, sEVs contain cytoskeletal proteins (e.g., actin, tubulin) and signaling proteins (e.g., enzymes, growth factors, receptors).

- **Lipids**, including cholesterol, sphingomyelin, glycolipids, and phospholipids (e.g., phosphatidylserine, phosphatidylcholine), which are present on the sEV membrane. These lipids are involved in target cell recognition and internalization, and in the modulation of cellular responses such as inflammation, cell migration, and proliferation.

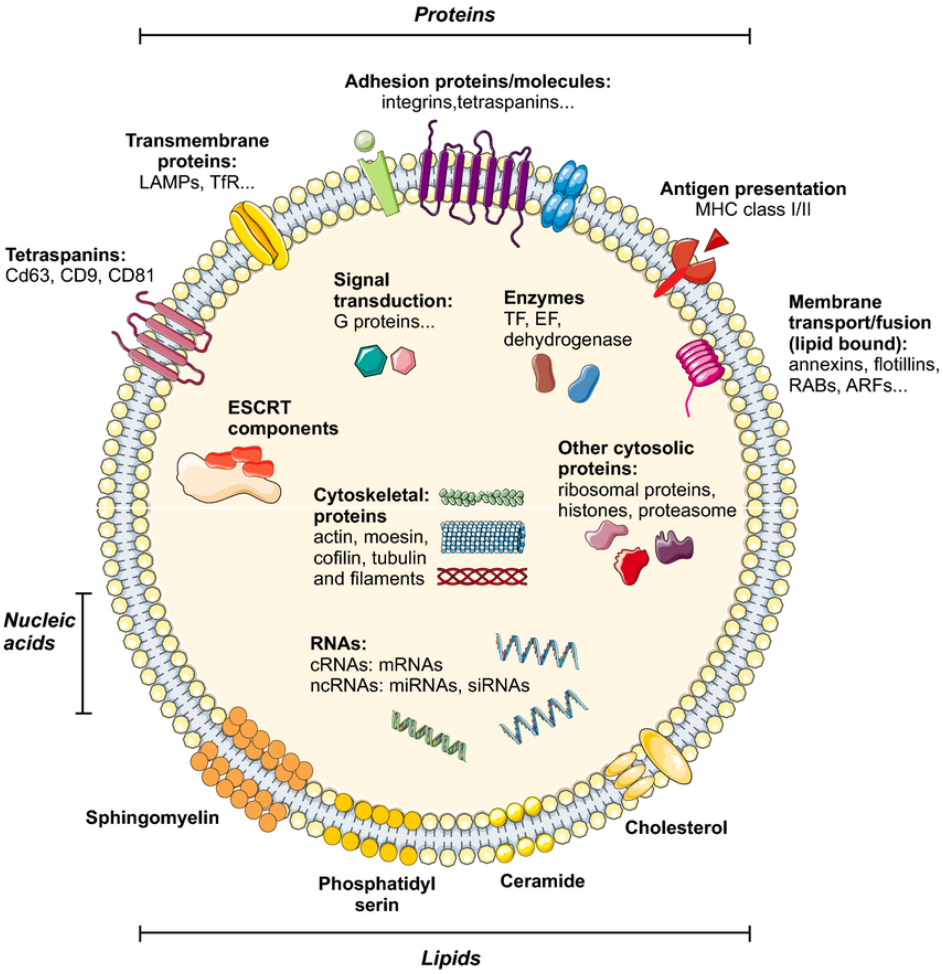

Figure 6 – Representative image of the composition of sEVs in terms of proteins, nucleic acids, and lipids. Adapted from Shahraki et al. 2023 [63].

2.4 Internalization of Small Extracellular Vesicles

Once released in the extracellular space, sEVs can be internalized in target cells through several mechanisms, allowing the transfer of their cargo inside the recipient cells. The most common mechanisms underlying the sEVs internalization process, shown in *Figure 7*, are:

- **Clathrin-mediated endocytosis**, in which sEVs are internalized through the formation of clathrin-coated vesicles that invaginate and subsequently form early endosomes [64].
- **Caveolin-mediated endocytosis**, in which vesicles are internalized through membrane invaginations called *caveolae*, which are rich in caveolin and cholesterol [65].
- **Clathrin- and caveolin-independent endocytosis**, which includes mechanisms such as phagocytosis and micropinocytosis [66], where the target cell internalizes portions of extracellular fluid, thereby engulfing sEVs as well [67].
- **Direct fusion** with the plasma membrane, in which sEVs release their content directly into the cytoplasm by fusing their membrane with the recipient cell's plasma membrane [67].
- **Internalization via surface proteoglycans**, in which sEVs can bind to proteoglycans (e.g., heparan sulfate) on the cell surface, facilitating their anchoring and subsequent internalization [68].
- **Receptor-mediated endocytosis**, in which specific receptors recognize ligands expressed on sEVs, enabling their recognition and internalization through receptor-specific pathways [69].

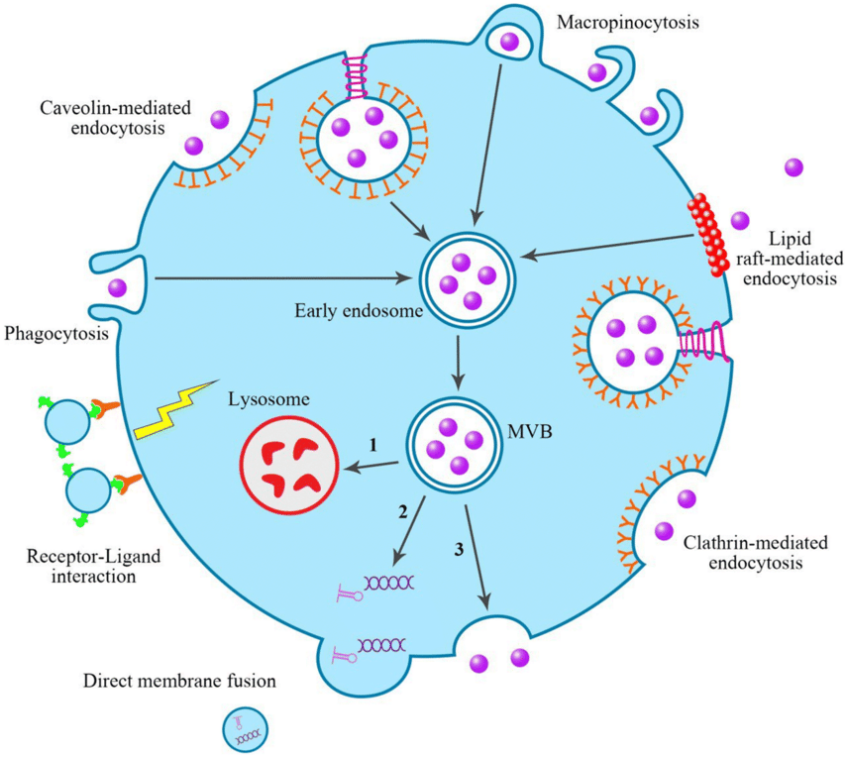

Figure 7 – Representative image of the different sEVs internalization mechanisms. Source: Samii A, et al. 2020 [70].

Recent studies have highlighted an unexpected role of sEVs in intracellular trafficking, revealing their ability to deliver their cargo into the nucleoplasm, suggesting a direct integration between the endosomal pathway and nuclear regulation. Specifically, Rappa et al. described that sEVs, once internalized through endocytosis, are transported to late endosomes (LEs), which are positioned near the nucleus within nuclear envelope invaginations (NEIs) [71]. Santos et al. revealed that this specific event is regulated by the VOR protein complex, consisting of **VAP-A** (Vesicle-associated membrane protein-associated protein A), an endoplasmic reticulum protein, which interacts through the FFAT (two phenylalanines in an acidic tract) domain with **ORP3** (Oxysterol-binding protein-related protein 3), which in turns binds the GTPase **Rab7** (Ras-related protein Rab-7) via its N-terminal region [72].

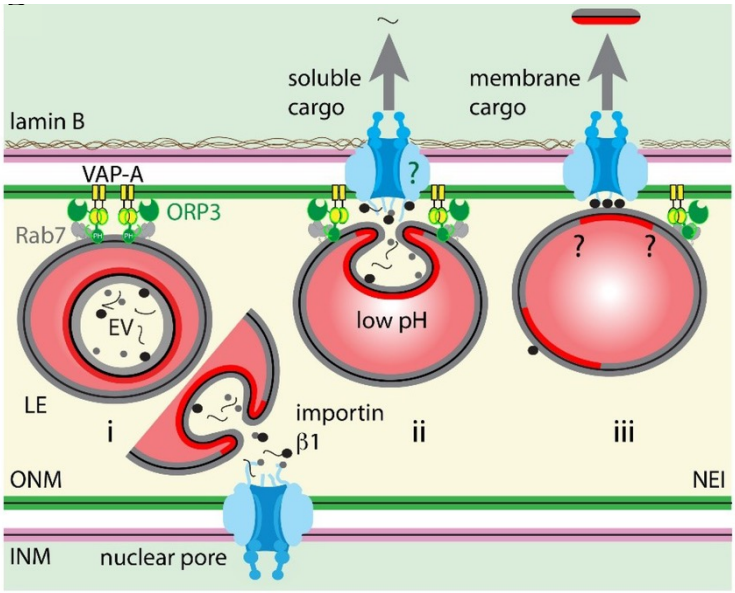

Figure 8 – Representative image of VOR complex involvement in the translocation of late endosomes into the nucleoplasmic reticulum and nuclear transfer of EV-derived components. Adapted from Corbeil D et al. 2020 [73].

2.5 Methods for Small Extracellular Vesicles Isolation

The isolation of sEVs from biological fluids has long represented a significant challenge for the scientific community. During the isolation process, it is essential to efficiently eliminate unwanted contaminants such as protein aggregates or lipoprotein particles, which can compromise the accuracy and purity of the isolated sample [74].

To address this issue, numerous approaches have been developed over the years, aimed at exploiting sEVs' morphological properties, such as size and density, or their biochemical

characteristics, such as solubility or affinity for specific protein markers. The preferred strategy is chosen based on the starting sample (e.g., cell culture, blood, urine) and the purpose of the analysis (e.g., quantification or diagnosis of specific diseases) [75].

Traditional techniques, such as differential **ultracentrifugation (UC)**, have long been considered the gold standard. These methods allow the processing of large volumes and the separation of different populations based on density, by exploiting the differential sedimentation of particles at increasing centrifugation speeds and durations. However, they require expensive equipment, may lead to co-precipitation of unwanted proteins, and can promote vesicle aggregation [76].

In addition to this traditional method, several companies have developed rapid and user-friendly **sEV isolation kits** aimed at minimizing the processing time and the required sample volume compared to conventional methods. These kits often exploit the lipophilic nature of sEVs, allowing them to be selectively captured or precipitated through interaction with specific substances or materials included in the kit, thereby facilitating their isolation. However, the reliability and specificity of these kits vary and they do not always represent the most effective solution. Moreover, commercial kits for sEV isolation/analysis tend to be relatively expensive and are often limited to processing only a small number of samples [77].

Recently, **Size-Exclusion Chromatography** (**SEC**) has emerged as a promising technique for sEVs isolation. SEC is a filtration-based method that enables the elution of sEVs through a column packed with polymer beads of varying pore sizes [78][79]. Unlike smaller proteins, sEVs do not penetrate the resin's pores but are retained on the surface, which slows their elution time compared to larger particles that are eluted first. This strategy enables the isolation of sEVs based on size, while preserving their integrity and biophysical properties [80].

The sEV isolation techniques described above are illustrated in *Figure 9*.

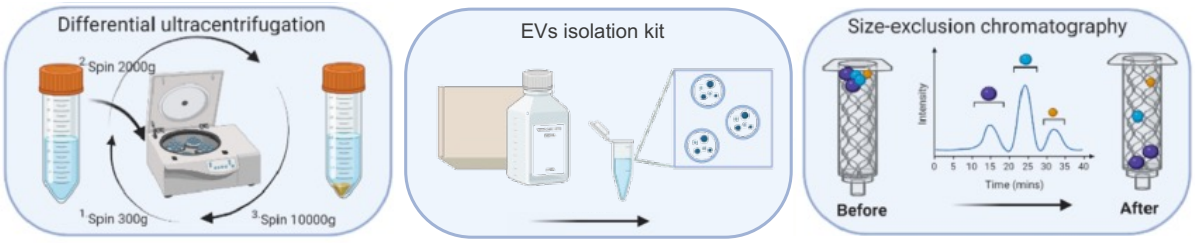

Figure 9 – Representative image of different sEVs isolation tecniques, including differential ultracentrifugation, sEVs isolation kit, and SEC. Adapted from Yang G et al, 2023 [59].

2.6 Characterization of Small Extracellula Vesicles

According to **MISEV 2023** (*Minimal Information for Studies of Extracellular Vesicles 2023*), a guideline document aimed at standardizing the study and application of sEVs, it is essential that sEVs are characterized using a multiparametric approach to confirm their identity, purity, and origin. This includes analysis of size, concentration, morphology, and molecular content.

For **size analysis**, the method of choice is **Dynamic Light Scattering (DLS)**. This technique measures the scattering of light by particles undergoing Brownian motion in suspension. By analyzing fluctuations in the intensity of light scattered by the particles, the velocity of their Brownian motion is calculated, allowing for the determination of the particles' average hydrodynamic diameter [81].

For **concentration analysis**, the most widely used technique is **Nanoparticle Tracking Analysis (NTA)**. This method combines laser light scattering microscopy with a camera that allows visualization and recording of nanoparticles in solution. In this system, the vesicles are carried by a flow, and the NTA software tracks the Brownian motion of individual particles, calculating their size and total concentration [82].

For **morphological analysis**, the most common characterization methods involve **electron microscopy**, particularly **TEM** (Transmission Electron Microscopy), **Cryo-TEM** (Cryo-Transmission Electron Microscopy), and **SEM** (Scanning Electron Microscopy), high-resolution imaging techniques that allow observation of sEVs shape and structure, confirming their vesicular nature [83].

For **molecular analysis**, the preferred technique is **Western blot**, used to detect specific sEVs markers, including membrane tetraspanins (**CD9**, **CD63**, **CD81**), as well as biogenesis-associated proteins such as **Alix** and **TSG101**. Equally important for verifying the purity of the preparations is the evaluation of **negative markers**, cellular or subcellular contaminants such as **Calnexin**, a specific protein of the endoplasmic reticulum, and **GM130**, a Golgi-specific protein [84].

2.7 State of the art in the involvement of CRC-sEVs in hepatic pre-metastatic niche

The involvement of tumor-derived sEVs in the hepatic PMN formation has been already described in literature with regards to their effect on non parenchymal liver cells:

- **Kupffer cells**: Y. Shao et al. report that CRC-sEVs can regulate Kupffer cells immunodulatory properties, thus favoring in the liver local inflammation via the NF-κB

signaling pathway and promoting the subsequent release of the pro-inflammatory cytokine IL-6, increased ECM deposition, and vascular remodeling [85], thus contributing to hPMN formation.

- **Liver sinusoidal endothelial cells (LSECs)**: it has been reporteted that LSECs exposure to CRC-sEVs determine increased vascular permeability, facilitating angiogenesis and the passage of tumor cells through the endothelium [86].
- **Hepatic stellate cells (HSCs)**: Costa-Silva et al. demonstrated that pancreatic tumor derived-sEVs induce in HSCs an increased expression of Apha-Smooth Muscle Actin (α-SMA), a typical marker of the myofibroblastic phenotype. Once activated, these HSCs secrete fibronectin, a fundamental ECM glycoprotein aknwoledged as a structural component of the fibrotic liver and involved in the recruitment of pro-tumor myeloid cells [87].

Beyond influencing the behavior of resident liver cells, sEVs can also impact recruited cells within the hepatic PMN, such as **macrophages**. Pucci et al. showed that CRC- and myeloma-derived sEVs can impact macrophages M0 behavior by increasing the expression of proinflammatory cytokines like IL-6 and the immune checkpoint inhibitor PD-L1, thereby favoring the creation of an inflammatory and immunesuppressive microenvironment [88].

Regarding **Heps**, the most conspicuous and functional cell component in the liver, their role in liver metastasis is partly described and related to the pro-metastatic process [89]. Nevertheless, our research group provided the first evidence on Heps' involvement in the early stages of tumor progression in a recently published paper by Pucci et al. [90]. This study revealed the ability of CRC-sEVs to induce Heps to undergo EMT, early event leading to liver fibrosis, depicting for the first time an overlooked, yet critical, role of Heps, educated by CRC-sEVs in shaping in liver a favorable microenvironment for metastatic colonization. Despite this novel insight, a more comprehensive understanding of the mechanisms underlying Heps involvement in fibrosis, as well as their potential role in other key processes contributing to PMN formation, is still required to fully elucidate how the liver prepares to support and promote metastatic growth.

CHAPTER 3 - Models to study EVs' involvement in cancer progression

Given the key roles that sEVs play in intercellular communication and in pathological processes such as cancer, recent years have seen an increased interest in understanding their various implications in human health. In just the last two years, over 10.000 papers regarding sEVs have been released, the most of them relying on traditional bidimensional (2D) *in vitro* models. While these models are valuable for obtaining fundamental insights, they are not well suited to describe all the complex events underlying hepatic PMN formation. From this arises the need for *in vivo* experimentation, representing an omnicomprehensive approach, where cells are not isolated but rather interact with each other in physicologically revelant ways. Among all the animals employed for *in vivo* experimentation, rodents models, particularly mice and rats, play a fundamental role, due to their genetic, physiological, and anatomical similarities to human.

However, animal testing has many practical and logistical drawbacks, such as high cost, time, and strict regulations, which, together with the ethical implications, can act as a major barrier to cancer research relying on animal testing. This highlights the need for models able to overcome the limitations of traditional 2D cell cultures while limiting the use of animal experimentation. Considering this, Russel and Buch formualted in the 1959 "The Principles of the 3R" (Replacement, Reduction, and Refinement), advocating for a new applied science to improve the treatment of laboratory animals by reducing their application, refining the experimental designs, and replacing their use, when possible, with alternative models [91]. Since then, significant effort has been put on creating alternative approaches that serve as a more accessible and yet physiologically relevant systems, to the point that alternative models are now recognized within the scientific community as a conjunction ring between *in vitro* and *in vivo* models, overcoming *in vitro* traditional models' limitations, whilst limiting animal experimentation.

3.1 Alternative three-dimensional *in vitro* models: spheroids

Three-dimensional (3D) cell culture models have been developed as effective alternatives to animal experimentation. The advent of 3D colture system relies on the numerous advantages that this system have in comparison to canonical 2D colture system. Notably, 3D systems allow cells to interact to each other and to the sourrounding microenvironment in three dimensions, thereby promoting cell-cell and cell-ECM interactions. Moreover, cellular morphology,

behavior, and organization more closely replicate the native tissue. In addition, thanks to their tridimensional structure, 3D cultures exhibit layered cellular arrangements, differently exposed to the external environment, thus allowing the formation of a gradient of nutrient and oxygen. Despite all these advantages, 3D cell cultures have some drawbacks, such as cost, lack of reproducibility, and challenges in identifying the most suitable assay for downstream analyses. The advantages and disadvantages of 3D cell culture are summarized in *Table 3*.

2D Cell Cultures		3D Cell Cultures	
Advantages	**Disadvantages**	**Advantages**	**Disadvantages**
Inexpensive	Not representative of real cell environment	Better mimic tissue-like structures	Expensive
Well-established	Lack of predictivity	Exhibit differentiated cellular function	Reproducibility could be unsatisfactory
Large amount of comparative literature	Lack of cell–cell interactions	Simulate microenvironment conditions	Some systems are limited due to the static conditions
Easier cell observation and measurement	Lack of cell–ECM interactions	Better predict in vivo responses to drug treatment	Difficulties in finding the right assay for analysis

Table 3 – Advantages and disadvantages od 2D and 3D cultures. Source: Urzì O, et al. 2023 [92].

Spheroids development and applications - One of the earliest 3D culture models developed was the spheroid. Introduced for the first time in 1970 by Sutherland et al. to study cancer cell response so radiotherapy [93], spheroids are spherical, self-assembling cellular aggregates, generated by either single cell type (homotypic spheroid) or from multiple types (heterotypic spheroids) [94].

Various techniques have been developed to generate spheroids, mainly relying on the self-assembly properties of cells. These methods, summarized in *Figure 10*, include:

- *Pellet culture*, where cells are cultured on non-adherent surfaces.
- *Liquid Overlay*, in which cells are seeded in non-adhesive surfaces such agarose.
- *Hanging drop*, in which cells aggregate within suspended droplets.
- *Magnetic levitation*, in which cells internalizing magnetic nanoparticles can levitate due to a magnetic field which enhance their aggregation.

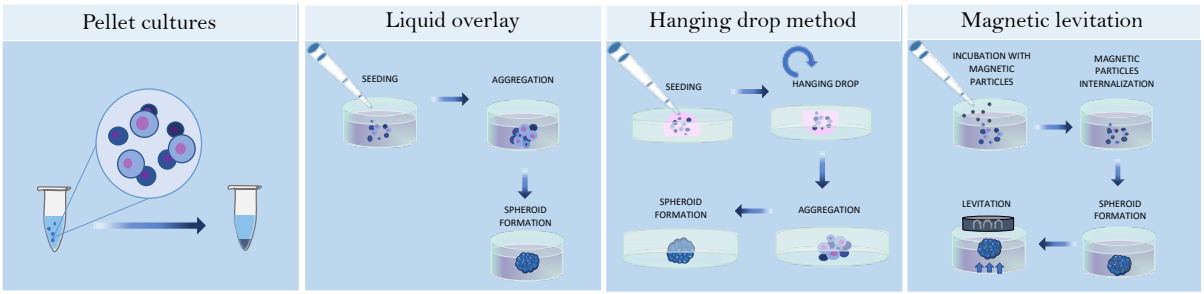

Figure 10 – Schematic representation of the different methods to generate spheroids. Adapted from Urzì O, et al. 2023 [92].

The applications of 3D spheroids offer several advantages in comparison to canonical 2D culture systems, including:

- *Enhanced physiological relevance*: spheroids recapitulate the native tissue microenvironment by establishing cell-cell and cell-ECM interactions, ECM deposition, oxygen and nutrient gradient, which are often missing in cells cultured in 2D monolayers.
- *Extended culture longevity*: spheroids remain viable and functional for longer duration, than 2D cultures, enabling long-term experimentations [95].
- *Improved drug response predictions*: spheroids' three-dimensional structure offer a suitable system where drug penetration is limited, providing a more accurate platform to test drug efficacy and resistance [96].

To date, spheroids have been successfully generated from a wide range of cell types, including Heps [97], mesenchymal stem cells (MSCs) [98], neurons [99], lung cells [100], pre-osteoblasts [101], cancer cells [102] [103] [104], and several other cytotypes (*Figure 11*).

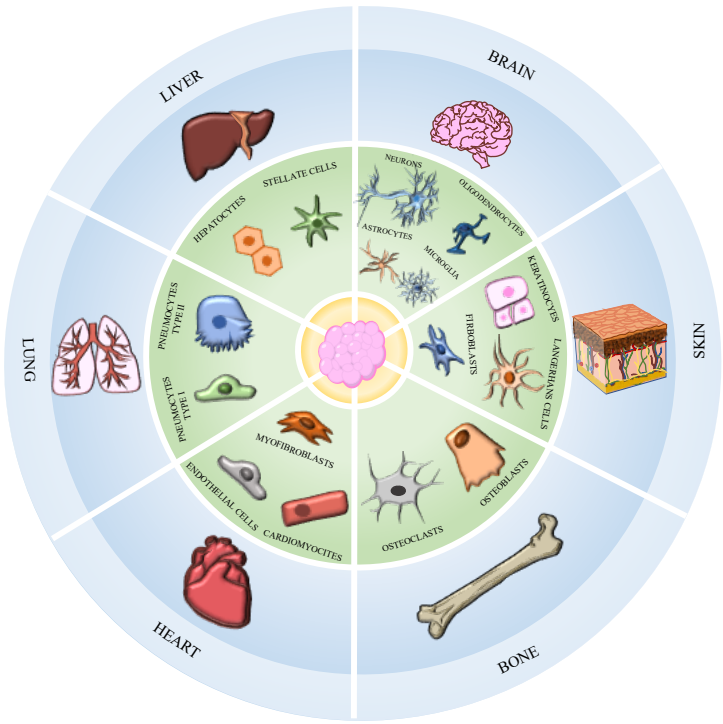

Figure 10 – Representative image of the application of spheroid cultures to model the physiology of different organs. Adapted from Urzì O, et al. 2023 [92].

Spheroids and Extracellular Vesicles research - Owing to their numerous advantages, spheroids have been widely applied by the scientific community for a variety of applications. The most common applications of 3D spheroids include drug discovery and toxicology [105], cancer and tumor microenvironment modeling [106], and tissue engineering and regenerative medicine [107]. In the context of EVs research spheroids are recognized as useful models to provide insights into EVs production, function, and potential therapeutic applications. Broadly this research can be divided into two main lines: one in which spheroids serve as EVs donor cells and one where spheroids are used as target cells. With regards to the first research line, it has been reported how 3D spheroids coltures outperform 2D monolayer systems in EVs production. In fact, spheroids allow physiologically relevant environment cell-cell and cell-ECM interactions, which are crucial for EVs secretion. For instance, it has been reported how mesenchymal stem cells (MSCs) cultured in spheroids produce higher yields of EVs compared to MSCs cultured in 2D monolayers [108]. In addition to that, it has been recently reported that EVs released from 3D cultures exhibit superior therapeutic properties, when compared to their 2D cultured counterparts [109].

These studies collectively highlight how 3D spheroid models can overcome the low secretion yield and difficulties associated with EVs large-scale production, currently representing a

major challenge when isolating EVs from monolayer cultures.

At the same time spheroids can be used as optimal target systems for EVs, providing a complex threedimensional microenviroment where EVs uptake, trafficking, and cellular responses are more accurately replicated than in 2D cultures. Moreover these systems, granting oxygen, nutrients, and signaling molecules gradients, provide a realistic model to study EV-mediated communication [109].

Heps' Spheroids - Heps' spheroids (3D_Heps) are recognized as 3D models able to recapitulate the numerous functions and the multifaceted role that Heps play in the native liver. To begin with, unlike conventional 2D culture, where Heps often undergo rapid loss of hepatic functions, 3D_Heps culture supports the maintenance of mature hepatic phenotypes and long-term functional stability [110].

A comparative study by Bell et al. revealed how primary human Heps cultured as 3D_Heps show higher expression levels of proteins involved in drug absorption, distribution, metabolism, and excretion, when compared to primary human Heps cultured as 2D monolayers, suggesting a higher level of differentiation of these cells when culture as spheroids. Moreover, their proteome remained stable over 14 days, revealing a higher temporal stability, and they showed improved sensitivity to hepatotoxic compounds [111].

In addition to that, 3D_Heps secrete more ECM compared to 2D cultures, thus forming microenvironments more accurately reflecting the *in vivo* liver tissue.

In the light of the numerous advantages above mentioned, 3D_Heps have a wide range of applications including:

- *Hepatotoxicity* and *prediction of drug-induced liver injury* (DILI) [112].
- *Metabolite identification and Pharmacokinetic Studies* [110].
- *Liver Disease Modeling*, including Non-Alcoholic Fatty Liver Disease (NAFLD) [113]. Infectious Liver disease [110], Cholestatic Liber Disease [114].
- *Tissue Engineering and Regenerative Therapy [115][116].*

3.2 Alternative *in vivo* models: zebrafish embryos

Despite the significant potential of 3D alternative models in providing usuful data prior to animal experimentation, *in vivo* research still remains a mandatory step in cancer research. Rodents and higher-order amimal models keep providing invaluable insights into cancer biology and therapeutic development; however, their application, as previously stated, has many practical and logistical drawbacks. This has led to increased interest to alternative *in vivo*

models, including zebrafish (*Danio rerio*) (ZF), a tropical freshwater species native to India, scientifically described for the first time in 1822 by the Scottish physician Francis Hamilton [117] (*Figure 12*).

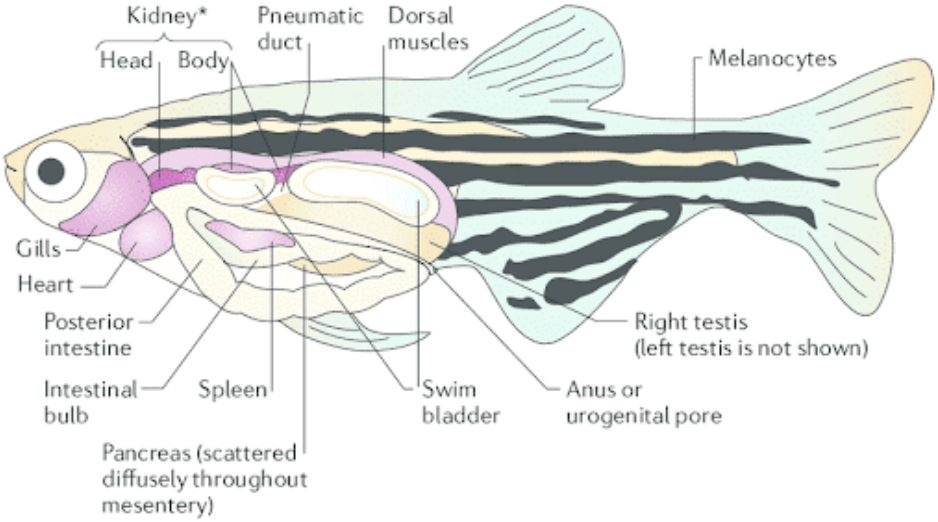

Figure 11 – Representative Image of adult Zebrafish (Liu, Li & Yuan, 2016) [118].

ZF debut in the biomedical fields dates back to 1981, when Streisinger et al. demonstrated several genetic manipulation tecniques in ZF [119], laiding the foundation for its use as a vertebrate model. Since then, ZF model have steadily emerged as a valuable model for studying human physiology and disease. Remarkably, it shares over 70% of its genes with *Homo sapiens*, including many orthologs relevant to human health. One of the main advantages of this model is its small adult size (1.8–3.7 cm) and ability to thrive in dense populations, making it feasible to maintain large numbers of individuals in limited space and at relatively low cost compared to mammalian models. ZF reach sexual maturity quickly, within approximately 10–12 weeks, and can produce up to 300 eggs per spawning, significantly exceeding the reproductive output of rodents.

Zebrafish embryos - A fundamental advantage of the application of ZF lies in their embryos (*Figure 13*), which develop externally and are highly accessible, thus facilitating straightforward genetic and developmental manipulation. Importantly, ZF embryos are not classified as animal experimentation subjects. In fact, according to current Italian legislation (Legislative Decree 26/2014) and European regulation (Directive 2010/63/EU and Commission Implementing Decision 2012/707/EU), animal experimentation is defined as beginning only once the organism acquires autonomous feeding capabilities. Since ZF embryos typically develop this capability after the embryonic stage, generally considered to extend up

to 5 days post fertilizaion (5dpf), their use before this point falls outside animal experimentation laws.

In addition to this, ZF embryos application has many other advantages, including optical clarity, genetic malleability, and high throughput screening [120][121]. Moreover, despite being still at the embryonic stage, ZF embryos already display the formation and early development of multiple organs, such as the heart, brain, eyes, and somites. Of particular relevance to our study, ZF embryos develop a functional liver within four days, showing a similar architecture to mammalians' one and containing cell types morphologically and functionally analogous to their human counterparts [122].

Thanks to these advantageous features, ZF embryos have a wide range of applications hightly relevant to our study, including the creation of transgenic fluorescent models, the development of larval tumor xenografts, and real-time imaging of EVs. These aspects which will be explored in greater detail in the following sections.

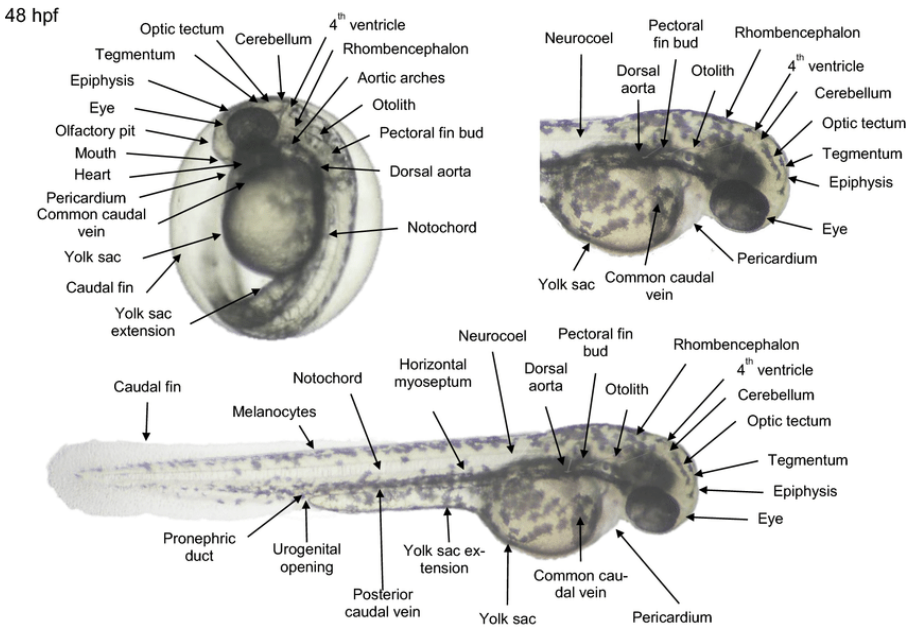

Figure 12. Morphology of normal zebrafish embryo at 2 dpf. Source: von Hellfeld et al. 2020 [123].

Zebrafish transgenic fluorescent models - ZF transgenic models enable the visualization of organs, tissues, or even single cell types within the larva due to microinjection in single-cell stage embryos of DNA constructs containing tissue-specific promoters driving expression of fluorescent reporter genes (e.g., GFP, DsRed, mCherry).

Thanks to this strategy several ZF transgenic lines reporters for several cells and tissues have been estabished, including endothelial cells (under kdrl or fli-1 promoters), neutrophils (under

mpx promoter), macrophages (under mpeg1 or mfap promoters), Schwann cells (under sox10 promoter) [124], bone (under the sp7 promoter) [125] and so on. With particular relevance to our study ZF transgenic lines with labeled liver have been established using specific liver promoters, such as the promoter fatty acid-binding protein 10 (fabp10), coming from the omonymous gene, which is highly expressed in ZF liver. This promoter driving liver-specific expression represents an excellent tool to target transgene expression specifically to Heps, allowing their fluorescent labeling (*Figure 14*) or to express in Heps functional genes for studying liver development, regeneration, and disease [126].

Figure 14. Tg(fabp10a:nls-mcherry) larva at 5 dpf. Adapted from Bambino et al (2019) [127].

Zebrafish larval tumor xenografts - ZF larval xenografts have been broadly used for cancer research and became attractive systems for many application, allowing *in vivo* and real time study of cancer progression and providing a powerful platform to study tumor response to anti-cancer therapies, as well as key processes in the context of cancer evolution, including angiogenesis and metastases development [128].

The establishment of larval tumor xenografts consists in microinjecting cancer cells, tipically fluorescenlty labeled or genetically tagged, in ZF embryos, thus enabling a clear and straightforward visualization of tumor cells *in vivo*. For cancer cells engraftment in ZF embryos four locations have been used in literature, namely the yolk sack, the perivitelline space (PVS), the duct of Cuvier, and the hindbrain ventricle. The yolk sack is the site established by the standard protocol, representing an acellular and delimited compartment where cells can be easily engrafted and visualized. However the yolk environment is more close to a suspension stage rather than an adherent one, which is necessary for tumor cells anchorage-dependent growth [129]. On the other hand, PVS is an avascular region, considered the ideal injection site where to study migration and metastatic behavior, despite being tenchically more difficult to reach. In the light of this Mayra Martinez-Lopez et al. recently published a step by step protocol to generate ZF xenografts by injecting cancer cells in the PVS, addressing the need for a standardized methodology that was previously lacking [130]. This protocol, providing a reliable and reproducible method for ZF larval xenograft generation, was followed for the

purposes of the present research project, as described in Chapter 10, section 10.9. An illustrative image of a zebrafish larval xenograft is shown in *Figure 15*.

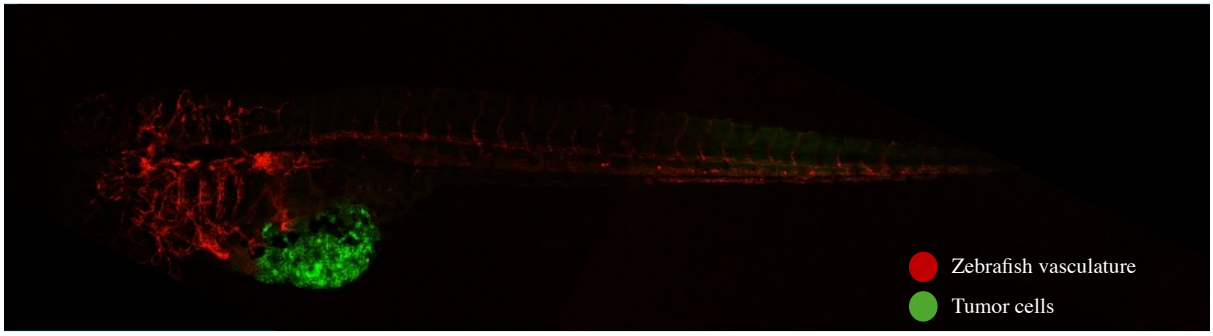

Figure 13 - Demonstrative fluorescent stereomicroscope image of 5dpf ZF embryo Tg(*kdrl*:mCherry-CAAX), exhibiting mCherry-labeled endothelial cells, injected at dpi in the PVS with SW480 CD63-pHluorin+ tumor cells.

Live imaging of EVs within Zebrafish embryos - Due to their small size and transparency, ZF embryos offer an optimal system to study EVs release, transfer, and function, allowing to combine *in vivo* imaging with sub-cellular resolution while preserving the whole-mount imaging scale. Given that, multiple EV-based studies have relied on ZF embryo model. Verweij et al. described ZF embryos application to track endogenous sEVs by expressing the CD63-pHluorin reporter, a fluorescent molecule specifically tagging sEVs, allowing live visualization of their release and revealing for the first time the secretion, journey, and uptake in target cells of individual sEVs secreted *in vivo* [131]. For the purposes of this study, this approach was applied to investigate exogenous sEVs, specifically CRC-sEVs by (i) microinjecting CD63-pHluorin–tagged CRC-sEVs into the ZF duct of Cuvier, and (ii) engrafting genetically tagged CRC cells expressing CD63-pHluorin into ZF embryos to enable *in vivo* production and release of fluorescently tagged sEVs.

CHAPTER 4 – Objectives

This project aims at elucidating the multifaceted role of Heps educated by CRC-sEVs in shaping the hepatic PMN. Since fibrosis and immunosuppression are two key hallmarks of the hepatic PMN, the study will focus particularly on these two interconnected processes through complementary *in vitro* and *in vivo* approaches.

To investigate the immunomodulatory effects of CRC-sEVs on Heps, a two-dimensional *in vitro* model has been selected, providing a controlled setting to monitor Heps–sEVs interactions and to assess how this interaction can alter Heps' immunomodulatory phenotype.

To study Heps' pro-fibrotic properties upon exposure to CRC-sEVs, an hepatocyte spheroid model has been developed, better recapitulating the *in vivo* architecture of the liver microenvironment, including cell-cell and ECM interactions, spatial organization, and matrix deposition. These features are crucial when studying fibrosis-related processes, including EMT and deposition of ECM proteins.

Finally, to bridge to *in vivo* relevance, we aimed to develop a novel zebrafish CRC xenograft model, enabling real-time tracking of interactions among CRC-sEVs, tumor cells, and the hepatic microenvironment, thereby linking our *in vitro* findings to a dynamic living system and strenghtening their biological relevance.

Taken together, the results obtained within this project could provide new evidence for a previously underestimated role of Heps in h-PMN formation. By dissecting both the immunomodulatory and pro-fibrotic roles of CRC-sEV-educated Heps, and developing novel alternative models, namely spheroids and ZF larval xenografts to validate these findings, this study may open new avenues for early intervention and therapeutic targeting of liver metastasis in CRC.

CHAPTER 5 – *In vitro* bidimensional study: CRC-sEVs active hepatocytes immunodulatory properties

It's well established that sEVs can play a key role in immunomodulation, by influencing a wide range of immune cells, including macrophages, dendritic cells, and T lymphocytes. These interactions often promote an immunosuppressive phenotype, facilitating immune evasion and supporting tumor progression. Pucci et al. showed for the first time that CRC-sEVs can modulate the immunomodulatory functions of macrophages, by upregulating the checkpoint inhibitor protein PD-L1 [88]. Given that also Heps possess immunomodulatory properties, for instance they show constitutive expression of PD-L1, which can be enhanced by activated T cells and viral infection [132], we investigated whether CRC-sEVs exposure could similarly induce PD-L1 upregulation in Heps. Such an effect would support a key role of these cells in shaping in liver an immunosuppressive microenvironment, a fundamental feature of hepatic PMN.

5.1 SW480-sEVs are internalized by THLE-2

In accordance with the MISEV 2023 guidelines, SW480-sEVs have been isolated by adopting size exclusion chromatography (SEC), a technique that separates EVs from soluble proteins and other contaminants based on size differences. To this end, using IZON qEVoriginal/35 nm columns (ICO-35) and following the manufacturer's instructions, we optimized a protocol for isolating sEVs released by SW480 cells, which is described in detail in Chapter 6, paragraph 6.6. Briefly, starting from 500 µL of concentrated conditioned medium diluted with 8.5 mL of PBS, six fractions of 400 µL each were collected and analyzed by Dynamic Light Scattering (DLS). Based on the results, reported in *Figure 16A,* fractions 1, 2, and 3 were selected as they were the most enriched in sEVs and free from contaminating soluble proteins. The three selected fractions were pooled and quantified using Nanoparticle Tracking Analysis (NTA), which revealed an average sEVs concentration of 2.8×10^{10} particles/mL (*Figure 16B*). The resulting particles were then characterized by Western blot analysis to assess the presence of specific vesicular markers, including the membrane tetraspanin CD81, Alix, and the Heat Shock Protein 70 (Hsp70). The non-detection of Calnexin, an endoplasmic reticulum-specific protein, confirmed the absence of cellular or subcellular contaminants (*Figure 16C*).

Following that we aimed at investigating the uptake of the sEVs in Heps. To achieve this, the lipophilic dye PKH26 has been used to label EVs. The PKH26-labeled SW480-sEVs were used

to treat the THLE-2 cell line for 3 and 6h. Fluorescent microscopy analysis revealed that, after 3h, the sEVs were already internalized and localized inside the cells (*6D*). Following this, we confirmed the non-toxicity of the selected dose (1.5 x 10^{10} particles/mL) of SW480-sEVs for THLE-2 cells after 24 (*Figure 16E*).

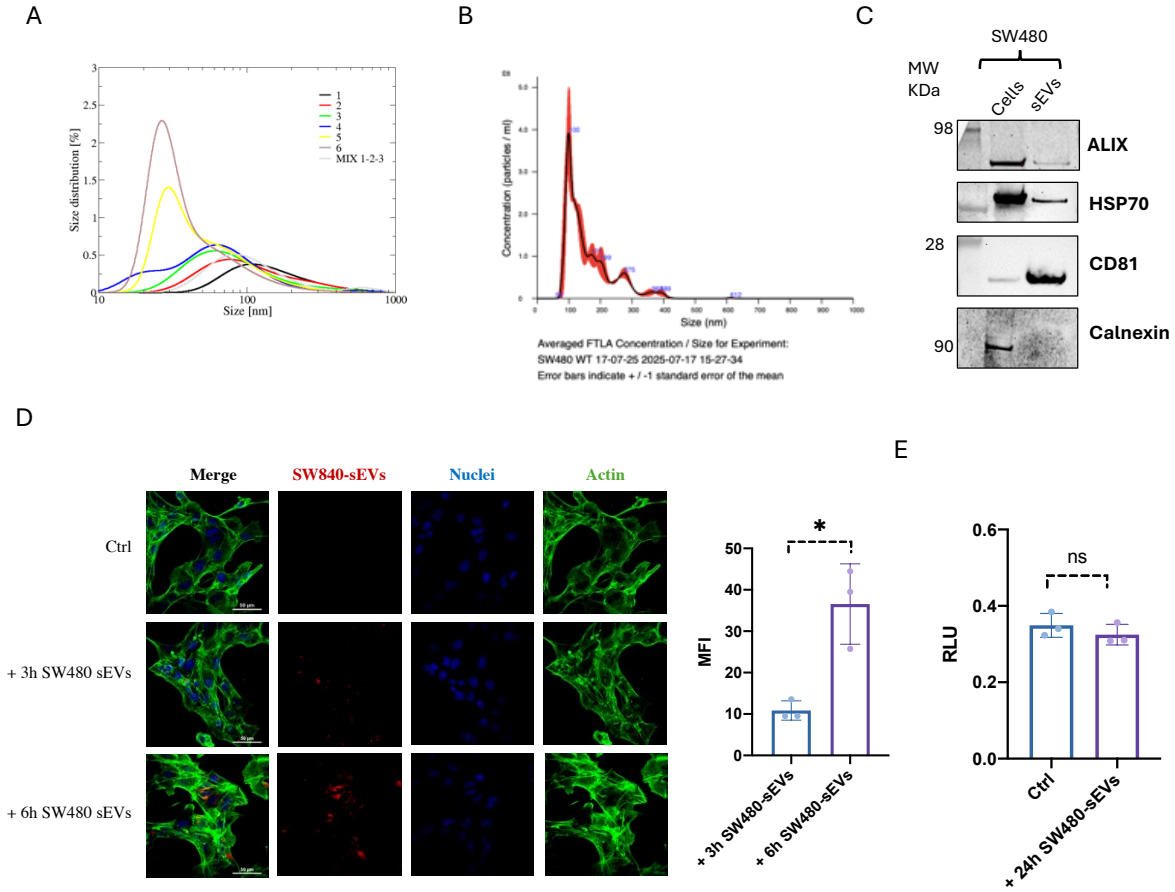

Figure 16 – **A.** Dynamic Light Scattering (DLS) of six different fractions obtained by Size Exclusion Chromatography (SEC) of SW480 conditioned media; **B**. Size distribution of SW480-sEVs obtained through NanoSight analysis; **C**. Western Blot showing the expression level of the sEVs markers CD81, Alix, and HSP70 and of the negative marker calnexin in SW480 cells and SW480-sEVs; **D.** Left panel: confocal micrographs showing the uptake of PKH26-labeled SW480-sEVs in THLE-2 cells treated for 3 and 6h. The sEVs are shown in red; cells nuclei are labeled in blue with Hoechst; actin fibers are stained in green (Actin green); right panel: histograms showing the mean ± standard deviation of PKH26-labeled SW480-sEVs' mean fluorescence intensity (MFI), from three confocal images; **E**. Viability assay of THLE-2 cells exposed to SW480-sEVs for 24h. The histogram shows the mean ± standard deviation from at least three independent experimental replicates. * $p < 0.05$, Ctrl untreated control cells.

5.2 SW480-sEVs increase nuclear PD-L1 expression in THLE-2

Following the premises established by our previous study, in which SW480-sEVs increased PD-L1 expression in M0 macrophages [90], the ability of SW480-sEVs in inducing PD-L1 expression in Heps was investigated. By performing Western Blot analysis, PD-L1 expression was found increased after 3h of treatment with SW480-sEVs (*Figure 17A*). This result complies with various literature data reporting PD-L1 overexpression in the tumor microenvironment (TME) of several types of cancer: PD-L1 is synthetized in the endoplasmic reticulum of TME cells, and subsequently transported to the plasma membrane, allowing the interaction with its receptor PD-1 expressed on T cell surface [133] [134]. Since PD-L1 action as checkpoint inhibitor is strictly dependent on its cell surface localization, cytofluorimetric assays were performed to investigate PD-L1 expression on THLE-2 cells' membrane. Surprisingly PD-L1 expression on Heps' surface was not increased by SW480-sEVs treatment, as shown in *Figure 17B*. Recent literature data have shown that PD-L1 is mainly, but not exclusively, localized at the cellular membrane; in fact, PD-L1 expression has been detected in several cellular compartments, including cells nuclei [135]. In the light of these observations, nuclear PD-L1 (nPD-L1) expression was investigated in THLE-2 cells treated with SW480-sEVs. By performing Western Blot analysis of the nuclear and cytoplasmic fraction (*Figure 17C*) and immunofluorescence (*Figure 17D*) on THLE-2 exposed for 3h to SW480-sEVs, nPD-L1 expression was found increased after 3h of treatment with SW480-sEVs when compared to control cell.

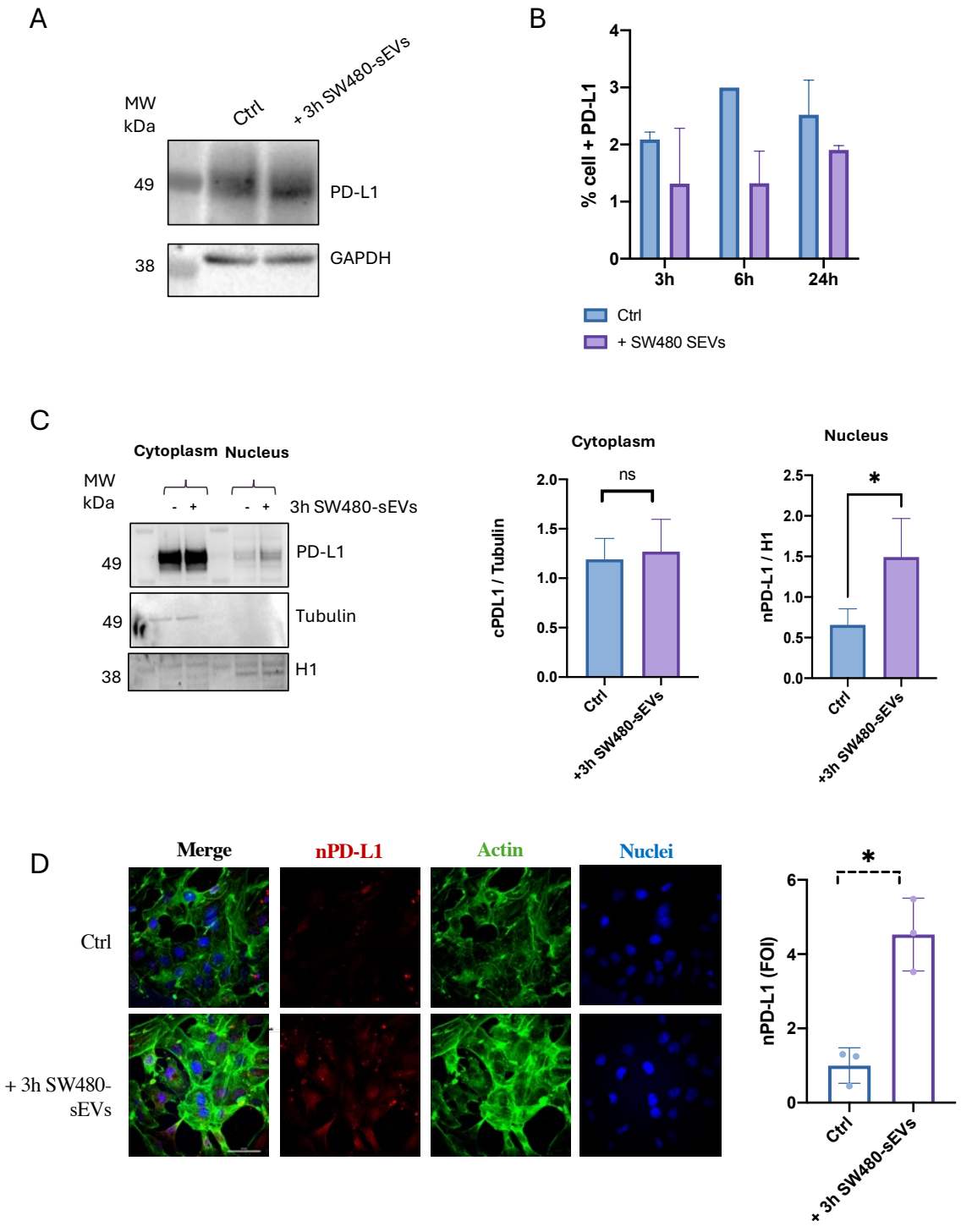

Figure 17 – **A.** Western Blot showing PD-L1 expression in THLE-2 control and exposed to SW480-sEVs for 3h; **B**. Cytofluorimetric analysis of PD-L1 in THLE-2 treated with SW480-sEVs for 3h, 6h, and 24h. The reported values are the mean ± standard deviation of three replicates; **C.** Left panel: Western Blot analysis of PD-L1 expression in both nuclear and cytoplasmic fraction of THLE-2 cells exposed to SW480-sEVs for 3h. Histone 1 (H1) and Tubulin were used as housekeeping markers to confirm successful separation of nuclear and cytoplasmic fractions; right panel: densitometric analysis

of the Western Blot, showing the mean ± standard deviation of at least three replicates; **D.** Left pannel: fluorescent confocal microscope images showing PD-L1 nuclear localization in THLE-2 treated for 3h with SW480-sEVs; Actin Green (green) was used to stain actin fibers; Hoechst (blue) was used to stain the nuclei; PD-L1 is shown in red; right panel: histograms showing the mean ± standard deviation of nuclear PD-L1 fluorescence intensity (MFI) from three confocal images. Ctrl untreated control cells. ns = not significant; * $p < 0.05$

5.3 The increase of nPD-L1 is associated to the expression of VISTA and PD-L2

Several literature data have been reporting the role of nPD-L1 as a crucial effector in transducing intrinsic signals activating alternative pathways supporting tumor progression. Despite these observations, the function of nPD-L1 in CRC liver metastases has not been yet investigated. Recent literature suggests that nPD-L1 can regulate the expression of two alternative immune checkpoint ligands: PD-L2 (Programmed death Ligand 2), known as a second ligand of PD-1 receptor, and VISTA (V-domain Ig Suppressor of T cell Activation) [135]. Similarly to PD-L1, these factors contribute to promote T cell anergy and exhaustion, resulting in tumor escaping from immune attack. VISTA and PD-L2 expression was evaluated by performing Real Time analysis, which revealed a significant increase in mRNA of both factors after 6h of treatment with SW480-sEVs (*Figures 18A-B*). This result was further confirmed by Western Blot analysis and confocal imaging, showing in THLE-2 cells a significant increase in protein expression of VISTA (*Figures 18C-D*) and PD-L2 (*Figures 18E-F*), respectively after 9h and 12h of treatment with SW480-sEVs.

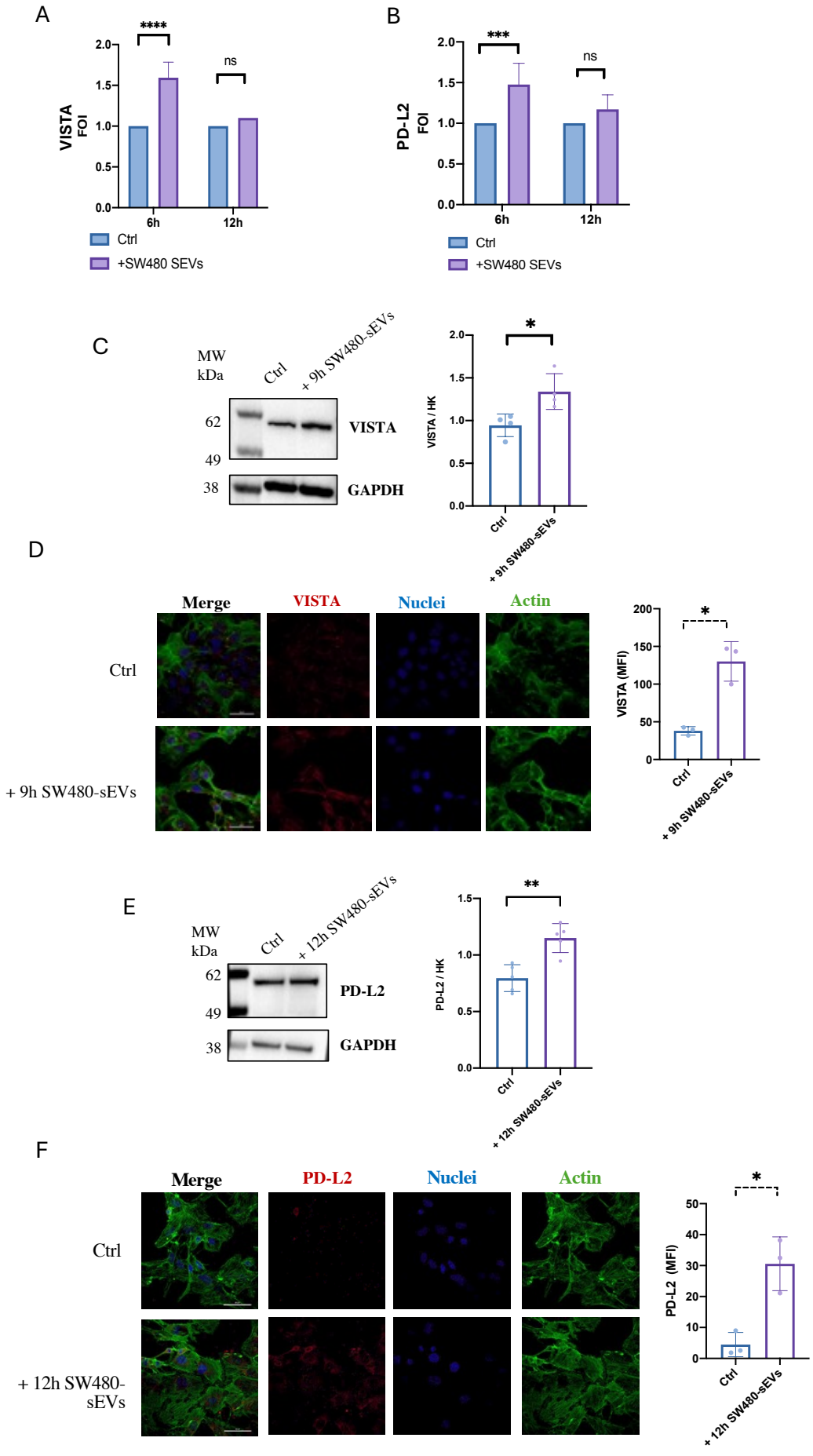
A
****
ns
VISTA FOI
2.0
1.5
1.0
0.5
0.0
6h
12h
Ctrl
+SW480 SEVs
B
***
ns
PD-L2 FOI
2.0
1.5
1.0
0.5
0.0
6h
12h
Ctrl
+SW480 SEVs
C
MW kDa
Ctrl
+ 9h SW480-sEVs
62
49
38
VISTA
GAPDH
*
VISTA / HK
2.0
1.5
1.0
0.5
0.0
Ctrl
+ 9h SW480-sEVs
D
Merge
VISTA
Nuclei
Actin
Ctrl
+ 9h SW480-sEVs
*
VISTA (MFI)
200
150
100
50
0
Ctrl
+ 9h SW480-sEVs
E
MW kDa
Ctrl
+ 12h SW480-sEVs
62
49
38
PD-L2
GAPDH
**
PD-L2 / HK
1.5
1.0
0.5
0.0
Ctrl
+ 12h SW480-sEVs
F
Merge
PD-L2
Nuclei
Actin
Ctrl
+ 12h SW480-sEVs
*
PD-L2 (MFI)
50
40
30
20
10
0
Ctrl
+ 12h SW480-sEVs

Figure 18 – **A**. Real Time PCR of VISTA mRNA expression in THLE-2 exposed for 6 and 12h to SW480-sEVs. The reported values are the mean ± standard deviation of three replicates; **B**. Real Time PCR of PD-L2 mRNA expression in THLE-2 exposed for 6 and 12h to SW480-sEVs. The reported values are the mean ± standard deviation of three replicates; **C.** Left panel: Western Blot analysis of VISTA expression in THLE-2 exposed for 9h to SW480-sEVs; right panel: densitogram showing the mean ± standard deviation from at least three independent experimental replicates; **D.** Left panel: confocal micrographs showing the expression of VISTA in THLE-2 treated or not with SW480-sEVs for 9h. VISTA is marked in red; actin fibers are stained with Actin green. The nuclei are marked in blue with Hoechst; right panel: histograms showing the mean ± standard deviation of VISTA fluorescence intensity (MFI), from three confocal images; **E.** Left panel: Western Blot analysis of PD-L2 expression in THLE-2 exposed for 12h to SW480-sEVs; right panel: densitogram showing the mean ± standard deviation from at least three independent experimental replicates; **F.** Left panel: confocal micrographs showing the expression of PD-L2 in THLE-2 treated or not with SW480-sEVs for 12h. PD-L2 is marked in red; actin fibers are stained with Actin green. The nuclei are marked in blue with Hoechst; right pannel: histograms showing the mean ± standard deviation of PD-L2 fluorescence intensity (MFI) from three confocal images. Ctrl untreated control cells. ns = not significant;* $p < 0.05$; ** $p < 0.005$; *** $p < 0.0005$; ****$p < 0.0001$

5.4 PD-L1 is delivered from SW480-sEVs to the nuclei of THLE-2

As shown by Pucci et al., SW480-sEVs induce in macrophages M0 TLR4/NF-ϰB-dependent overexpression of PD-L1 mRNA levels [88]. To investigate whether the increased PD-L1 expression in Heps' nuclei could be due to an increased transcriptional activity of PD-L1 gene, PD-L1 mRNA levels were investigated by performing Real Time analysis in THLE-2 upon exposure to SW480-sEVs. Surprisingly, PD-L1 mRNA levels were not increased after SW480-sEVs treatment (*Figure 19A*). This last result, together with the early timepoints of PD-L1 protein level increase in THLE-2, previously shown, may suggest a direct delivery of PD-L1 from SW480-sEVs to the Heps, hypothesis supported by PD-L1 expression in SW480-sEVs (*Figure 19B*). This complies with recent literature revealing the role of PD-L1 carried by TD-sEVs in modulating the immunosuppressive features of tissue microenvironment of both primary tumor and PMN [136]. To establish that the increased nuclear form PD-L1 in THLE-2 was originating from donor SW480 cells, a SW480 cell line expressing NanoLuc-HA-tagged PD-L1 (SW480 PD-L1-NanoLuc-HA) was generated (*Figure 19C)* allowing the tracking of vesicle-associated PD-L1 (vPD-L1) delivery and intracellular localization in target cells. The

sEVs sourced from SW480 PD-L1-NanoLuc-HA (SW480-PD-L1-NanoLuc-HA-sEVs) were isolated and characterized by Western Blot analysis (*Figure 19D*) and NTA (*Figure 19E*). Moreover, Western blot analysis confirmed the presence of NanoLuc-HA–tagged PD-L1 in the isolated sEVs by using an antibody against the HA tag (*Figure 19F)*. Once characterized, SW480-PD-L1-NanoLuc-HA-sEVs were used to treat THLE-2 cells in order to assess the delivery of vPD-L1 to the Heps' nuclei. After 3h of exposure, confocal microscopy revealed distinct nuclear localization of the red fluorescence signal corresponding to the HA tag, and thus the tagged vPD-L1, in THLE-2 cells treated with SW480-PD-L1-NanoLuc-HA-sEVs (*Figure 19G*). This suggests that vPD-L1 is delivered from the TD-sEVs to the nuclei of recipient cells, suggesting a novel mechanism by which TD-sEVs can impact the immunomodulatory properties of target cells, by targeting their nuclear activity.

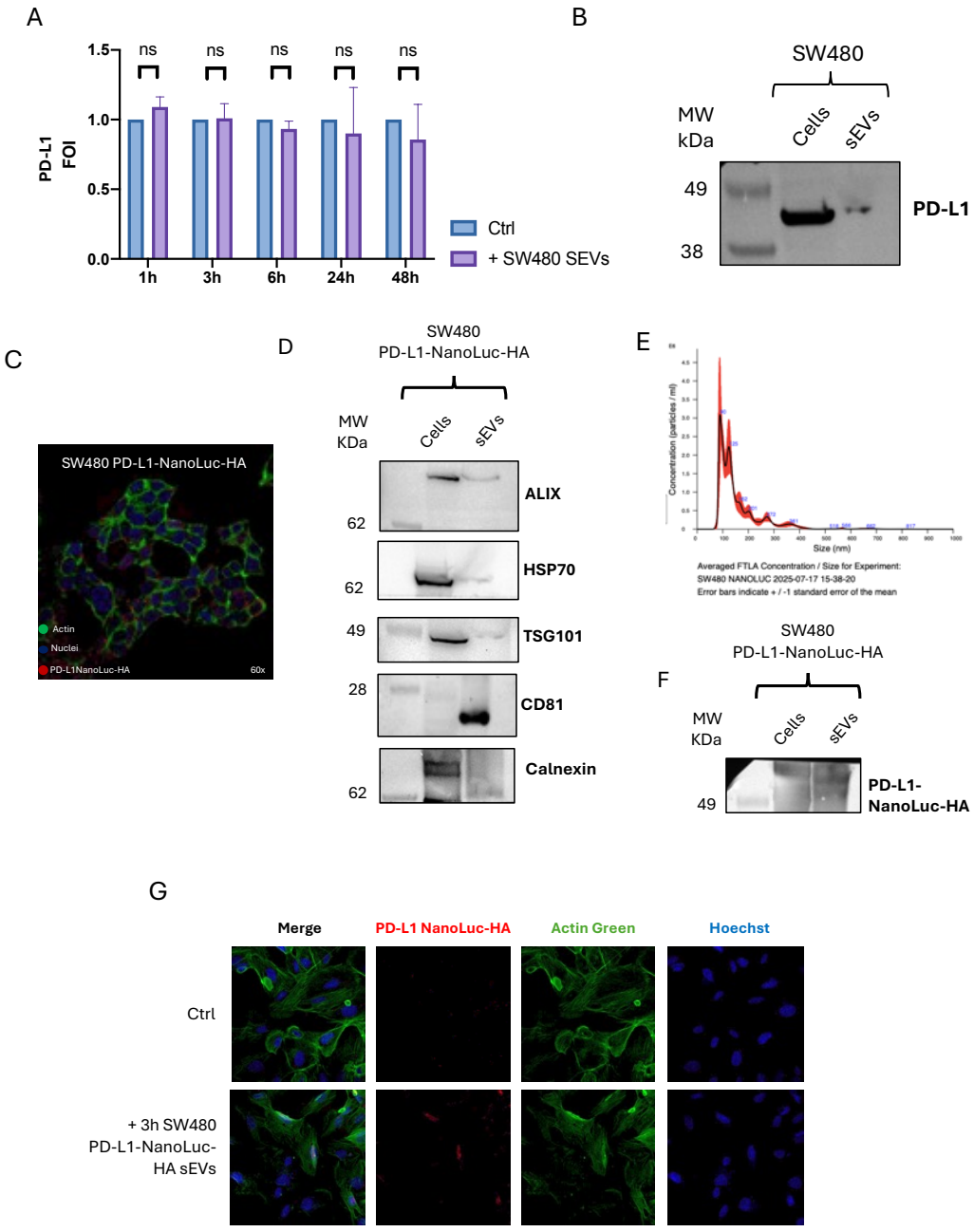

Figure 19 – **A**. Real Time PCR revealing PD-L1 mRNA expression levels in THLE-2 control and treated for 1, 3, 6, 24, and 48h with SW480-sEVs; **B**.Western Blot analysis of PD-L1 expression in SW480-sEVs and SW480 cells; **C**. Confocal micrographs showing the stable cell line SW480 PD-L1-NanoLuc-HA cells. PD-L1-NanoLuc-HA is showed in red. Actin fibers are marked in green with Actin Green. Nuclei are tagged in blue with Hoechst. **D.** Western Blot showing the expression level of the sEVs markers CD81, Alix, Tsg101, and HSP70, and of the negative marker calnexin in SW480 cells and SW480-sEVs; **E.** NTA of the sizes of SW480 PD-L1-NanoLuc-HA-sEVs **F**. Western Blot showing the expression level of PD-L1-NanoLuc-HA in SW480 cells and sEVs; **G**. Confocal micrographs showing the expression of PD-L1-NanoLuc-HA delivered from the sEVs to THLE-2 nuclei after 3h of exposure to SW480 PD-L1-NanoLuc-HA sEVs. PD-L1-NanoLuc-HA is marked in red. Actin fibres are

stained in green with Actin Green. Nuclei are marked in blue with Hoechst. Ctrl untreated control cells. ns = not significant;

5.5 The inhibition of VOR complex blocks the vPD-L1 nuclear delivery

Having demonstrated that the nuclear increased form of PD-L1 originated from CRC-sEVs, we explored the mechanism by which vPD-L1 could be transferred to the nuclei of recipient cells. Rappa et al. described a novel EV-mediated cellular communication mechanism, based on the creation of a sub-nuclear compartment, consisting of late endosomes and nuclear envelope invagination assembling. These nuclear envelope invagination-associated late endosomes mediate the delivery of EVs cargo to the nucleoplasm of recipient cells [71]. It has been reported that this process is mediated by a tripartite protein complex, referred to as VOR complex, consisting of the endoplasmic reticulum–localized vesicle-associated membrane protein (VAMP)-associated protein A (VAP-A), the cytoplasmic oxysterol-binding protein–related protein 3 (ORP3), and late endosome–associated small GTPase Rab7 [72]. Santos et al. recently found that the antifungal compound itraconazole (ICZ) is able to disrupt the binding of Rab7 to ORP3-VAP-A complex, leading to inhibition of sEVs' cargo release to cells nuclei. In the light of this promising finding, the authors synthetized a related compound smaller than ICZ, with the aim to reduce possible side effects of ICZ unrelated to the VOR complex inhibition. This molecule, designated as PRR851, was proved to interfere with VOR complex integrity and to hamper the nuclear delivery of sEVs cargo [137]. The PRR851, kindly provided by Professor Aurelio Lorico (Touro University, Nevada, USA), was used for our experimental activities to investigate whether VOR-mediated late endosomes and nuclear envelope invagination assembling could represent the mechanism underlying vPD-L1 nuclear delivery from CRC-sEVs to THLE-2. Therefore, cells were pre-treated for 10 minutes with PRR851 (10uM) and only then treated with SW480-sEVs. As shown in the confocal images in *Figure 20A*, the sEVs-induced PD-L1 nuclear localization was prevented by PRR851 pre-treatment, thereby suggesting VOR complex involvement in vPD-L1 nuclear delivery from SW480-sEVs. To further confirm these data THLE-2 were also pre-treated with PRR851 and then exposed to SW480-PD-L1-NanoLuc-HA-sEVs. As shown in *Figure 20B*, PD-L1-NanoLuc-HA nuclear localization was prevented by PRR851 pretreatment.

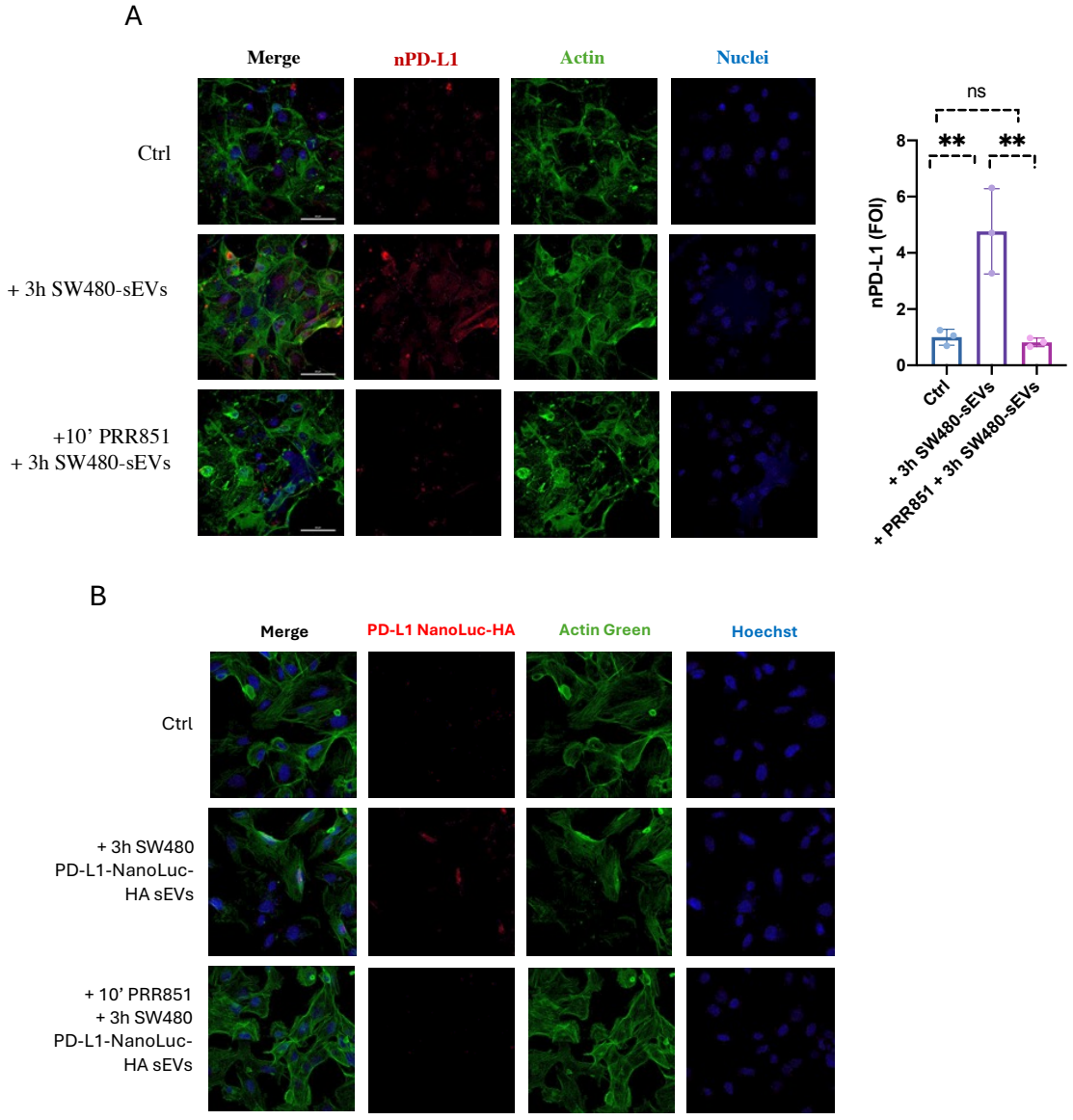

Figure 20 – **A.** Left panel: confocal micrographs showing the expression of PD-L1 in THLE-2 nuclei after 3h of exposure to SW480-sEVs with or without preatretment with PRR851. PD-L1 is marked in red. Actin fibres are stained in green with Actin Green. Nuclei are marked in blue with Hoechst; right panel: histograms showing the mean ± standard deviation of PD-L1 fluorescence intensity (MFI), from three confocal images; **B**. Confocal micrographs showing the expression of PD-L1-NanoLuc-HA delivered from the sEVs to THLE-2 nuclei after 3h of exposure to SW480 PD-L1-NanoLuc-HA sEVs with or without preatretment with PRR851. PD-L1-NanoLuc-HA is marked in red. Actin fibres are stained in green with Actin Green. Nuclei are marked in blue with Hoechst; Ctrl untreated control cells. ns = not significant; ** $p < 0.005$

In accordance with these data, the blockage of the nuclear delivery of vPD-L1 mediated by PRR851 had a negative effect on the induction of PD-L1 targets VISTA and PD-L2 (*Figures 21*), strongly supporting that PD-L1 delivery from sEVs to Heps' nuclei is a crucial event for the overexpression of these two immune checkpoint inhibitors.

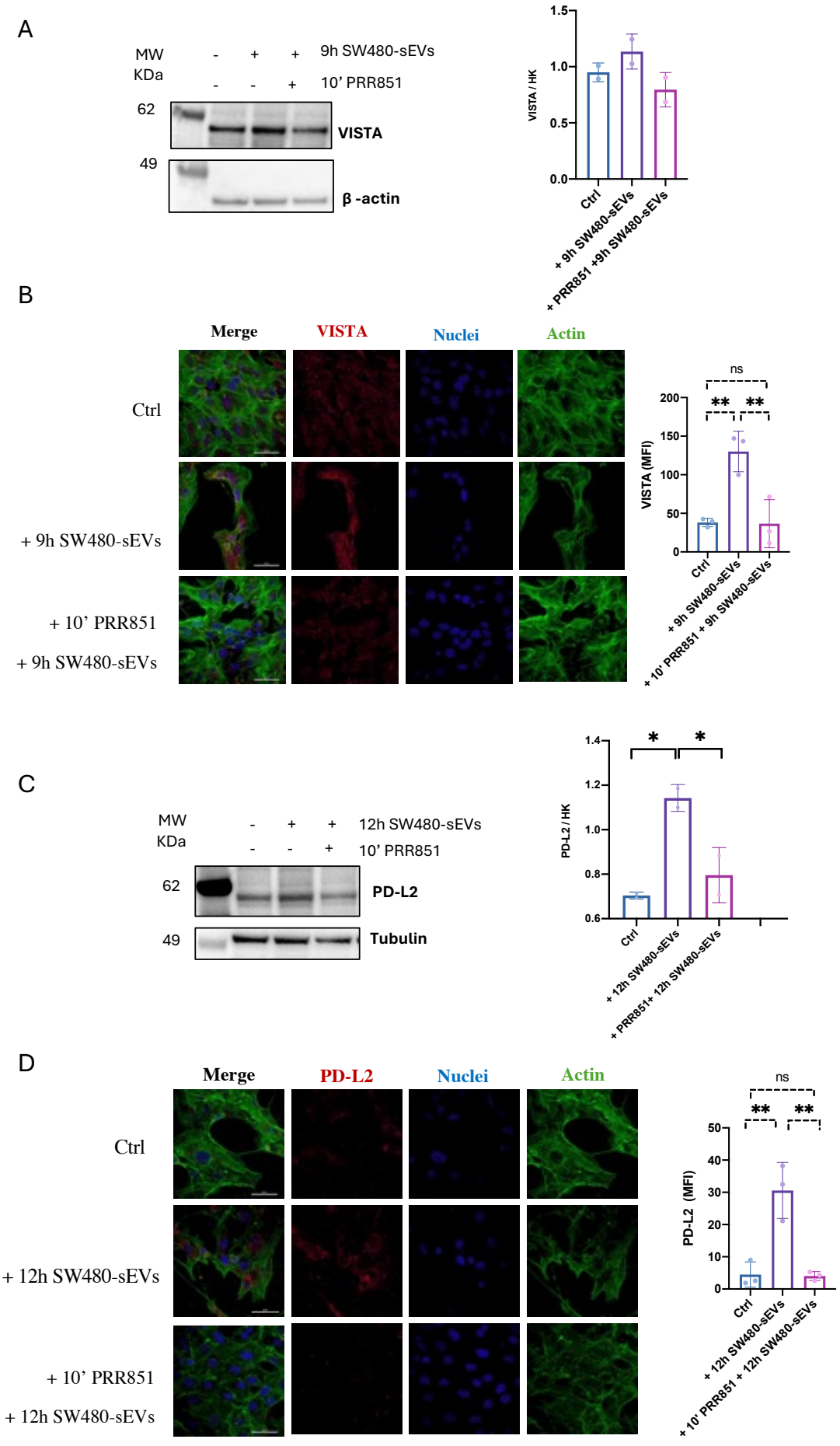
A
MW
KDa
9h SW480-sEVs
10' PRR851
62
VISTA
49
β -actin
VISTA / HK
Ctrl
+ 9h SW480-sEVs
+ PRR851 +9h SW480-sEVs
B
Merge
VISTA
Nuclei
Actin
Ctrl
+ 9h SW480-sEVs
+ 10' PRR851
+ 9h SW480-sEVs
VISTA (MFI)
ns
C
MW
KDa
12h SW480-sEVs
10' PRR851
62
PD-L2
49
Tubulin
PD-L2 / HK
+ 12h SW480-sEVs
+ PRR851+ 12h SW480-sEVs
D
Merge
PD-L2
Nuclei
Actin
Ctrl
+ 12h SW480-sEVs
+ 10' PRR851
+ 12h SW480-sEVs
PD-L2 (MFI)

Figure 21 – **A.** Left panel: Western Blot showing the expression of VISTA in THLE-2 exposed for 9h to SW480-sEVs with or without the pretreatment with PRR851; right panel: densitogram showing the mean ± standard deviation from two independent experimental replicates; **B.** Left panel: confocal micrographs showing the expression of VISTA delivered from the sEVs to THLE-2 nuclei after 9h of exposure to SW480-sEVs with or without preatretment with PRR851. VISTA is marked in red. Actin fibres are stained in green with Actin Green. Nuclei are marked in blue with Hoechst; right panel: istograms showing the mean ± standard deviation of VISTA fluorescence intensity (MFI) from three confocal images; **C.** Left panel: Western Blot showing the expression of PD-L2 in THLE-2 exposed for 12h to SW480-sEVs with or without the pretreatment with PRR851**;** right panel**:** densitogram showing the mean ± standard deviation from two independent experimental replicates; **D.** Left panel: confocal micrographs showing the expression of PD-L2 delivered from the sEVs to THLE-2 nuclei after 12h of exposure to SW480-sEVs with or without preatretment with PRR851. PD-L2 is marked in red. Actin fibres are stained in green with Actin Green. Nuclei are marked in blue with Hoechst; right panel: histograms showing the mean ± standard deviation of PD-L2 fluorescence intensity (MFI) from three confocal images; Ctrl untreated control cells, ns= not significant, * $p < 0.05$, ** $p < 0.005$

5.6 CRC/P-sEVs control THLE-2 immunomodulatory properties

To corroborate our *in vitro* results achieved via sEVs sourced from SW480, THLE-2 were treated with sEVs isolated from the plasma of CRC patients (CRC/P-sEVs), which have been previously characterized by TEM, NTA, and protein analysis [90]. In accordance with what has been found with SW480-sEVs, we observed that also CRC/P-sEVs expressed PD-L1 (*Figure 22A*). Following the assessment THLE-2 ability to interact with CRC/P-sEVs (*Figure 22B*) and the assessment of THLE-2 unaltered viability after exposure to 1.5 $x10^{10}$/mL of CRC/P-sEVs [90], the effect of CRC/P-sEVs on Heps' immunomodulatory properties was investigated. In accordance with the *in vitro* results previously shown, also CRC/P-sEVs were able to determine in THLE-2 an increased nPD-L1 expression upon 3h of treatment (*Figure 22C*).

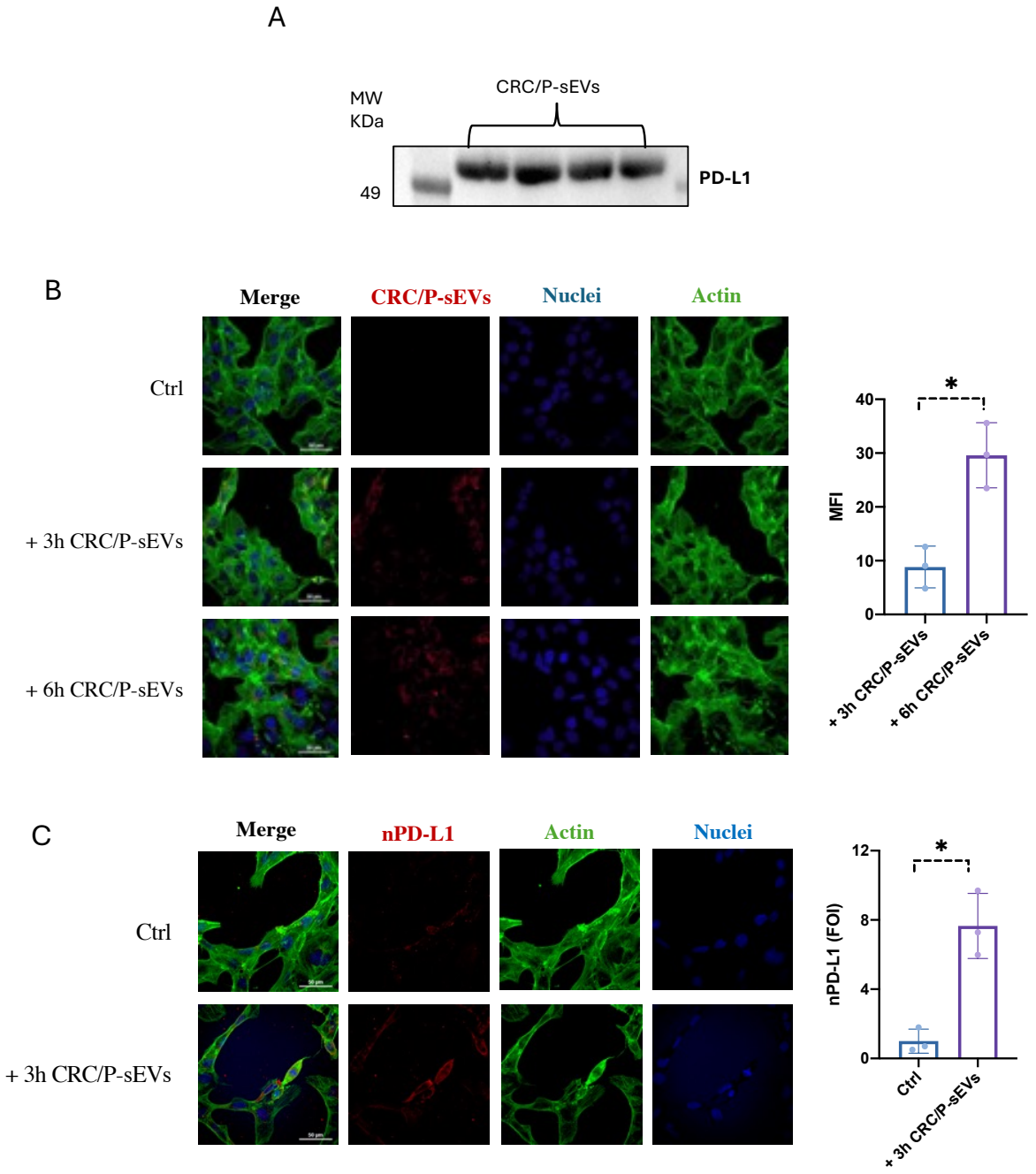

Figure 22 – **A**. Western Blot analysis of PD-L1 in sEVs isolated form the plasma of CRC patients; **B.** Left panel: uptake assay of PKH26-labeled CRC/P-sEVs in THLE-2 after 3 and 6h exposure. CRC/P-sEVs are marked in red; actin fibers are marker with Actin Green. Nuclei are labeled with Hoechst (blue); right panel: histograms showing the mean ± standard deviation of PKH26-labeled CRC/P-sEVs mean fluorescence intensity (MFI) from three confocal images; **C.** Left panel: fluorescent confocal microscope images showing PD-L1 nuclear localization in THLE-2 treated for 3h with CRC/P-sEVs; PD-L1 is marked in red. Actin Green (green) was used to stain actin fibers; Hoechst (blue) was used to stain the nuclei; right panel**:** histograms showing the mean ± standard deviation of nPD-L1 mean fluorescence intensity (MFI), from three confocal images. Ctrl untreated control cells. * $p < 0.05$

Moreover, in compliance with the previous findings, we observed in THLE-2 an increased expression of both VISTA (*Figures 23A-B*) and PD-L2 (*Figures 23C-D*) expression levels as a consequence of CRC/P-sEVs treatment.

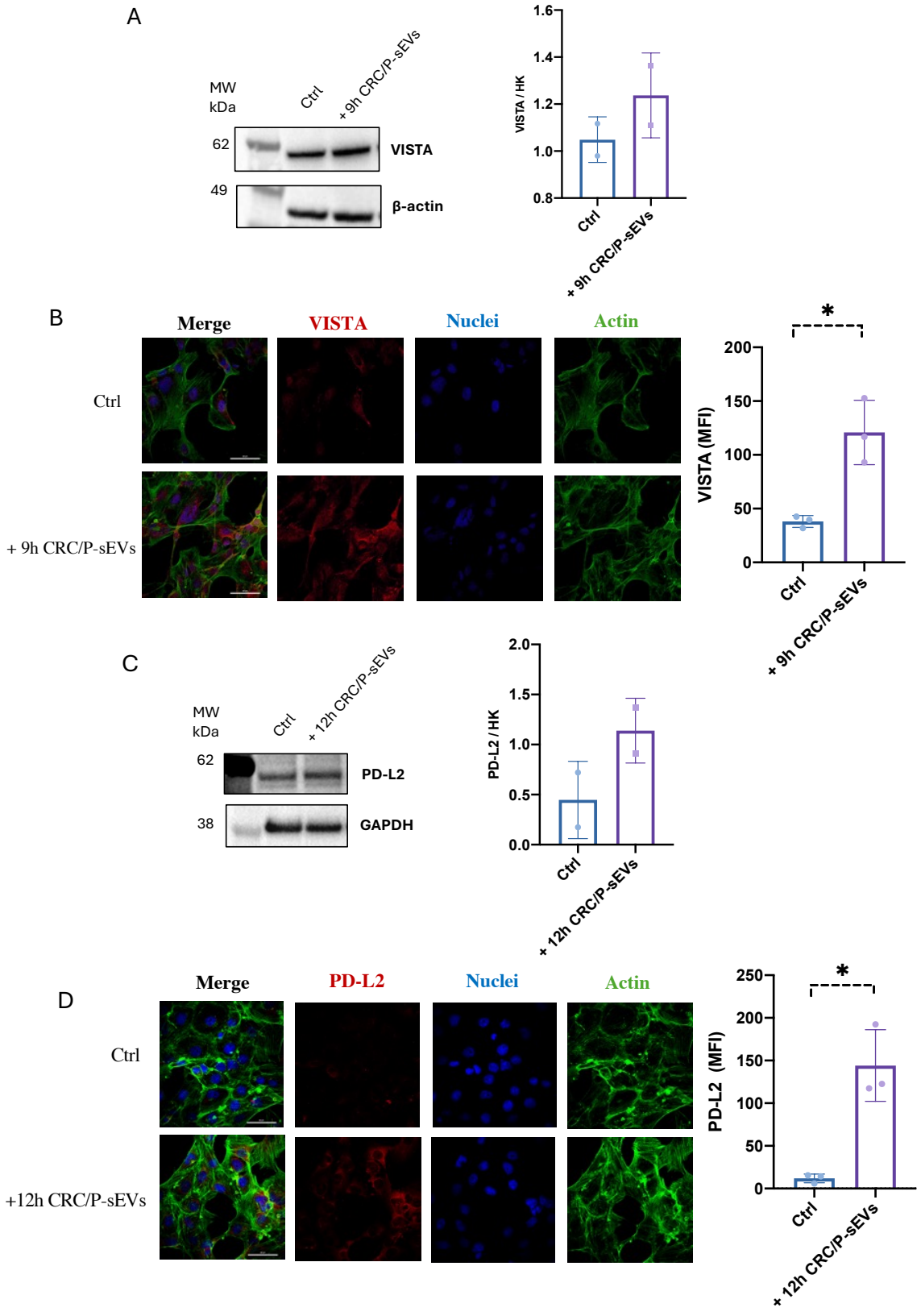
A
MW
kDa
Ctrl
+ 9h CRC/P-sEVs
62
VISTA
49
β-actin
VISTA / HK
1.6
1.4
1.2
1.0
0.8
Ctrl
+ 9h CRC/P-sEVs
B
Merge
VISTA
Nuclei
Actin
Ctrl
+ 9h CRC/P-sEVs
VISTA (MFI)
200
150
100
50
0
*
Ctrl
+ 9h CRC/P-sEVs
C
MW
kDa
Ctrl
+ 12h CRC/P-sEVs
62
PD-L2
38
GAPDH
PD-L2 / HK
2.0
1.5
1.0
0.5
0.0
Ctrl
+ 12h CRC/P-sEVs
D
Merge
PD-L2
Nuclei
Actin
Ctrl
+12h CRC/P-sEVs
PD-L2 (MFI)
250
200
150
100
50
0
*
Ctrl
+ 12h CRC/P-sEVs

Figure 23 – A. Left panel: Western Blot analysis of VISTA in THLE-2 exposed for 9h to CRC/P-sEVs; β-actin was used as housekeeping protein; right panel: densitogram showing the mean ± standard deviation from two independent experimental replicates; **B.** Left panel: confocal micrographs showing the expression of VISTA in THLE-2 after 9h of exposure to CRC/P-sEVs. VISTA is marked in red. Actin fibres are stained in green with Actin Green. Nuclei are marked in blue with Hoechst; right panel: histograms showing the mean ± standard deviation of VISTA mean fluorescence intensity (MFI) from three confocal images; **C.** Left panel: Western Blot analysis of PD-L2 in THLE-2 treated for 12h with CRC/P-sEVs; GAPDH was used as housekeeping protein; right panel: densitogram showing the mean ± standard deviation from two independent experimental replicates; **D.** Left panel: confocal micrographs showing the expression of PD-L2 in THLE-2 after 12h of exposure to CRC/P-sEVs. PD-L2 is marked in red. Actin fibers are stained in green with Actin Green. Nuclei are marked in blue with Hoechst; right panel: histograms showing the mean ± standard deviation of PD-L2 mean fluorescence intensity (MFI) from three confocal images; *Ctrl* untreated control cells. * $p < 0.05$;

To confirm that the observed effects were specifically attributable to tumor-derived sEVs, sEVs were isolated from the plasma of healthy donors (HS-sEVs), as previously described and used to treat THLE-2 cells. After verifying the ability of HS-sEVs to interact with THLE-2 cells through uptake assays (*Figure 24A*) and confirming that the selected dose was non-toxic to the target cells [90], the effects of HS-sEVs on THLE-2 were evaluated.

In contrast to what we observed in THLE-2 cells exposed to CRC-sEVs, the treatment with HS-sEVs did not induce an increased nuclear translocation of PD-L1 (*Figure 24B*), nor did it upregulate the downstream targets VISTA (*Figure 24C*) and PD-L2 (*Figure 24D*), thus highlighting the specificity of the previously observed immunomodulatory effects to tumor-derived sEVs.

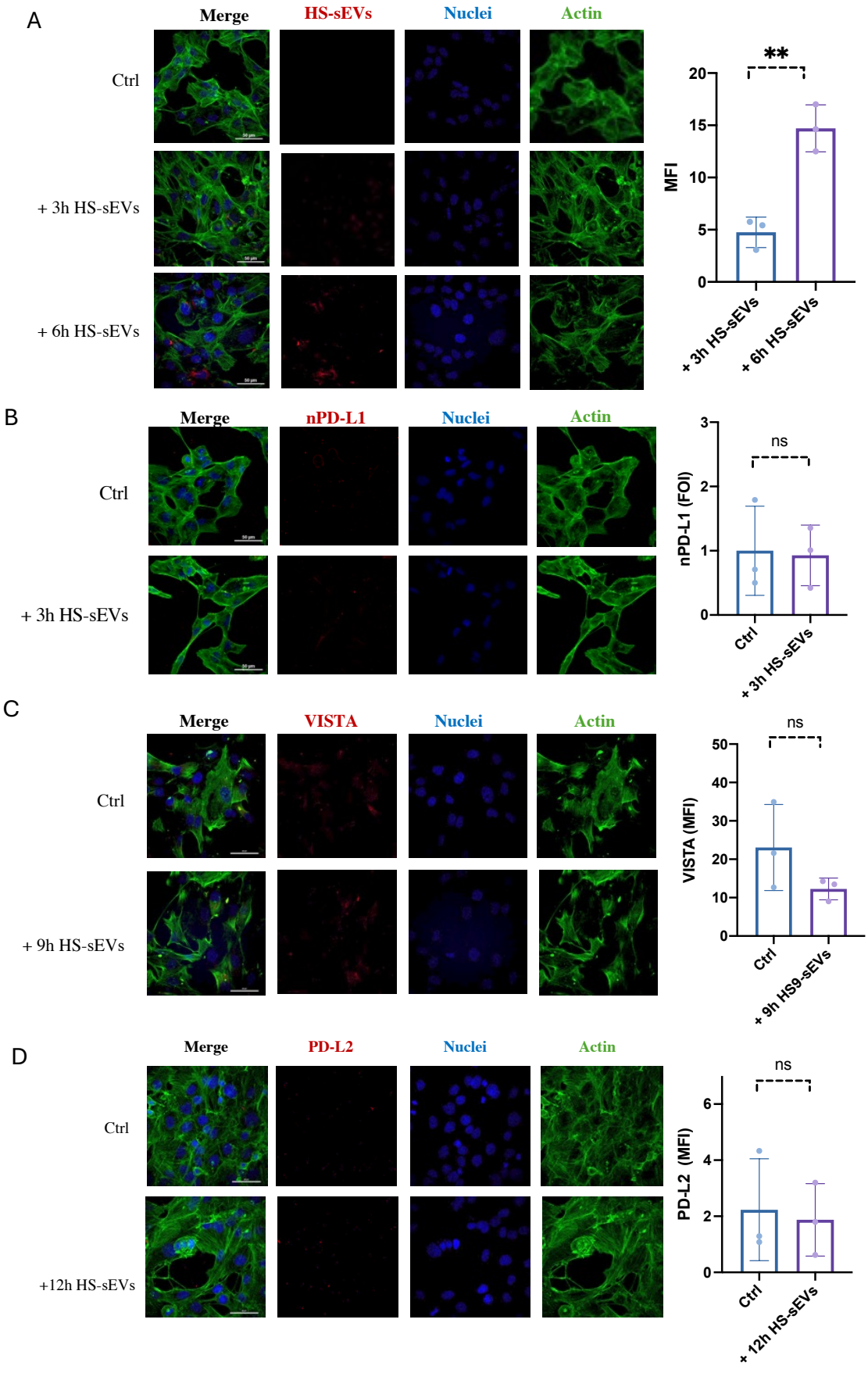
A
Merge
HS-sEVs
Nuclei
Actin
Ctrl
+ 3h HS-sEVs
+ 6h HS-sEVs
**
MFI
20
15
10
5
0
+ 3h HS-sEVs
+ 6h HS-sEVs
B
Merge
nPD-L1
Nuclei
Actin
Ctrl
+ 3h HS-sEVs
ns
nPD-L1 (FOI)
3
2
1
0
Ctrl
+ 3h HS-sEVs
C
Merge
VISTA
Nuclei
Actin
Ctrl
+ 9h HS-sEVs
ns
VISTA (MFI)
50
40
30
20
10
0
Ctrl
+ 9h HS9-sEVs
D
Merge
PD-L2
Nuclei
Actin
Ctrl
+12h HS-sEVs
ns
PD-L2 (MFI)
6
4
2
0
Ctrl
+ 12h HS-sEVs

Figure 24 – A. Left panel: uptake assay of PKH26-labeled HS-sEVs in THLE-2 after 3 and 6h exposure. HS-sEVs are marked in red; actin fibers are marker with Actin Green. Nuclei are labeled with Hoechst (blue); right panel: histograms showing the mean ± standard deviation of PKH26-labeled HS-sEVs mean fluorescence intensity (MFI) from three confocal images; **B.** Left panel: confocal micrographs showing the expression of PD-L1 after 3h of exposure to HS-sEVs. PD-L1 is marked in red. Actin fibres are stained in green with Actin Green. Nuclei are marked in blue with Hoechst; right panel: histograms showing the mean ± standard deviation of nPD-L1 fluorescence intensity (MFI) from three confocal images; **C.** Left panel: confocal micrographs showing the expression of VISTA in THLE-2 after 9h of exposure to HS-sEVs. VISTA is marked in red. Actin fibres are stained in green with Actin Green. Nuclei are marked in blue with Hoechst; right panel: histograms showing the mean ± standard deviation of VISTA mean fluorescence intensity (MFI) from three confocal images; **D**. Left panel: confocal micrographs showing the expression of PD-L2 in THLE-2 after 12h of exposure to HS-sEVs. PD-L2 is marked in red. Actin fibres are stained in green with Actin Green. Nuclei are marked in blue with Hoechst; right panel: histograms showing the mean ± standard deviation of PD-L2 mean fluorescence intensity (MFI) from three confocal images; Ctrl untreated control cells, ns = not significant, ** $p < 0.005$

5.7 Future outlooks: validation of nPD-L1 immunomodulatory role in hepatocytes

To further prove the functional role of sEVs-derived nPD-L1 in promoting the expression of the immunosuppression-related genes VISTA and PD-L2, the PD-L1 knockdown stable cell line SW480 shPD-L1 was generated. The knock down was performed in collaboration with Utrecht University by using a Tet-ON–inducible shRNA targeting PD-L1 mRNA, as thoroughly described in the Chapter 6, section 6.5. This system allows to control the PD-L1 silencing by adding doxycycline, which activates the transcription of the shRNA targeting PD-L1 mRNA. In addition to SW480 shPD-L1 cells, the stable SW480 cell line silenced for the Green Fluorescent Protein (GFP) was generated (shGFP SW480). The shGFP SW480 cells, exhibiting the silencing of GFP, a non-endogenous protein in SW480 cells, served as a negative control to ensure the absence of non-specific effects caused by the shRNA expression or the transduction process itself.

The PD-L1 silencing was verified by performing Western Blot analysis in SW480 WT (with or without doxycycline), SW480 shGFP (with or without doxycycline), and SW480 shPD-L1 (with or without doxycycline). As shown in *Figure 25A*, the shPD-L1 SW480 exposed to doxycycline (2 μg/mL) for 48h displayed a lower expression of PD-L1, compared to the other cells, confirming a successful knockdown of the protein following 48h of exposure to doxycycline 2 μg/mL. Subsequently, shPD-L1 SW480 were used as a source of shPD-L1 sEVs.

After 48h of incubation with 2ug/mL doxycycline, conditioned media were collected and sEVs isolated by SEC. The shPD-L1 SW480 sEVs thus obtained were characterized by Western Blot analysis (*Figure 25B*). These preliminary results confirmed the relevance of SW480 shPD-L1 cells in validating the role of vesicle-derived nPD-L1 in promoting the immunomodulatory properties of Heps. Building on this, we plan to investigate the expression of VISTA and PD-L2 in THLE-2 upon exposure to both shPD-L1 SW480-sEVs and WT SW480-sEVs. In addition to that, to further define the functional role of CRC-sEV-educated Heps, as well as the contribution of VISTA and PD-L2 upregulation in response to the nuclear delivery of PD-L1 via CRC-sEVs, co-culture experiments involving CRC-sEVs-educated Heps and T cells will be conducted. These experiments aim to determine whether the observed immunomodulatory effects driven by Heps overexpression of VISTA and PD-L2 can impair T cell activation, thus supporting the creation of an immunosuppressed microenvironment.

This approach would highlight the significant contribution of Heps educated by CRC-sEVs in promoting tumor immune evasion through the expression of alternative immune checkpoint proteins; moreover, it would point out a new mechanism of immunomodulation mediated by CRC-sEVs, based on PD-L1 nuclear delivery and the consequent transcriptional upregulation of its target VISTA and PD-L2.

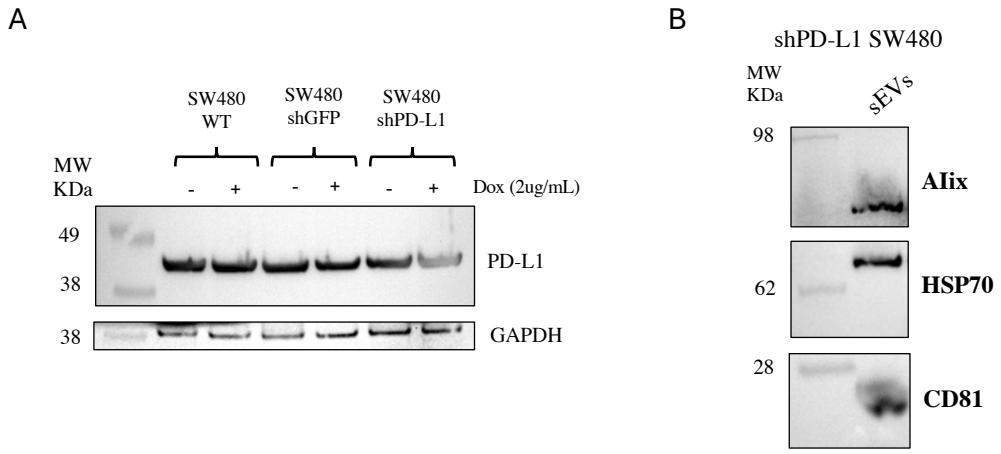

Figure 25 – A. Western Blot analysis of PD-L1 expression in SW480 WT (with or without doxycycline), SW480 shGFP (with or without doxycycline), and SW480 shPD-L1 (with or without doxycycline); **B**. Western Blot showing the expression level of the sEVs markers CD81, Alix, and HSP70 in SW480 shPD-L1-sEVs.

CHAPTER 6 – Material and Methods: *In vitro* bidimensional study

6.1 Cell colture

THLE-2 (ATCC, Manassas, VA), healthy human epithelial cells isolated from the left lobe of liver and immortalized with the catalytic subunit of human telomerase (hTERT), were cultured in RPMI 1640 medium (Euroclone,UK) supplemented with 10% fetal bovine serum (FBS, Euroclone UK), 1% penicillin (100 U/mL) and streptomycin (100µg/mL), epidermal growth factor (EGF), 5 ng/mL and phosphoethanolamine (PEA) 70 ng/mL at 37 ºC with 5% CO_2. Cells were maintained in flasks with a coating obtained from a solution of 0.03 mg/mL bovine collagen type I (Advanced Biomatrix, San Diego region, California, USA), and 0.01 mg/mL bovine albumin (SigmaAldrich, St Louis, MO, USA).

The CRC cell line SW480 (ATCC CCL-228) derived from a pre-metastatic primary tumor were used as a source of CRC-sEVs. SW480 cells were maintained in RPMI 1640 medium (Euroclone, UK) supplemented with 10% fetal bovine serum (FBS; Euroclone, UK), 2 mM L-glutamine (Euroclone, UK), 100 U/mL penicillin and 100 µg/mL streptomycin (Euroclone, UK). FBS (EU-approved, South American origin; Euroclone, UK) was ultracentrifuged at 100,000 × *g* for 105 minutes using a Type 70 Ti fixed-angle rotor to deplete animal-derived sEVs that could otherwise contaminate the experimental samples [138].

HEK-293T cells were used as packaging cells for lentiviral particles production. Cells were mantained in DMEM (Euroclone, UK) supplemented with 10% fetal bovine serum (FBS; Euroclone, UK), 2 mM L-glutamine (Euroclone, UK), 100 U/mL penicillin and 100 µg/mL streptomycin (Euroclone, UK).

6.2 Lentiviral particles production

For the production of lentiviral particles, conducted in Utrecht University, HEK-293T cells were used as packaging cells. The cells were seeded in 10 cm² Petri dishes. Once they reached 50–60% confluence, the cells were transfected with a mixture of the following plasmids:

- 15 µg of the gene of interest (PD-L1-EGFP or shPD-L1);
- 10 µg of the psPAX2 vector, which encodes Gag, Pol, Rev, and Tat (Addgene Plasmid #12260, 2nd generation lentiviral packaging plasmid);
- 5 µg of the pMD2.G vector, which encodes the VSV-G envelope protein (Addgene Plasmid #12259);

- PEI MAX stock (PEI MAX® – Polysciences Cat.#24765-2) at a ratio of 3 µL per µg of DNA;
- Opti-MEM (Gibco™ Cat.#31985070), added to reach a final volume of 1.2 mL.

The transfection mixture was added to the cells, which were then transferred to a biosafety level II (ML-II) laboratory and incubated overnight at 37°C in 5% CO_2. The next day, the medium was removed and replaced with fresh DMEM.

On the following day, the supernatant containing the lentiviral particles was collected and filtered through 0.45 µm filters to remove cellular debris. The lentiviral suspension was then stored at −80°C.

6.3 Generation of SW480 PD-L1-NanoLuc-HA cell line

To generate the stable cell line SW480 PD-L1-NanoLuc-HA, a knock in was performed via CRISPR/Cas9. SW480 were seeded in 6 multiwells at the density of 1.5 x 10^5 cells/well. After 24h, the cells were co-transfected with two plasmids respectively containing the information for PD-L1-NanoLuc.HA and for Cas9 and gRNA. Both plasmids, the HDR template for PD-L1-NanoLuc-HA cloned in a pBluescript backbone, and the gRNA for PD-L1 cloned in pSpCas9(BB)-2A-Puro (PX459) V2.0 (Addgene #62988) backbone containing the gene resistance for puromycin (*Figure 26*), were kindly provided by Utrecht University.

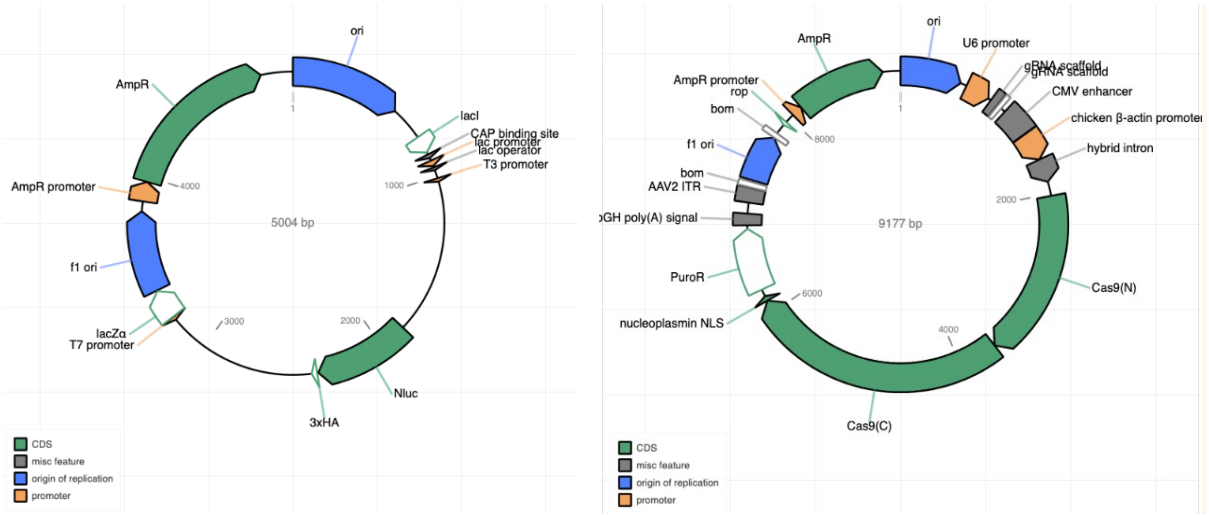

Figure 26 – Left panel: plasmid containing HDR template for PD-L1-NanoLuc-HA cloned in a pBluescript backbone; right panel: plasmid containing the information for the gRNA for PD-L1 cloned in pSpCas9(BB)-2A-Puro (PX459) V2.0 (Addgene #62988) backbone containing the gene resistance for puromycin.

For the transfection, the transfection reagent JetOptimus (Polyplus - SKU PO 201000001) was used. The plasmidic DNA was diluted in jetOptimus Buffer. Subsequently the JetOptimus Reagent was dded to the solution, which was then rapidly vortexed and added to the cells. Approximately 48h after the transfection, cells were selected by using the puromycin (10 µg/mL). For the single cell sorting of SW480-PD-L1-NanoLuc-HA cells, the cells were detached by using trypsin, centrifuged, and resuspended in 10% FBS diluted in PBS. The cells were subsequently single sorted through the Cell Sorter FACSAria and seeded in each in a well from a 96 multiwell. After approximately two weeks, the single clones were tested for the presence of the NanoLuc, by performing the Nano-Luciferase Assay System (Promega), thereby allowing the selection of the clones where the knock in was successful.

6.4 Generation of SW480 shPD-L1

To generate the stable SW480 shPD-L1 cells, SW480 cells were infected with lentiviral particles carrying a Tet-ON–inducible shRNA targeting PD-L1 mRNA, containing puromycin resistance, kindly provided by Utrecht University (*Figure 27*).

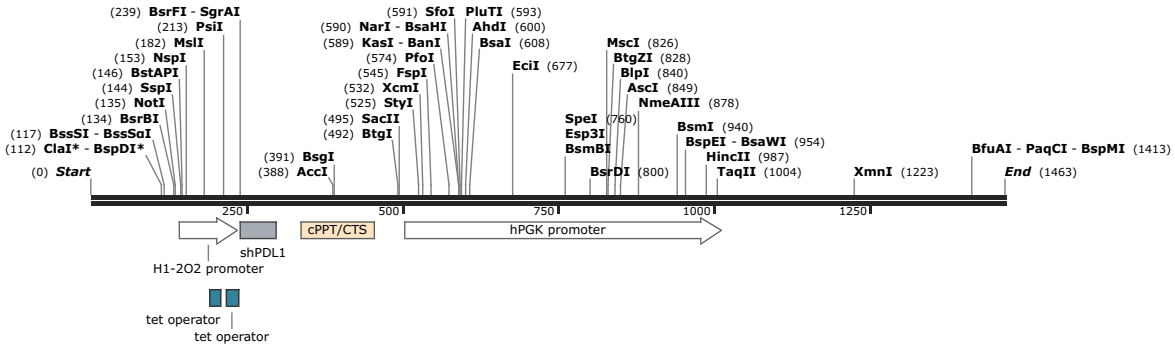

Figure 27 – Sequencing of the Tet-ON–inducible shRNA targeting PD-L1 mRNA.

Cells were seeded in 6-well plates and, upon reaching approximately 50% confluency, the medium was replaced with RPMI 1640 (Euroclone, UK) supplemented with 10% fetal bovine serum (FBS), 1% penicillin (100 U/mL), and streptomycin (100 μg/mL). Subsequently the virus was added. To enhance transduction efficiency, 8 μg/mL polybrene was added to the medium. After 24 hours, the medium was replaced with fresh culture medium. Selection of successfully transduced cells was performed using puromycin (6 μg/mL). To ensure compatibility with the Tet-inducible system, cells were maintained in medium containing tetracycline-free FBS (Tetracycline free FBS Premium FBS-TET-12A). For induction of shRNA expression, 2 μg/mL doxycycline (ANT-DOXBL-1 RepTor Reagent Kit) was added

for 48 hours to activate PD-L1 silencing. In addition to that, the SW480 shGFP cell lines was also generated following the same protocol above described and used as control for our study.

6.5 Isolation of sEVs from SW480 by SEC

SEVs were isolated from the conditioned medium collected after 48 hours of culture from SW480 cells. For this purpose, SW480 cells were seeded at a density of 35,000 cells/cm^2 in T175 flasks in RPMI 1640 culture medium (Euroclone UK), supplemented with 10% SEV-depleted FBS (Euroclone UK), 2 mM L-Glutamine (Euroclone UK), and 1% penicillin (100 U/mL) and streptomycin (100 μg/mL).

To deplete animal-derived sEVs, FBS was subjected to ultracentrifugation at 100,000 × g for 105 minutes using a fixed-angle rotor (70 Ti type). After centrifugation, the vesicle-containing pellet was discarded, and only the supernatant was collected.

Cells were then maintained in culture at 37°C with 5% CO_2 for 48 hours. Subsequently, the medium was removed and replaced with 40 mL of fresh culture medium. After an additional 24-hour culture period, the SW480-conditioned medium containing sEVs was collected and processed using the following differential centrifugation protocol: (i) 300 × g for 5 minutes at 4°C to remove dead cells and cell debris; (ii) 3,000 × g for 15 minutes at 4°C to eliminate apoptotic bodies; (iii)10,000 × g for 30 minutes at 4°C to remove microvesicles. The resulting supernatant was then concentrated using Amicon Ultra-15 centrifugal filter units with a 100 kDa molecular weight cut-off (Merck Millipore, UFC910008). Specifically, 40 mL of conditioned medium were concentrated by repeated centrifugation at 4°C, 4,000 × g for 40 minutes until reaching a final volume of 500 μL. This concentrate was used for sEVs isolation via SEC. SEC was performed using IZON qEVoriginal/35 nm columns (ICO-35). According to the manufacturer's instructions, the column was equilibrated at room temperature (18–24°C) and activated by adding 17 mL of sterile, filtered PBS (Euroclone). Next, the 500 μL of concentrated conditioned medium were loaded onto the column. Once fully absorbed into the resin, elution was initiated using 8.5 mL of sterile, filtered PBS.

During elution, an initial 2.9 mL exclusion volume (VOID) was collected, followed by sequential collection of 400 μL fractions.

The quality and content of the eluted fractions were assessed using Dynamic Light Scattering (DLS), a technique that measures particle size based on light scattering, allowing estimation of the vesicle size distribution. DLS analysis identified the first three fractions following the VOID as the most enriched in sEVs and free from protein aggregates. These fractions were pooled, and the particle number and concentration were quantified using Nanoparticle Tracking

Analysis (NTA), which tracks individual vesicles via phase contrast microscopy and Brownian motion analysis. The resulting sEVs were stored at –80°C until further use.

6.6 Isolation of sEVs from human plasma

To validate the results obtained with sEVs derived from CRC cells, sEVs were also isolated from plasma of CRC patients and healthy donors. The Total Exosome Isolation Kit (Invitrogen) was used to isolate sEVs from 100 µL of plasma samples, according to the manufacturer's instructions. The plasma was initially centrifuged for 20 min at 2000 x g and for 20 min at 10,000 x g at room temperature. The supernatant was then mixed with 50 µL of 1X PBS and vortexed, and 30 µL of exosome precipitation reagent was added to the samples and vortexed again. The samples were incubated at room temperature for 10 min and centrifuged for 5 min at 10,000 × g at room temperature. Finally, the pellet of sEVs was resuspended in 1X PBS and centrifuged for 30 seconds at 10,000 × g. After isolation, sEVs pellets obtained from plasma samples were resuspended in 50 µl of PBS and quantified by Bradford assay (Pierce, Rockford, IL, USA) [139]. SEVs were stored at -80 °C.

6.7 Treatment of the THLE-2

THLE-2 cells were seeded at a density of 2×10^4 cells/cm² and incubated in a controlled environment at 37°C with 5% CO_2. After reaching subconfluence, the cells were treated with 1.5×10^{10} particles/mL of SW480-sEVs, CRC/P-sEVs or HS-sEVs for 3, 6, 9, 12, and 24 hours according to the different experimental conditions. To verify whether the nuclear accumulation of PD-L1 observed was mediated by the intra-nuclear transport mechanism dependent on the VOR complex, the cells were pretreated for 10 minutes with PRR851 at a concentration of 10 µM.

6.8 sEVs labeling and uptake assay

To visualize cellular internalization of sEVs in THLE-2, SW480-sEVs, CRC/P-sEVs, and HS-sEVs were labeled with PKH26, a lipophilic dye that emits red fluorescence. Briefly, the vesicles were incubated with the dye for 20 min in the dark at room temperature, washed in PBS after three centrifugations at 18,800 x g for 10 min, resuspended in the medium and incubated with the cells for 3, 6 and 8 h at 37 ºC. After incubation, cells were fixed in PAF 4% and stained with ActinGreen™ 488 Ready ProbesR Reagent (Thermo Fisher, Waltham, MA,

USA), which binds F-actin, and Hoechst (Molecular Probes, Life Technologies, USA) to stain nuclei, and observed with confocal microscopy (Nikon A1).

6.9 MTT Cell Viability Assay

The cell viability of THLE-2 upon 24h of treatment with SW480-sEVs was evaluated with MTT (3-[4,5-Dimethylthiazol-2-yl]-2,5 Diphenyl Tetrazolium Bromide) Assay. The THLE-2 cells were seeded in triplicate in 96-well plates; 24h post-seeding, the cells were treated with SW480-sEVs for 24. The absorbance was measured by an ELISA reader at 540 nm (Microplate Reader, BioTek, Winooski, VT, USA).

6.10 Western Blot

For total protein lysate preparation, at the end of the experiment, cells were mechanically detached from the culture flask using a scraper. The resulting cell suspension was washed three times with PBS followed by centrifugation at 300 × g for 5 minutes at 4°. The pellet was then resuspended in lysis buffer composed of: 50 mM Tris-HCl pH 7.6; 300 mM NaCl; 0.5% Triton X-100; PMSF 1X; leupeptin 1X; aprotinin 1X; and phosphatase inhibitors 1X. The suspension was incubated on ice for one hour to promote cell lysis. Finally, the lysate solution was centrifuged at 14,000 rpm for 15 minutes at 4°C to remove cellular debris and nucleic acids. The supernatant containing soluble proteins was collected and quantified using the Bradford assay (Pierce, Rockford, IL, USA).

For nuclear-cytoplasmic fractionation, the Nuclear Extract Kit (#40010 – Active Motif) was used. Following the manufacturer's protocol, at the end of the experiment, cells were washed with PBS phosphatase inhibitor solution (consisting of 10x PBS, H_2O, and phosphatase inhibitor). Cells were then mechanically detached with a scraper and centrifuged at 300 × g for 5 minutes at 4°C. The pellet was resuspended in 1x Hypotonic Buffer and incubated for 15 minutes at room temperature. Subsequently, 10 µL of detergent was added, and the solution was centrifuged at 14,000 × g for 1 minute at 4°C. The recovered supernatant constituted the cytoplasmic protein fraction. The remaining pellet was resuspended in 20 µL of Complete Lysis Buffer (composed of DTT, protease cocktail 100X, Lysis Buffer AAMI) and incubated in agitation for 30 minutes at 4°C. After incubation, centrifugation at 14,000 × g for 10 minutes at 4°C was performed, and the supernatant containing the nuclear protein fraction was collected. Protein content was quantified by Bradford assay (Pierce).

For protein lysates from sEVs isolated by SEC, the first three fractions were pooled and concentrated using an Amicon® Ultra-4 filter with a 100 kDa cutoff, then lysed with Complete Lysis Buffer and quantified by Bradford assay (Pierce).

For Western Blot sample preparation, reducing agent (1x), Sample Buffer (1x), and dH_2O were added to protein lysates; samples were then incubated at 70°C for 10 minutes in a thermoblock to denature proteins. About 10 µg of total protein per sample was loaded onto Bolt™ 4–12% Bis-Tris Plus SDS-PAGE gels (Invitrogen) for separation by molecular weight. A protein marker (Invitrogen, Thermo Fisher Scientific) ranging from 3 to 198 kDa was loaded (7.5 µL). Gels were placed in electrophoresis tanks filled with running buffer prepared by diluting MES SDS Running Buffer 1x in distilled water. Electrophoresis was run at a constant voltage of 165 V for approximately 80 minutes.

After electrophoresis, proteins were transferred from the gel onto a nitrocellulose membrane (MCE, Invitrogen, Life Technologies, USA) using a sandwich system composed of sponge, filter paper (3 mm), gel, membrane, filter paper, and sponge. Transfer was performed at 50 V for 90 minutes at 4°C in Transfer Buffer (1x Tris-glycine, 20% methanol, dH_2O).

To verify transfer efficiency, membranes were stained with Ponceau Red (0.1% in 5% acetic acid), then washed with TBS-Tween (20 mM Tris-HCl, 150 mM NaCl, 0.1% Tween 20 in dH_2O, pH 7.6) to remove the dye.

Membranes were incubated for 1 hour and 30 minutes at 4°C with agitation in Blocking Solution (5% BSA in TBS-Tween). After washing, membranes were incubated overnight at 4°C with primary antibodies. The primary antibodies used were: PD-L1 (Antibodies, A251953, diluted 1:1000 in Blocking Solution), VISTA (Antibodies, AB254581, 1:1000), PD-L2 (Antibodies, AB253570, 1:1000), CD81 (AB219209, 1:300), TSG101 (AB133586, 1:300), Alix (AB186429, 1:300), HSP70 (AB2787, 1:300), Calnexin (AB22595, 1:300), and HA Tag (Invitrogen 26183, 1:500).

After overnight incubation with primary antibodies, membranes were washed five times for 5 minutes each with TBS-Tween, followed by 1 hour incubation at 4°C with agitation with HRP-conjugated secondary antibodies: Anti-Rabbit IgG HRP-linked (Cell Signaling 31460) and Anti-Mouse IgG HRP-linked (Cell Signaling 2-6520), both diluted 1:1000 in Blocking Solution. Membranes were then washed five times for 5 minutes each with TBS-Tween.

The chemiluminescent substrate for HRP was prepared using Amersham ECL Western Blotting Detection Reagent by mixing Detection Reagent 1 and 2 in a 1:1 ratio. Chemiluminescent signals were acquired with the ChemiDoc™ MP imaging system, and densitometric analysis of protein bands was performed using ImageJ software.

6.11 qPCR

To analyze gene expression of PD-L1, PD-L2, and VISTA, Real-Time qPCR was performed. THLE-2 cells were seeded in collagen-coated 12-well plates at 6×10^4 cells/cm². After 24 hours, cells were treated with SW480-sEVs for 1, 3, 6, 12, 24, and 48 hours according to experimental conditions.

At the end of treatments, total RNA was extracted using the Illustra™ mini-RNA Kit (GE Healthcare). RNA was reverse-transcribed into cDNA using a high-capacity reverse transcription kit (Applied Biosystems).

Quantitative PCR was performed using SYBR Green with a total reaction volume of 20 µL containing 2X SYBR Green I Master Mix (Applied Biosystems), 2 µL cDNA, and 300 nM forward and reverse primers (Invitrogen). The primer sequences are reported in the Table 4. The Real-Time PCR protocol consisted of initial denaturation at 95°C for 20 seconds, followed by 40 amplification cycles of 95°C for 3 seconds and 60°C for 30 seconds. GAPDH was used as the endogenous control gene.

Gene expression modulation was analyzed by the ΔΔCt method. For each sample, ΔCt was calculated as the difference between target gene Ct and reference gene (GAPDH) Ct. ΔΔCt was obtained by subtracting the control sample ΔCt from the treated sample ΔCt. Relative gene expression (fold change) was calculated using the formula 2^(-ΔΔCt).

Primers	Forward	Reverse
GAPDH	ATGGGGAAGGTGAAGGTCG	GGGTCATTGATGGCAACAATAT
PD-L1	TCACGGTTCCCAAGGACCTA	AGGTCTTCCTCTCCATGCAC
VISTA	TGTAGACCAGGAGCAGGATG	ATGCACCATCCAACTGTGTG
PD-L2	TGAAAAGTGCAAATGGCAAGC	GTCTTGGGAGCCAGGGTGAC

Table 4 - Primers used in RT-PCR

6.12 Immunofluorescence

To perform immunofluorescence on THLE-2 cells, cells were seeded in collagen-coated 6-well chamber slides. After forming a monolayer, cells were treated with sEVs for 3,6, 9 or 12 h hours according to the experimental conditions. After treatment, cells were washed twice with

PBS and fixed with 4% paraformaldehyde for 15 minutes, then permeabilized with 0.1% Triton X-100 in PBS for 2 minutes. Cells were washed 3 times with PBS and incubated for 30 minutes in 1% Blocking solution at room temperature with agitation. Afterwards cells were washed and incubated for 1 hour at room temperature with the primary antibody diluted 1:100 in 1% Blocking solution in PBS. The primary antibodies used were: PD-L1 (Antibodies, A251953), VISTA (Antibodies, AB254581), and PD-L2 (Antibodies, AB253570).

After primary antibody incubation, excess antibody was removed by three washes in PBS 1x. Cells were incubated for 1 hour at room temperature with DyLight 594-conjugated secondary antibody, diluted 1:300 in 1% Blocking solution in PBS. Excess secondary antibody was removed by three additional washes in PBS 1X. Nuclear staining was performed using Hoechst 33342 (Invitrogen, H3570, diluted 1:1000), and cytoskeleton was labeled with Actin Green 488 (Invitrogen, R37110, 1 drop/mL) by incubation for 30 minutes. After three washes in PBS 1X, cells were stored in 70% glycerol until imaging. Cells were observed using a Nikon Eclipse Ti confocal microscope.

6.13 Statistical Analysis

Statistical analysis was performed using GraphPad Prism 9.5.1 (GraphPad Software, Inc., La Jolla, California). Values in all graphs represent the mean ± standard deviation (SD) of three replicates, unless otherwise indicated.

CHAPTER 7 – *In vitro* tridimensional study

In the light of our previous investigation, revealing for the first time that CRC-sEVs carrying TGFβ1 trigger in human healthy Heps the activation of a TGFβ1/SMAD-dependent EMT [90], we hypothesized a key role of CRC-sEVs-educated Heps in developing in liver a fibrotic microenvironment and in shaping h-PMN. However, the investigation of the potential pro-fibrotic activity of CRC-sEVs-exposed Heps demands a valid and reliable model, which can't be represented by the traditional *in vitro* bi-dimensional (2D) system. In fact, for Heps to grow in 2D *in vitro* condition, a collagen and fibronectin coating is required [90]. This condition can hamper the achievement of our investigation's goals, being collagen and fibronectin well known ECM components, more extensively deposited within a fibrotic microenvironment. Moreover, since fibrosis results from an impaired interactions among the various cytotypes in the liver, a more comprehensive system incorporating different cell types is necessary to better elucidate the crosstalk between them. To overcome these limitations along with others, namely lack of physiological relevance, altered cell morphology, limited cell interactions, and so on, we developed a model of Heps' spheroids (3D_Heps) to unravel the pro-fibrotic role of CRC-sEVs-educated Heps in h-PMN establishment.

7.1 Generation and characterization of 3D_Heps

To generate the 3D_Heps the 96 multiwell plate Ultra Low Attachment (Corning 96-well spheroid microplate, Ultra-Low Attachment surface, 4515) was used to seed the THLE-2 cells (1500 cells/well) following the protocol described in the Chapter 8, paragraph 8.2. Three days after seeding the cells formed an appreciable spheric structure that became compact and with well-defined contours after 5 days (*Figure 28A*), when 3D_Heps could be used for the treatment with the CRC-sEVs. Seven days after plating, the 3D_Heps were collected to carry out their characterization. The scanning electron microscopy (SEM) micrograph in *Figure 28B*, shows the rounded and compact structure with a regular circumference of the spheroids, and the hematoxylin eosin staining of their sections (4 μm) revealed the absence of a necrotic core within the inner layers (*Figure 28C*). In addition, the analyses performed by using the automated platform W8 Physical Cytometer Cell Dynamics showed that the 3D_Heps represent a homogenous population in terms of diameter and mass density, with an average diameter of approximately 164 μm, and an average mass density of 1025 fg/m³ (*Figure 28D*).

Finally, to investigate the Heps' differentiation level within the 3D structure, the expression of functional and phenotypic markers was assessed. As shown in the micrographs in *Figure 28E*, 3D_Heps exhibit the expression of the Hepatocytes Transcriptional Factor 4 (HNF4), a nuclear receptor protein expressed in the liver, acknowledged as central regulator of Heps differentiation and function [140], and of E-Cadherin, a transmembrane protein responsible for cell-cell adhesion and maintenance of normal tissue architecture.

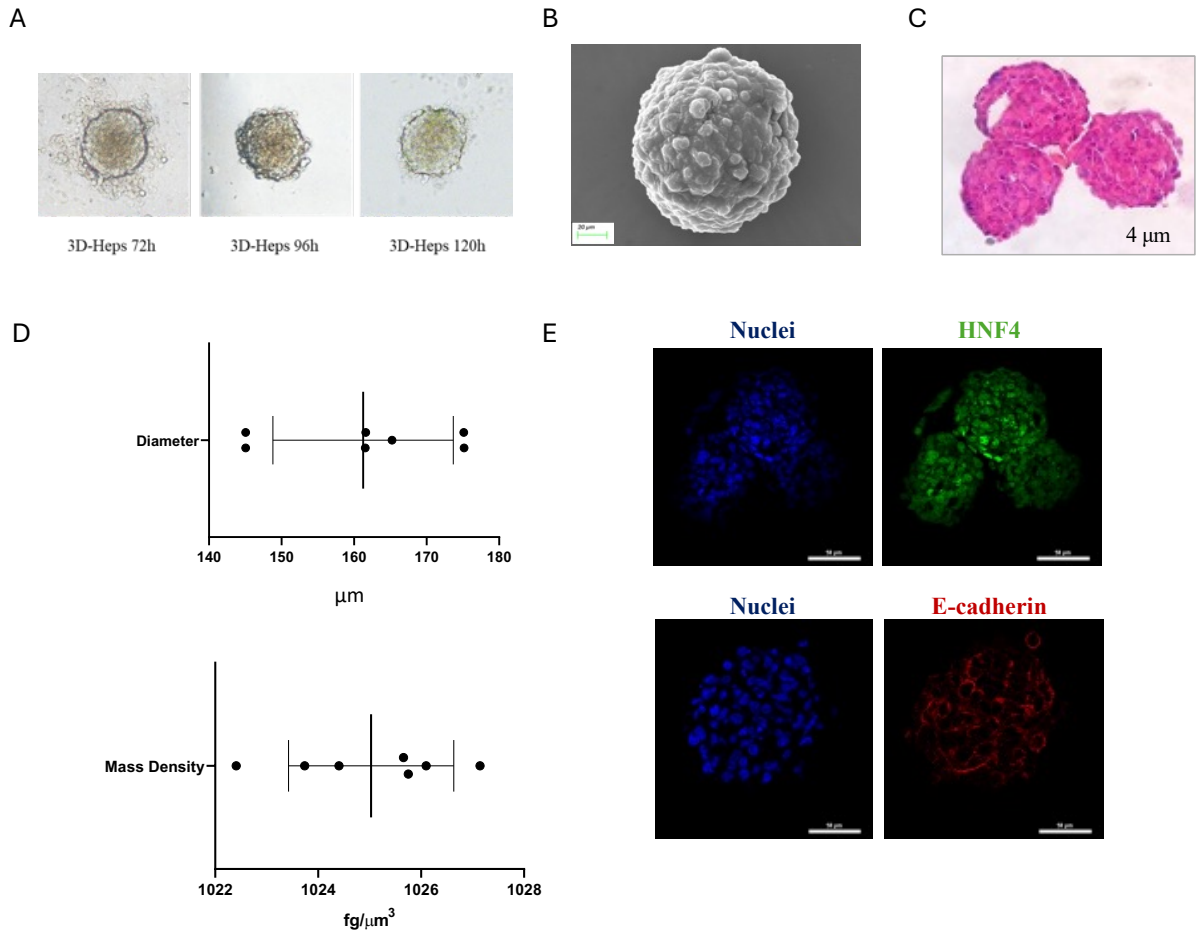

Figure 28 – **A.** Representative image of whole 3D_Heps observed at optical microscope 72, 96, and 120h post seeding; **B**. Representative image of whole 3D_Heps observed at Scansion Electron Microsopy; **C**. Representative image of 4µm sections of 3D_Heps stained with Hematoxylin-Eosin. **D**. Average diameter (left panel) and mass density (right panel) of 3D_Heps, measured through the cytometer W8; **E.** Upper panel: HFN4 expression in 3D_Heps. HNF4 was stained in green; cells nuclei were stained with Hoechst; lower panel**:** E-Cadherin expression in 3D_Heps. E-Cadherin was stained in green; cells nuclei were stained with Hoechst.

7.2 Uptake of SW480-sEVs by 3D_Heps

Before investigating the effects of SW480-sEVs' on 3D_Heps, an uptake assay was performed to assess the internalization of the SW480-sEVs within the 3D structure. Briefly, 3D_Heps were exposed to PKH26-labeled SW480-sEVs (1.5 x10^{10}/mL) for 3 and 8 hours and thereafter imaged at the confocal microscopy. As shown in the micrographs in *Figure 29A*, the internalization of SW480-sEVs, already appreciable after 3 hours of treatment, was evident also in the innermost layers of the 3D structure after 8 hours. Following that, RealTime-Glo™ MT Cell Viability Assay, measuring the reducing potential of cells and thus metabolism, was performed to assess cell viability upon exposure to SW480-sEVs. The results revealed that the treatment with 1.5 x10^{10}/mL of SW480-sEVs for 48 hours did not alter cell viability of 3D_Heps (*Figure 29B*).

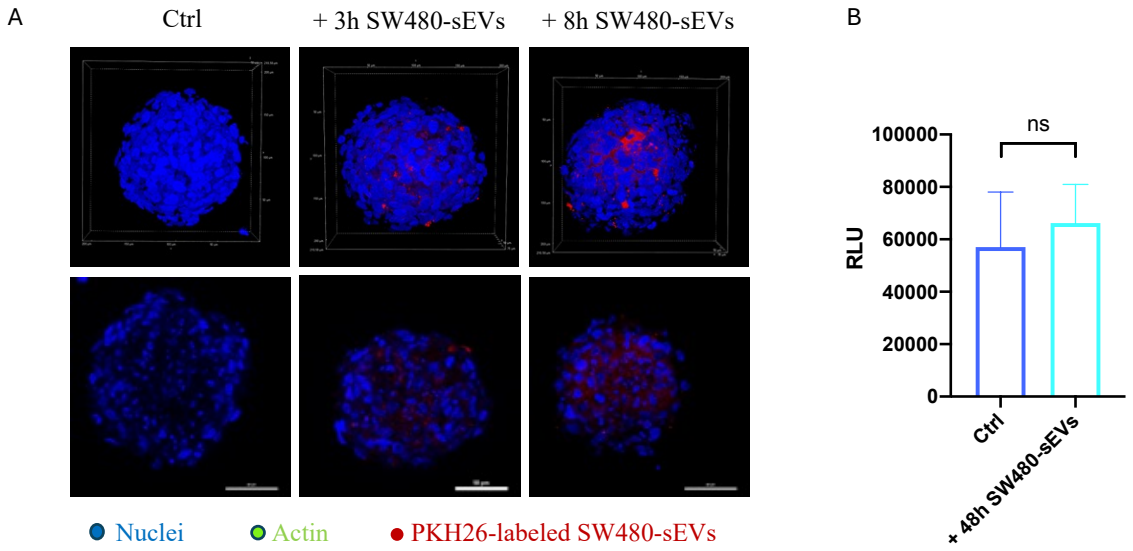

Figure 29 – **A**. Uptake assay of SW480-sEVs by 3D_Heps treated for 3 and 8 hours with 1.5 x10^{10}/mL of SW480-sEVs; actin fibers were stained with ActinGreen (green); nuclear counterstaining was performed using Hoechst (blue); CRC-sEVs were labelled with PKH26 (red). **B**. Cell viability of 3D_Heps exposed to SW480-sEVs for 48h, assessed by RealTime-Glo assay. The histogram shows the relative luminescence units (RLU) measured at different time points (or conditions), indicating the metabolic activity and viability of the cells. Data represent the mean ± standard deviation (SD) of at least three independent experiments. Ctrl untreated control cells. ns = not significant

7.3 SW480-sEVs modulate 3D_Heps properties

To uncover any potential morphological changes following SW480-sEVs exposure, treated and control 3D_Heps were observed at Scansion Electron Microscopy (SEM), revealing that the treatment for 48h with $1.5x10^{10}$/ml SW480-sEVs caused an alteration of their morphology, now elongated and irregular rather than spherical (*Figure 30A*). These observations were confirmed by analyzing the physical parameters diameter and mass density of 3D_Heps following the exposure to the SW480-sEVs through the W8 tool. As shown in *Figure 30B*, both parameters were found significantly decreased by the treatment with the SW480-sEVs in comparison to untreated 3D_Heps. The effects of SW480-sEVs on 3D_Heps' functional properties was then examined by analyzing the expression levels of hepatocyte-specific markers including HNF4 and Albumin. The Western Blot in *Figure 30C* revealed the SW480-sEVs' ability to elicit a downregulation of HNF4 in treated 3D_Heps when compared to control ones. HNF4 downregulation following SW480-sEVs exposure was further confirmed by performing immunofluorescence on whole 3D_Heps treated or not with SW480-sEVs (*Figure 30D*). Afterward, the expression level of Albumin (ALB), a plasma protein primarily produced by Heps, was examined by carrying out ELISA assay on media conditioned by 3D_Heps, which revealed a significant downregulation of ALB after exposure to SW480-sEVs for 24h (*Figure 30E*). Collectively, these findings suggest SW480-sEVs' ability to trigger in 3D_Heps a loss of their morphological, physical, and phenotypic properties, thus directing them towards a less differentiated phenotype.

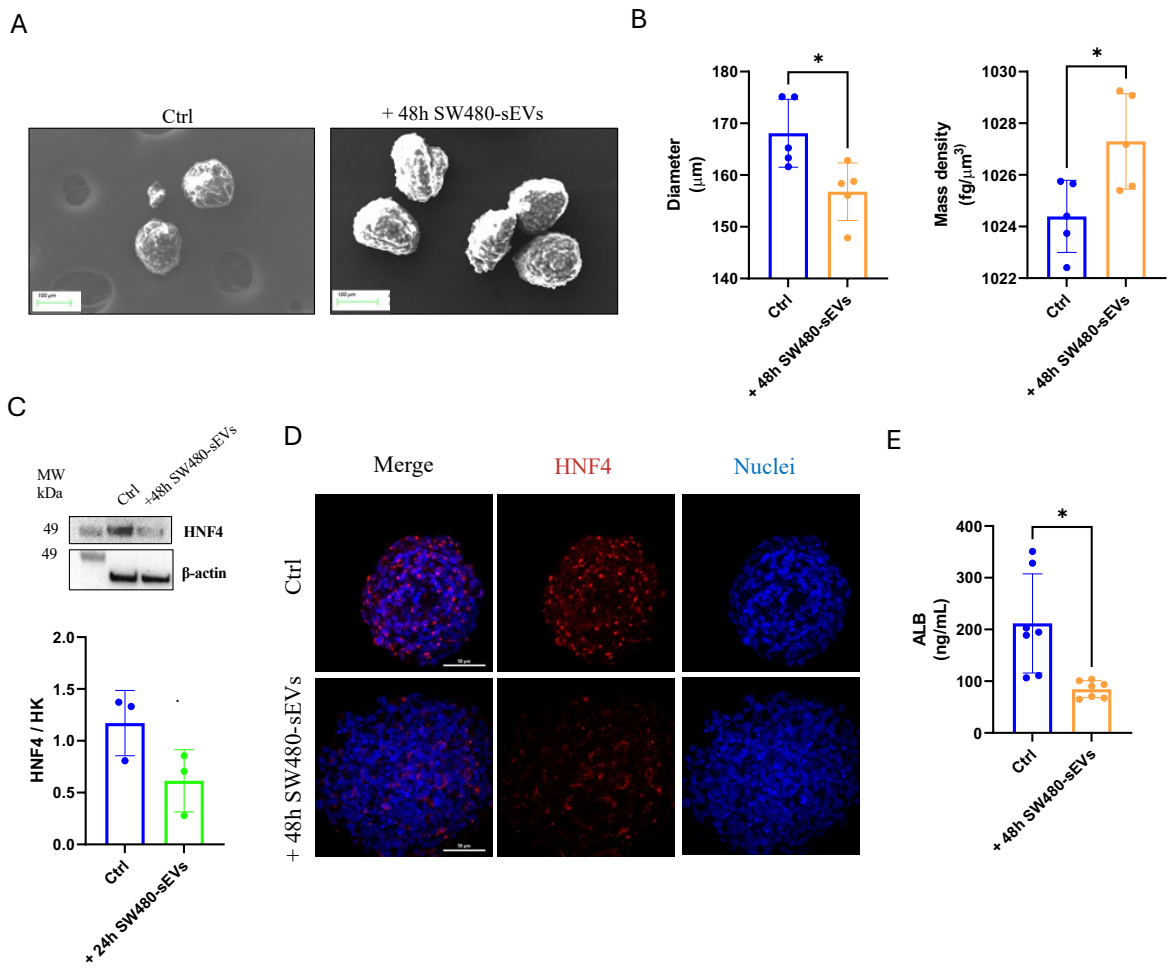

Figure 30 – **A**. SEM analysis of 3D_Heps control and treated with SW480-sEVs for 48h; **B** Histograms showing the average value of diameter (left panel) and mass density (right panel) of at least three different spheroids for each tested condition; **C.** Left panel: Western blot analysis of HNF4 expression in 3D_Heps treated or not with SW480-sEVs for 48h; β-actin was used as housekeeping protein; right panel: corresponding densitometric analysis where the reported values are the mean of at least 2 independent experiments (± SD) of the protein normalized vs loading control. **D**. Fluorescent confocal microscope images showing HNF4 expression and localizations in 3D_Heps control and treated with 48h with SW480-sEVs. HNF4 is stained in red; Hoechst (blue) was used to stain the nuclei; **E.** ELISA assay of albumin (ALB). The histogram represents the ng/mL of ALB released into the culture medium by 3D_Heps treated or not with SW480-sEVs for 48h. Data are expressed as mean ± standard deviation (SD) from at least three independent experiments. Ctrl untreated control cells. * $p < 0.05$.

7.4 SW480-sEVs modulate the expression of EMT markers in 3D_Heps

In consideration of SW480-sEVs ability in modulating the key phenotypic features of 3D_Heps, we aimed to confirm the role of SW480-sEVs in activating EMT in Heps, as demonstrated in our previous study by using conventional 2D hepatocyte system [90]. Thus, we explored whether the expression of epithelial and mesenchymal markers was modulated in 3D_Heps exposed to the treatment with the SW480-sEVs. Both Western Blot analyses and confocal imaging on whole 3D_Heps revealed that the SW480-sEVs treatment reduced the expression of the epithelial markers and enhanced the expression of the mesenchymal markers (*Figure 31*). Specifically, we found that the effect of the treatment with the SW480-sEVs was less evident on the intermediate filaments CK8/18 (epithelial markers; *Figures 31A-B*) and Vimentin (mesenchymal marker; *Figure 31E-F*) and well-marked for the adhesion molecules E-cadherin (epithelial marker; *Figures 31C-D*) and N-cadherin (mesenchymal marker; *Figures 31G-H*).

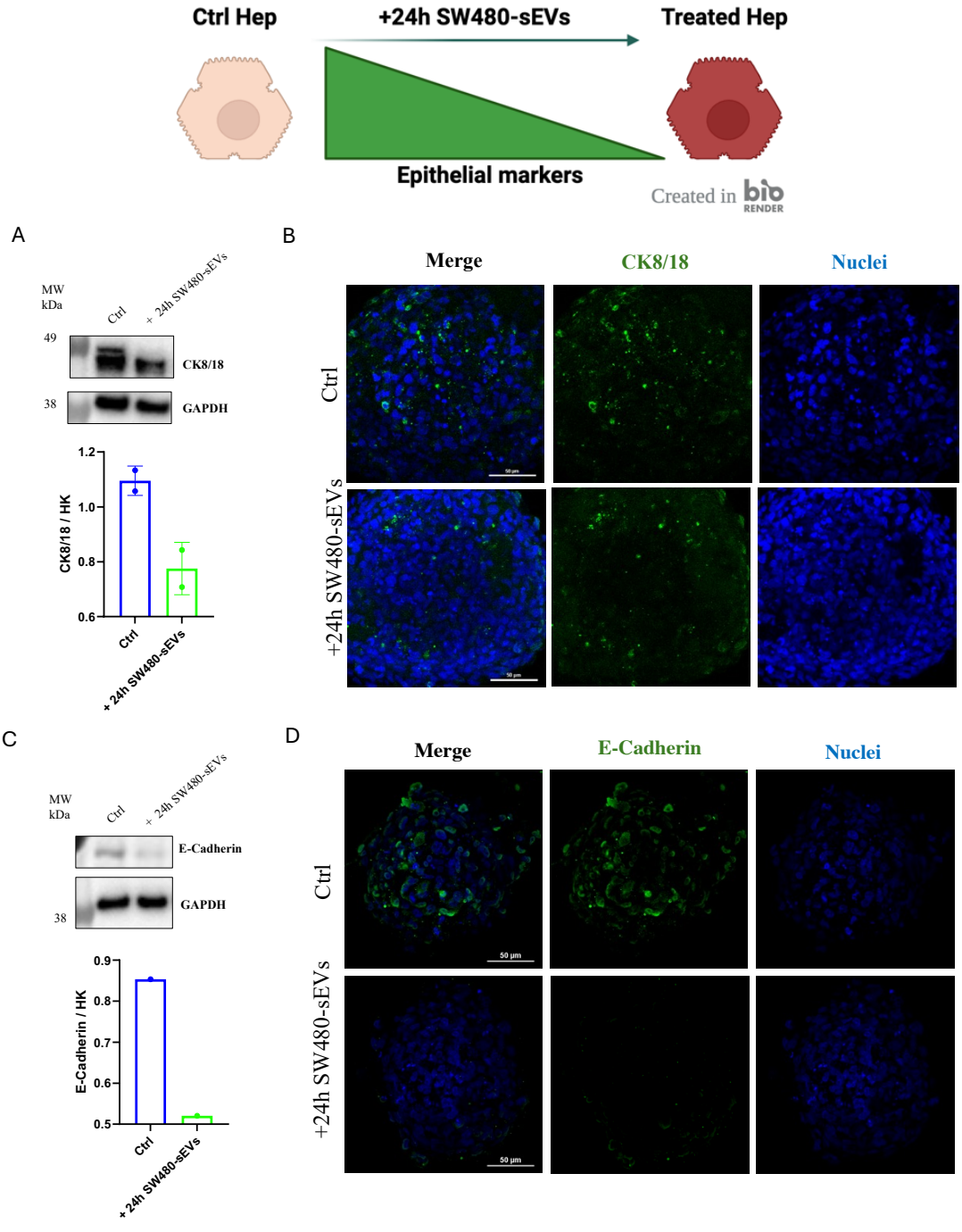
Ctrl Hep
+24h SW480-sEVs
Treated Hep
Epithelial markers
Created in bio RENDER
A
MW kDa
Ctrl
+ 24h SW480-sEVs
49
CK8/18
38
GAPDH
CK8/18 / HK
1.2
1.0
0.8
0.6
Ctrl
+ 24h SW480-sEVs
B
Merge
CK8/18
Nuclei
Ctrl
+24h SW480-sEVs
C
MW kDa
Ctrl
+ 24h SW480-sEVs
E-Cadherin
38
GAPDH
E-Cadherin / HK
0.9
0.8
0.7
0.6
0.5
Ctrl
+ 24h SW480-sEVs
D
Merge
E-Cadherin
Nuclei
Ctrl
+24h SW480-sEVs
50 µm
50 µm

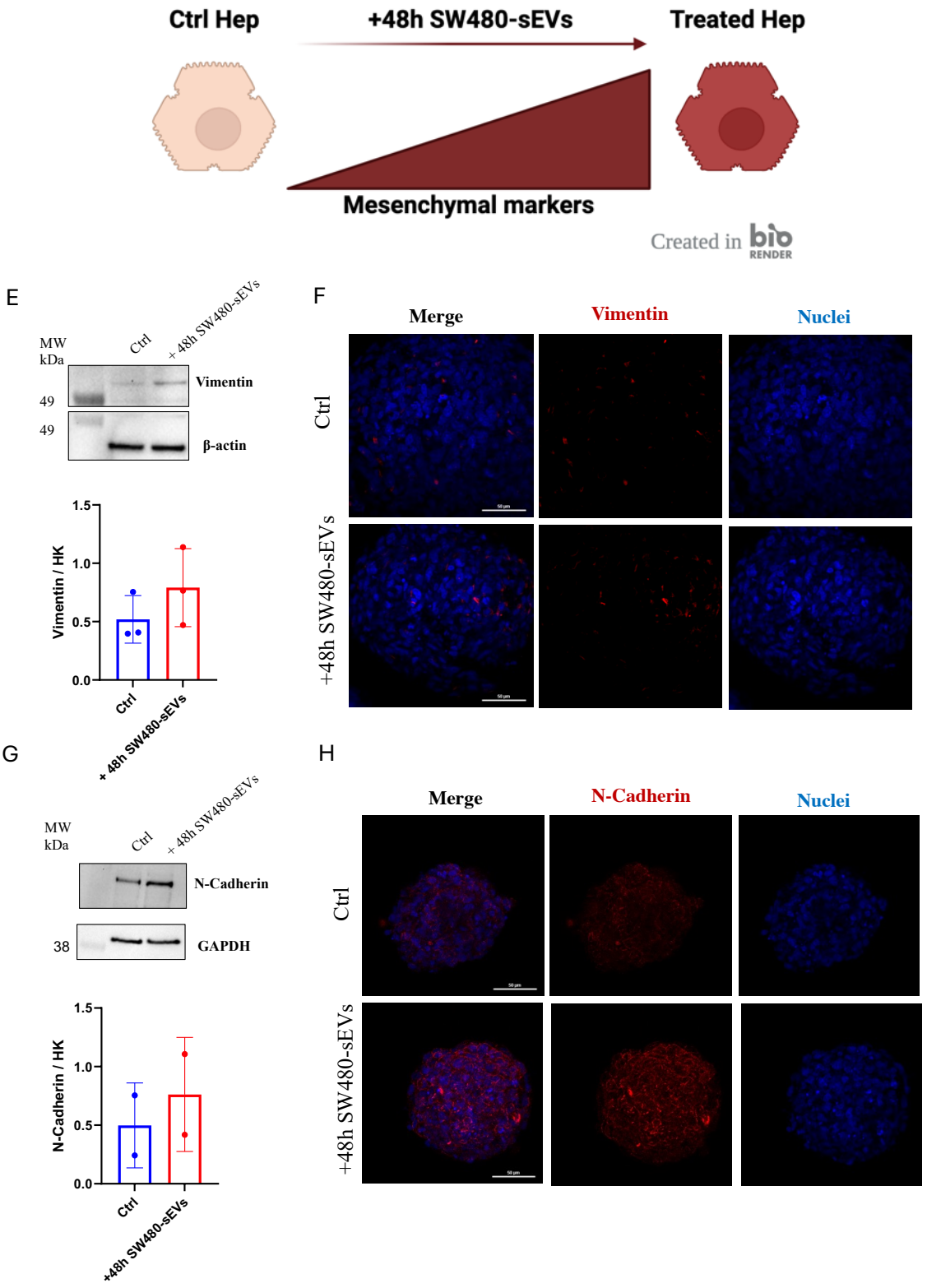

Figure 31 – **A.** Left panel: Western blot analysis of CK8/18 expression in 3D_Heps treated or not with SW480-sEVs for 24h; GAPDH was used as housekeeping protein; right panel: corresponding densitometric analysis where the reported values are the mean of at least 2 independent experiments

(± SD) of the protein normalized vs loading control; **B**. Confocal micrographs showing CK8/18 expression in 3D_Heps treated or not with SW480-sEVs for 24h. CK8/18 is marked in green; nuclei are counterstained in blue. **C**. Left panel: Western Blot analysis of E-cadherin expression in 3D_Heps treated or not with SW480-sEVs for 24h; GAPDH was used as housekeeping protein; right panel: corresponding densitometric analysis where the reported values are the mean of at least 2 independent experiments (± SD) of the protein normalized vs loading control; **D**. Confocal micrographs showing E-cadherin expression in 3D_Heps treated or not with SW480-sEVs for 24h. E-cadherin is marked in green; nuclei are counterstained in blue. **E.** Left panel: Western Blot analysis of Vimentin expression in 3D_Heps treated or not with SW480-sEVs for 48h; β-actin was used as housekeeping protein; right panel: corresponding densitometric analysis where the reported values are the mean of at least 2 independent experiments (± SD) of the protein normalized vs loading control; **F**. Confocal micrographs showing Vimentin expression in 3D_Heps treated or not with SW480-sEVs for 48h. Vimentin is marked in red; nuclei are counterstained in blue. **G.** Left panel: Western Blot analysis of N-cadherin expression in 3D_Heps treated or not with SW480-sEVs for 48h; GAPDH was used as housekeeping protein; right panel: corresponding densitometric analysis where the reported values are the mean of at least 3 independent experiments (± SD) of the protein normalized vs loading control; **H**. Confocal micrographs showing N-cadherin expression in 3D_Heps treated or not with SW480-sEVs for 48h. N-cadherin is marked in red; nuclei are counterstained in blue. *Ctrl*: untreated control cells.

7.5 SW480-sEVs modulate the expression of fibrotic markers and mediators in 3D_Heps

Based on the evidence that SW480-sEVs' can induce EMT in 3D_Heps, we aimed to explore whether SW480-sEVs-educated 3D_Heps can exhibit EMT-dependent pro-fibrotic properties. To achieve this aim, we investigated if in SW480-sEVs treated 3D_Heps occurred changes in deposition of ECM components as Fibronectin, Tenascin C, and Collagen IV, reported to be overexpressed within a fibrotic environment [141] [142]. Results obtained by confocal immunofluorescence microscopy and ELISA assay highlighted an increased deposition of Tenascin C (*Figure 32A*), Fibronectin (*Figure 32B*), and Collagen IV (*Figure 32C*) in 3D_Heps exposed to SW480-sEVs for 48 h in comparison to the untreated ones. Moreover, according to these data we found that the SW480-sEVs stimulate the 3D_Heps to release factors acknowledged as being engaged in liver fibrosis development, namely IL-6 [143] (*Figure 32D*), Gas6 [144] (*Figure 32E*), and TGF-β [145] (*Figure 32F*). Taken together these results suggest that the CRC-sEVs conditioned Heps can have an active role in shaping of a fibrotic microenvironment that may favor the follow tumor cell colonization.

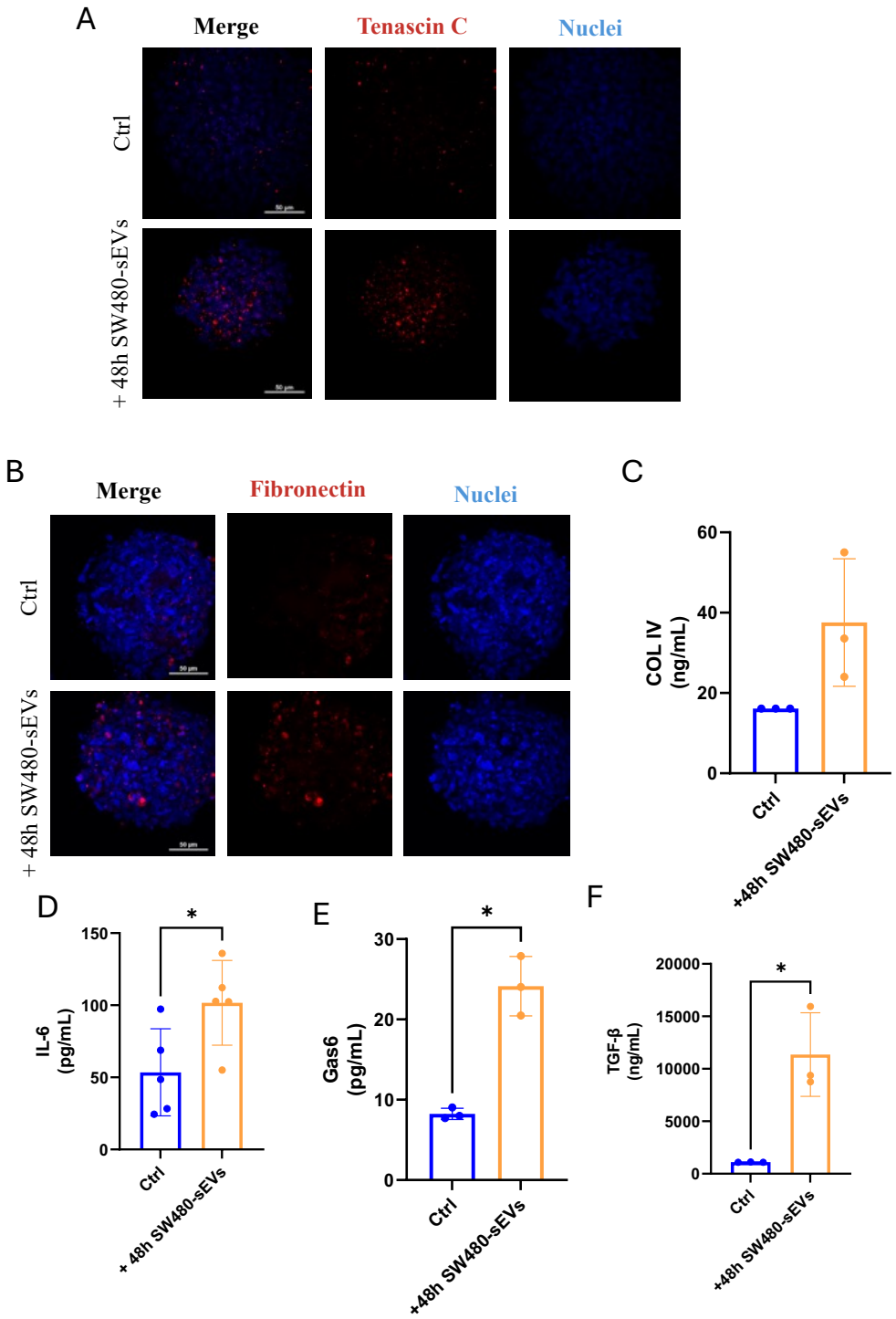

Figure 32 – **A**. Confocal micrographs showing Tenascin C expression in 3D_Heps treated or not with SW480-sEVs for 48h. Tenascin C is marked in red; nuclei are counterstained in blue. **B**. Confocal micrographs showing Fibronectin expression in 3D_Heps treated or not with SW480-sEVs for 48h. Fibronectin is marked in red; nuclei are counterstained in blue. **C.** ELISA assay of COL IV. The histogram represents the ng/mL of COL IV released into the culture medium by 3D_Heps treated or not with SW480-sEVs. Data are expressed as mean ± standard deviation (SD) from at least three independent experiments. **D.** ELISA assay of IL-6. The histogram represents the pg/mL of IL-6

released into the culture medium by 3D_Heps treated or not with SW480-sEVs. Data are expressed as mean ± standard deviation (SD) from at least three independent experiments. **E.** ELISA assay of Gas6. The histogram represents the pg/mL of Gas6 released into the culture medium by 3D_Heps treated or not with SW480-sEVs. Data are expressed as mean ± standard deviation. **F.** ELISA assay of TGF-β. The histogram represents the ng/mL of TGF-β released into the culture medium by 3D_Heps treated or not with SW480-sEVs. Data are expressed as mean ± standard deviation. *Ctrl* untreated control cells, * $p < 0.05$.

7.6 SW480-sEVs favor the invasion of SW620 in 3D_Heps

To specifically point out the role of SW480-sEVs-educated Heps in driving CRC cell colonization, a mixed-cell spheroid model was established. The two isogenic CRC cell lines SW480 (isolated from primary CRC), used as a model of primary CRC, and SW620 (isolated from lymph node metastases), displaying a higher invasive potential, were applied. In particular, SW480 were employed as a source of sEVs, used to precondition 3D_Heps for 48h. Afterwards, SW620-GFP cell line was established to allow the tracking of the cells within the spheroids and were added to 3D_Heps in ratio of 1:3 (SW620-GFP:THLE-2). The obtained mixed-cell spheroids were maintained in culture at least for the next 72h and then recovered. The whole mixed-cell spheroids were observed at confocal microscope to assess the metastatic CRC cells colonization rate. By comparing SW480-sEVs conditioned 3D_Heps with untreated ones, it's clear that SW480-sEVs priming favored the invasion of the SW620-GFP, which penetrated deeper into the core layers of the 3D_Heps (*Figure 33*). This result suggests that the changes observed in 3D_Heps following SW480-sEVs exposure can create a supporting microenvironment for cancer cells invasion, thereby pointing out a novel role of Heps in building a favorable niche for CRC cells colonization in response to CRC-sEVs.

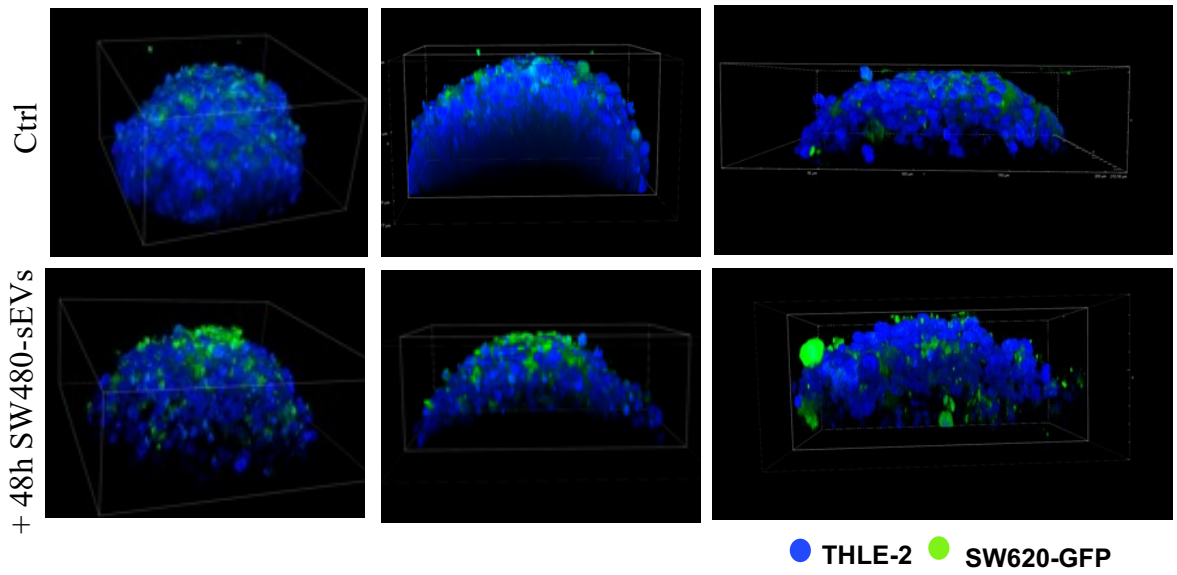

Figure 33 - Confocal micrographs showing 3D_Heps co-cultured for 24h with SW620-GFP, pre-treated or not for 48h with SW480-sEVs. Cells nuclei are stained in blue (Hoechst). SW620 cells are marked in green (GFP). *Ctrl* untreated control cells

7.7 CRC/P-sEVs modulate 3D_Heps functional properties

To corroborate our *in vitro* results achieved via sEVs sourced from SW480 cells, 3D_Heps were treated with sEVs isolated from the plasma of CRC patients (CRC/P-sEVs), previously characterized by TEM, NTA, and protein analysis [90]. After assessing that the treatment with CRC/P-sEVs did not alter the viability 3D_Heps (*Figure 34A*), these sEVs were used to investigate their ability to modulate the key phenotypic features and pro-fibrotic properties of the 3D_Heps. According to the results obtained by using SW480-sEVs, we found that the treatment with 1.5 x10^{10}/mL of CRC/P-sEVs for 48 hours induced a significant reduction of Albumin release (*Figure 34B*) and of HNF4 expression (*Figure 34C*).

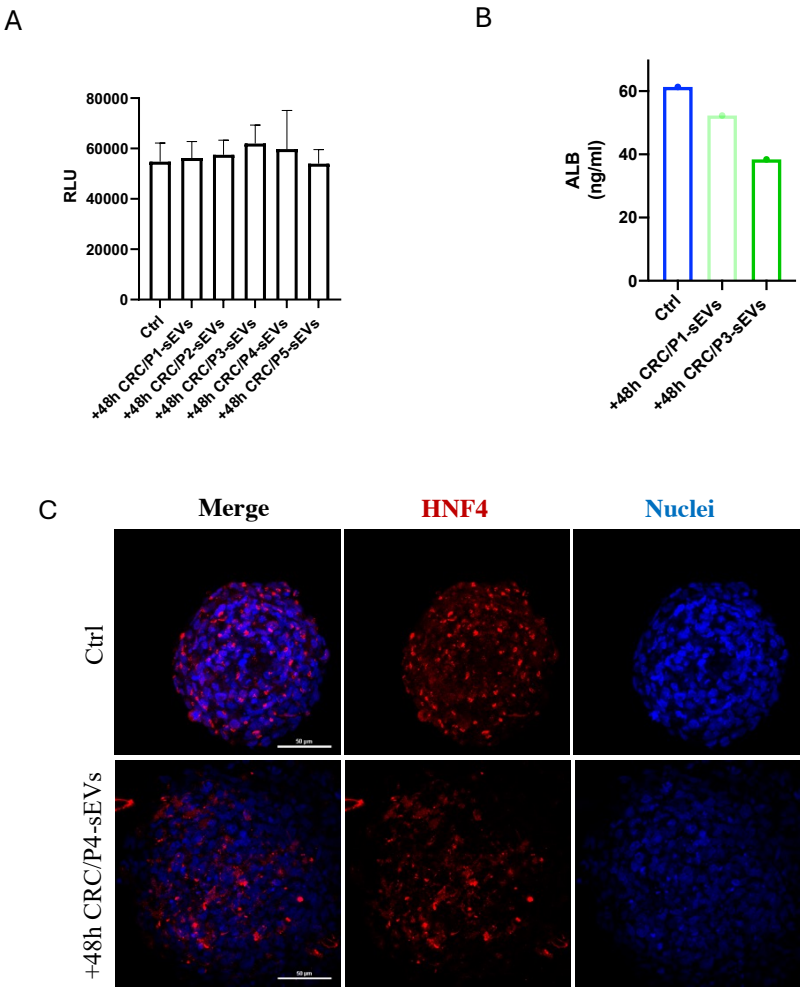

Figure 34 - **A**. Cell viability of 3D_Heps exposed to CRC-sEVs isolated from five different non metastatic CRC patients, assessed by RealTime-Glo assay. The histogram shows the relative luminescence units (RLU) measured at different time points (or conditions), indicating the metabolic activity and viability of the cells. Data represent the mean ± standard deviation (SD) of at least three independent experiments; **B** ELISA assay of albumin (ALB). The histogram represents the ng/mL of ALB released into the culture medium by 3D_Heps control and treated with CRC-sEVs isolated from two different CRC patients. **C**. Confocal micrographs showing HNF4 expression in 3D_Heps treated or not with CRC/P-sEVs for 48h. HNF4 is marked in red; nuclei are counterstained in blue.

In addition to that, we revealed that the exposure to SW480-sEVs determined in 3D_Heps a negative modulation of epithelial markers (CK8/18 and E-Cadherin, *Figures 35 A*-C) and the positive modulation of the mesenchymal ones (Vimentin and N-Cadherin; *Figures 35 D-F*).

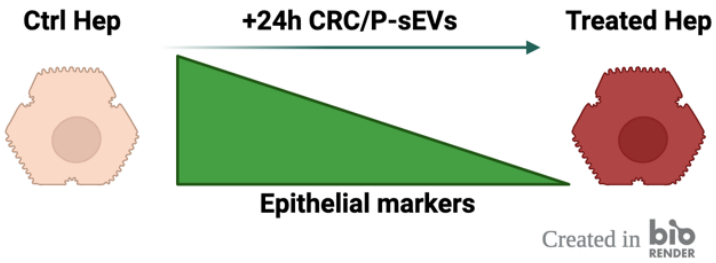
Ctrl Hep
+24h CRC/P-sEVs
Treated Hep
Epithelial markers
Created in bio RENDER

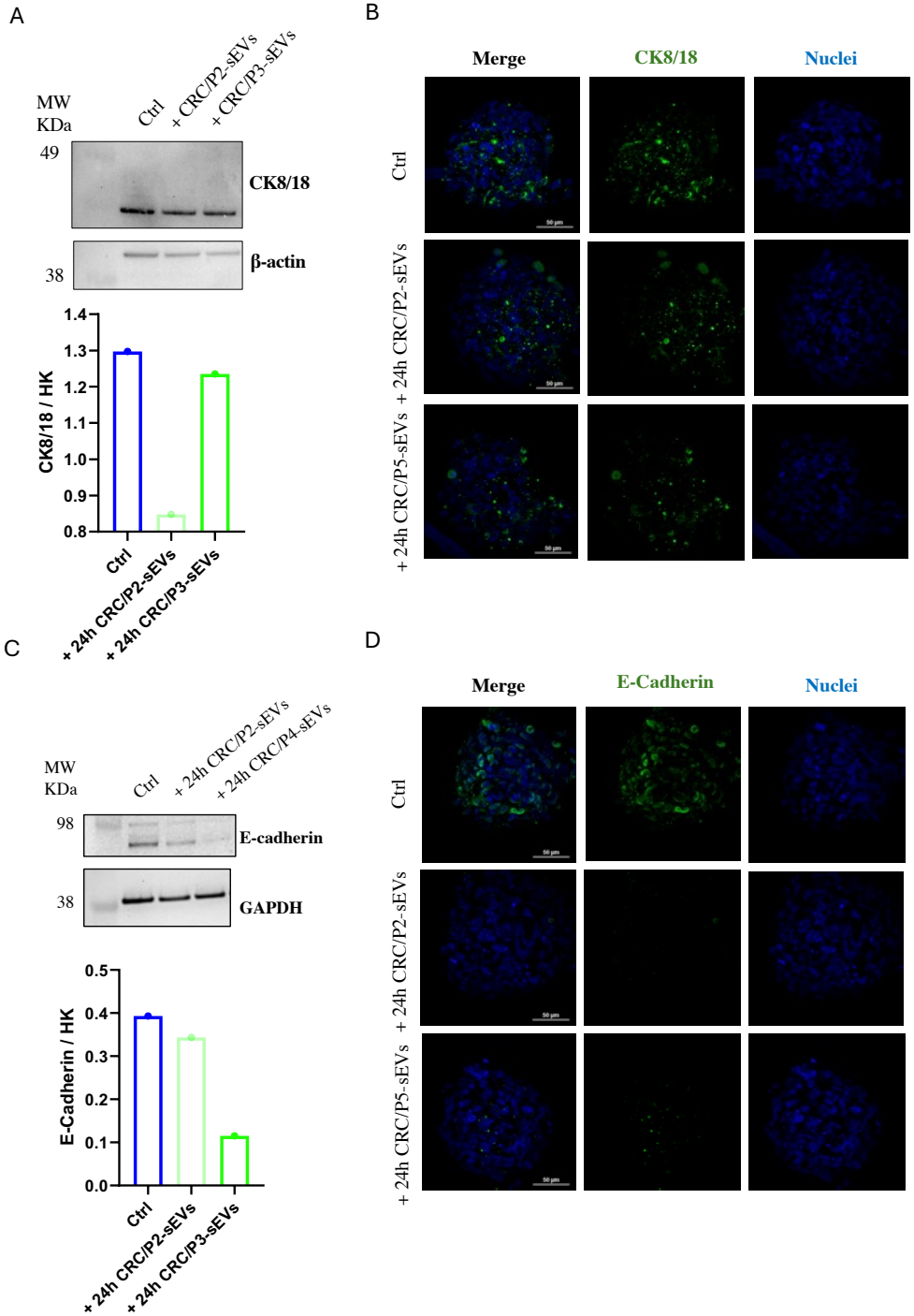
A
MW KDa
Ctrl
+ CRC/P2-sEVs
+ CRC/P3-sEVs
49
CK8/18
38
β-actin
CK8/18 / HK
1.4
1.3
1.2
1.1
1.0
0.9
0.8
Ctrl
+ 24h CRC/P2-sEVs
+ 24h CRC/P3-sEVs
B
Merge
CK8/18
Nuclei
Ctrl
+ 24h CRC/P2-sEVs
+ 24h CRC/P5-sEVs
C
MW KDa
Ctrl
+ 24h CRC/P2-sEVs
+ 24h CRC/P4-sEVs
98
E-cadherin
38
GAPDH
E-Cadherin / HK
0.5
0.4
0.3
0.2
0.1
0.0
Ctrl
+ 24h CRC/P2-sEVs
+ 24h CRC/P3-sEVs
D
Merge
E-Cadherin
Nuclei
Ctrl
+ 24h CRC/P2-sEVs
+ 24h CRC/P5-sEVs

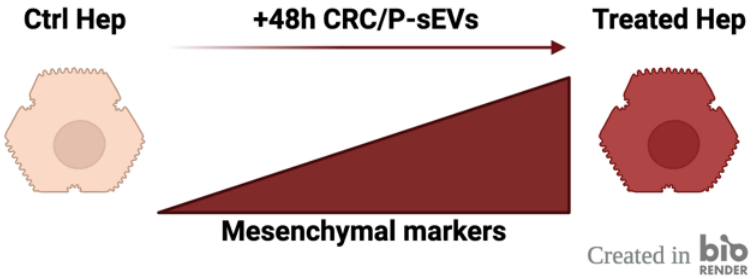
Ctrl Hep
+48h CRC/P-sEVs
Treated Hep
Mesenchymal markers
Created in bio RENDER

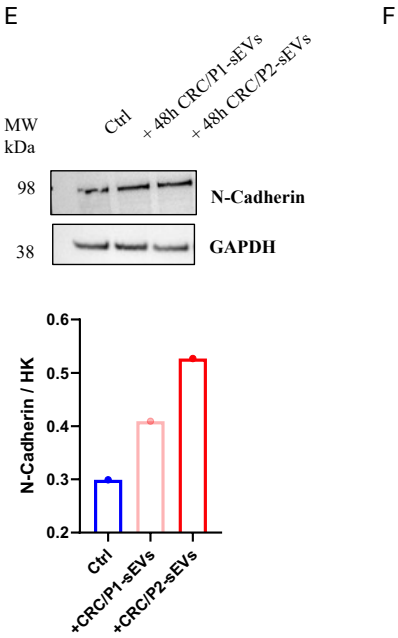
E
MW kDa
Ctrl
+ 48h CRC/P1-sEVs
+ 48h CRC/P2-sEVs
98
N-Cadherin
38
GAPDH
N-Cadherin / HK
0.6
0.5
0.4
0.3
0.2
Ctrl
+CRC/P1-sEVs
+CRC/P2-sEVs

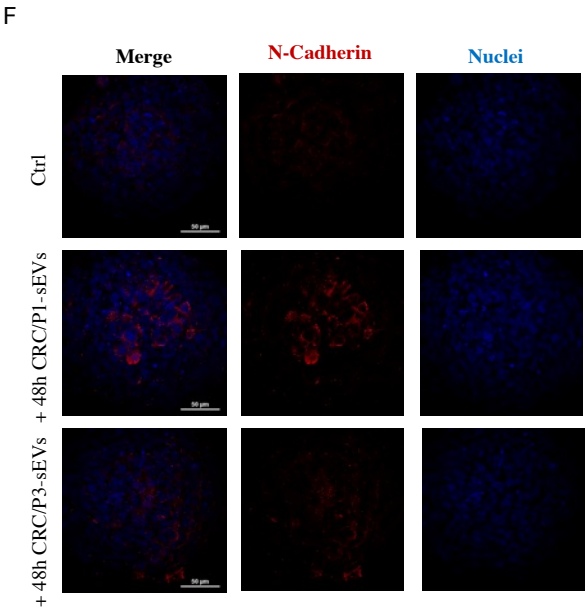
F
Merge
N-Cadherin
Nuclei
Ctrl
+ 48h CRC/P1-sEVs
+ 48h CRC/P3-sEVs

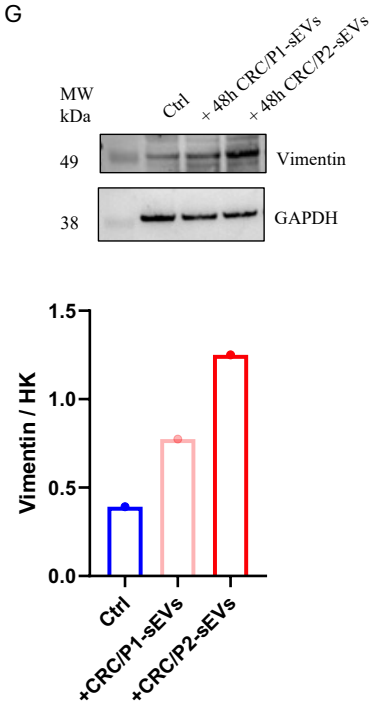
G
MW kDa
Ctrl
+ 48h CRC/P1-sEVs
+ 48h CRC/P2-sEVs
49
Vimentin
38
GAPDH
Vimentin / HK
1.5
1.0
0.5
0.0
Ctrl
+CRC/P1-sEVs
+CRC/P2-sEVs

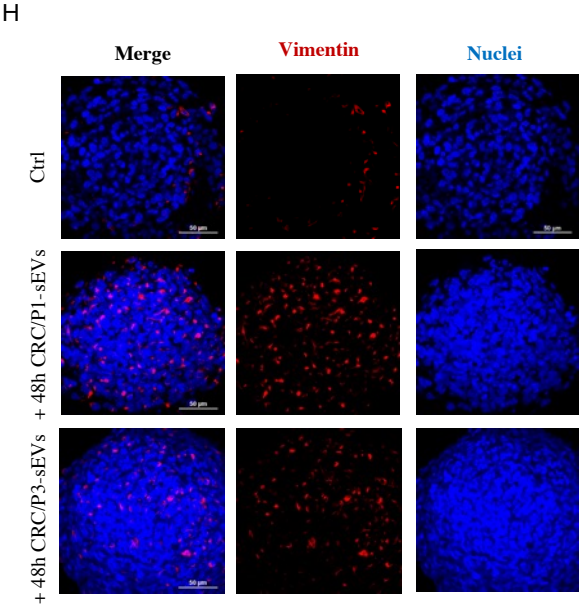
H
Merge
Vimentin
Nuclei
Ctrl
+ 48h CRC/P1-sEVs
+ 48h CRC/P3-sEVs

Figure 35 – **A.** Upper panel: Western blot analysis of CK8/18 expression in 3D_Heps treated or not for 24h with CRC/P-sEVs isolated from two different CRC patients; β-actin was used as housekeeping protein; bottom panel: corresponding densitometric analysis; **B**. Confocal micrographs showing CK8/18 expression in 3D_Heps treated or not for 24h with CRC-sEVs isolated from two different CRC patients. CK8/18 is marked in green; nuclei are counterstained in blue. **C**. Upper panel: Western Blot analysis of E-cadherin expression in 3D_Heps treated or not treated or not for 24h with CRC/P-sEVs isolated from two different CRC patients; GAPDH was used as housekeeping protein; bottom panel: corresponding densitometric analysis; **D**. Confocal micrographs showing E-cadherin expression in 3D_Heps treated treated or not for 24h with CRC/P-sEVs isolated from two different CRC patients. E-cadherin is marked in green; nuclei are counterstained in blue. *Ctrl*: untreated control cells. **E.** Upper panel: Western blot analysis of N-cadherin expression in 3D_Heps treated or not for 48h with CRC/P-sEVs isolated from two different CRC patients; GAPDH was used as housekeeping protein; bottom panel: corresponding densitometric analysis; **F**. Confocal micrographs showing N-cadherin expression in 3D_Heps treated or not for 48h with CRC/P-sEVs isolated from two different CRC patients. N-cadherin is marked in green; nuclei are counterstained in blue. **G**. Upper panel: Western Blot analysis of Vimentin expression in 3D_Heps treated or not treated or not for 48h with CRC/P-sEVs isolated from two different CRC patients; GAPDH was used as housekeeping protein; bottom panel: corresponding densitometric analysis; **H**. Confocal micrographs showing Vimentin expression in 3D_Heps treated treated or not for 24h with CRC-sEVs isolated from two different CRC patients. Vimentin is marked in green; nuclei are counterstained in blue. *Ctrl*: untreated control cells.

Moreover, the CRC/P-sEVs were found able to stimulate in 3D_Heps the deposition of the ECM proteins Tenascin C (*Figure 36A*), Fibronectin (*Figure 36B*), and Collagen IV (*Figure 36C*) and to positively modulate the release of the fibrosis inducers Gas6 (*Figure 36D)*, IL-6 *(Figure 36E)*, and TGF-β (*Figure 36F).* This *ex vivo* validation strengthens the robustness and translational clinical relevance of our findings, highlighting the potent ability of CRC-sEVs to induce profibrotic activation in Heps.

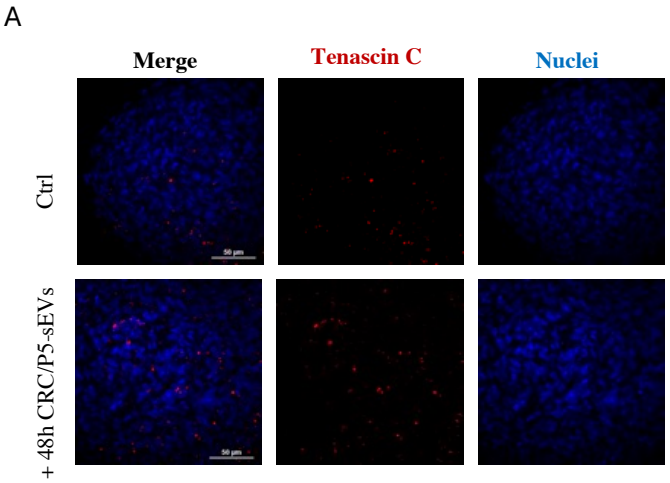
A
Merge
Tenascin C
Nuclei
Ctrl
+ 48h CRC/P5-sEVs

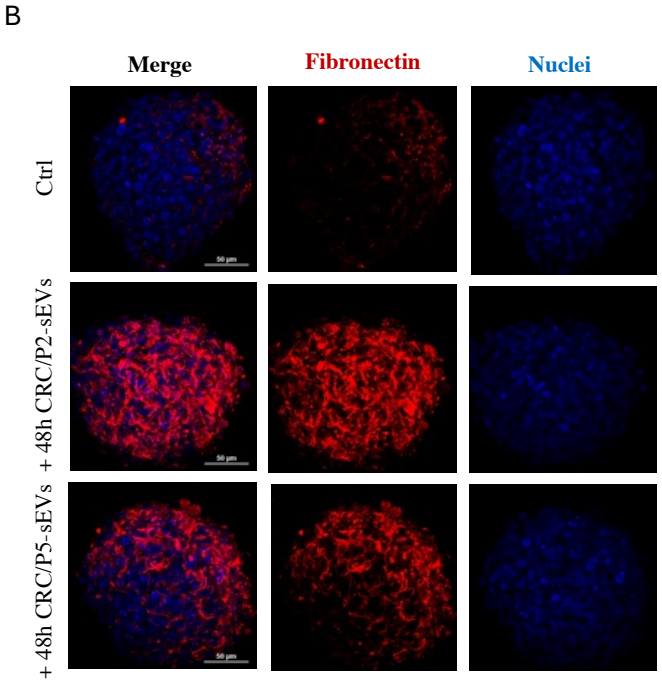
B
Merge
Fibronectin
Nuclei
Ctrl
+ 48h CRC/P2-sEVs
+ 48h CRC/P5-sEVs

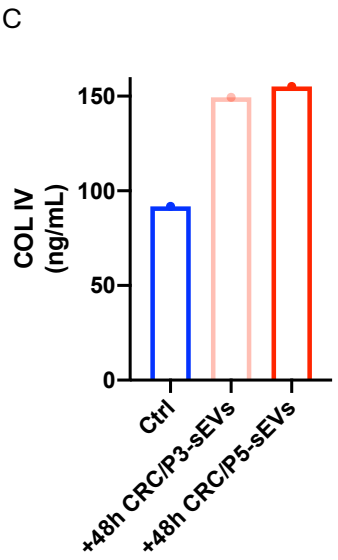
C
COL IV (ng/mL)
150
100
50
0
Ctrl
+48h CRC/P3-sEVs
+48h CRC/P5-sEVs

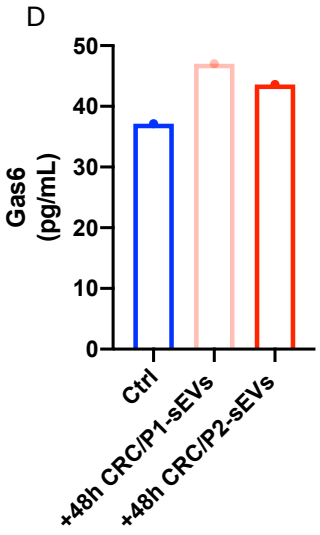
D
Gas6 (pg/mL)
50
40
30
20
10
0
Ctrl
+48h CRC/P1-sEVs
+48h CRC/P2-sEVs

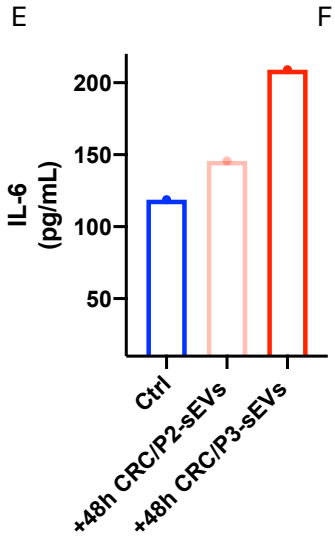
E
IL-6 (pg/mL)
200
150
100
50
Ctrl
+48h CRC/P2-sEVs
+48h CRC/P3-sEVs

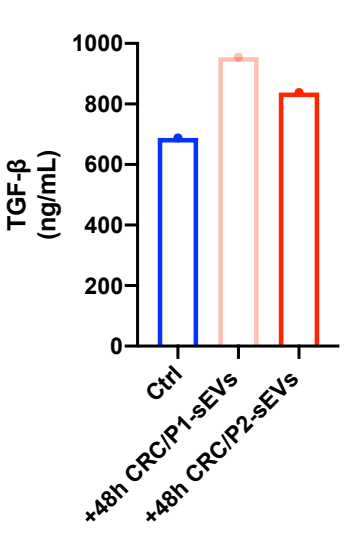
F
TGF-β (ng/mL)
1000
800
600
400
200
0
Ctrl
+48h CRC/P1-sEVs
+48h CRC/P2-sEVs

Figure 36 - A. Confocal micrographs showing Tenascin C expression in 3D_Heps treated or not with CRC/P-sEVs for 48h. Tenascin C is marked in red; nuclei are counterstained in blue. **B**. Confocal micrographs showing Fibronectin expression in 3D_Heps treated or not fot for 48h with CRC/P-sEVs isolated from two different CRC patients. Fibronectin is marked in red; nuclei are counterstained in blue. **C.** ELISA assay of COL IV. The histogram represents the ng/mL of COL IV released into the culture medium by 3D_Heps treated or not fot for 48h with CRC/P-sEVs isolated from two different CRC patients. **D.** ELISA assay of Gas6. The histogram represents the pg/mL of Gas6 released into the culture medium by 3D_Heps treated or not fot for 48h with CRC-sEVs isolated from two different CRC patients. **E.** ELISA assay of IL-6. The histogram represents the pg/mL of IL-6 released into the culture medium by 3D_Heps treated or not fot for 48h with CRC/P-sEVs isolated from two different CRC patients. **F.** ELISA assay of TGF-β. The histogram represents the ng/mL of TGF-β released into the culture medium by 3D_Heps treated or not fot for 48h with CRC/P-sEVs isolated from two different CRC patients.

To confirm that the observed effects were specifically attributable to tumor-derived sEVs, sEVs were isolated from the plasma of healthy donors (HS-sEVs), as previously described [90] and used to treat 3D_Heps. After confirming that the selected dose was non-toxic to cells (*Figure 37A*), the effects of HS-sEVs on 3D_Heps were evaluated.

In contrast to the effects observed in 3D_Heps exposed to CRC-sEVs, treatment with HS-sEVs did not induce a loss of key functional or phenotypic hepatocyte markers. Specifically, the expression of HNF4 (*Figure 37B*) and Albumin (*Figure 37C*) was preserved, with only a slight, non–statistically significant decrease in Albumin levels. Likewise, HS-sEV exposure did not alter the expression of the cytoskeletal proteins CK8/18 (*Figure 37D)* and Vimentin (*Figure 37E*).Furthermore, HS-sEVs did not modulate the expression of fibrotic markers, including Fibronectin (*Figure 37F*) and Collagen IV (*Figure 37G*), nor of key fibrosis-associated mediators such as IL-6 (*Figure 37H*), Gas6 (*Figure 37I*), and TGF-β (*Figure 37L*). Although a slight reduction in some of these mediators was observed, these changes were not statistically significant. This lack of effect demonstrates that the profibrotic reprogramming observed is not a generic response to circulating sEVs, but rather a specific consequence of tumor-derived sEVs, thereby reinforcing the specificity and biological relevance of our findings.

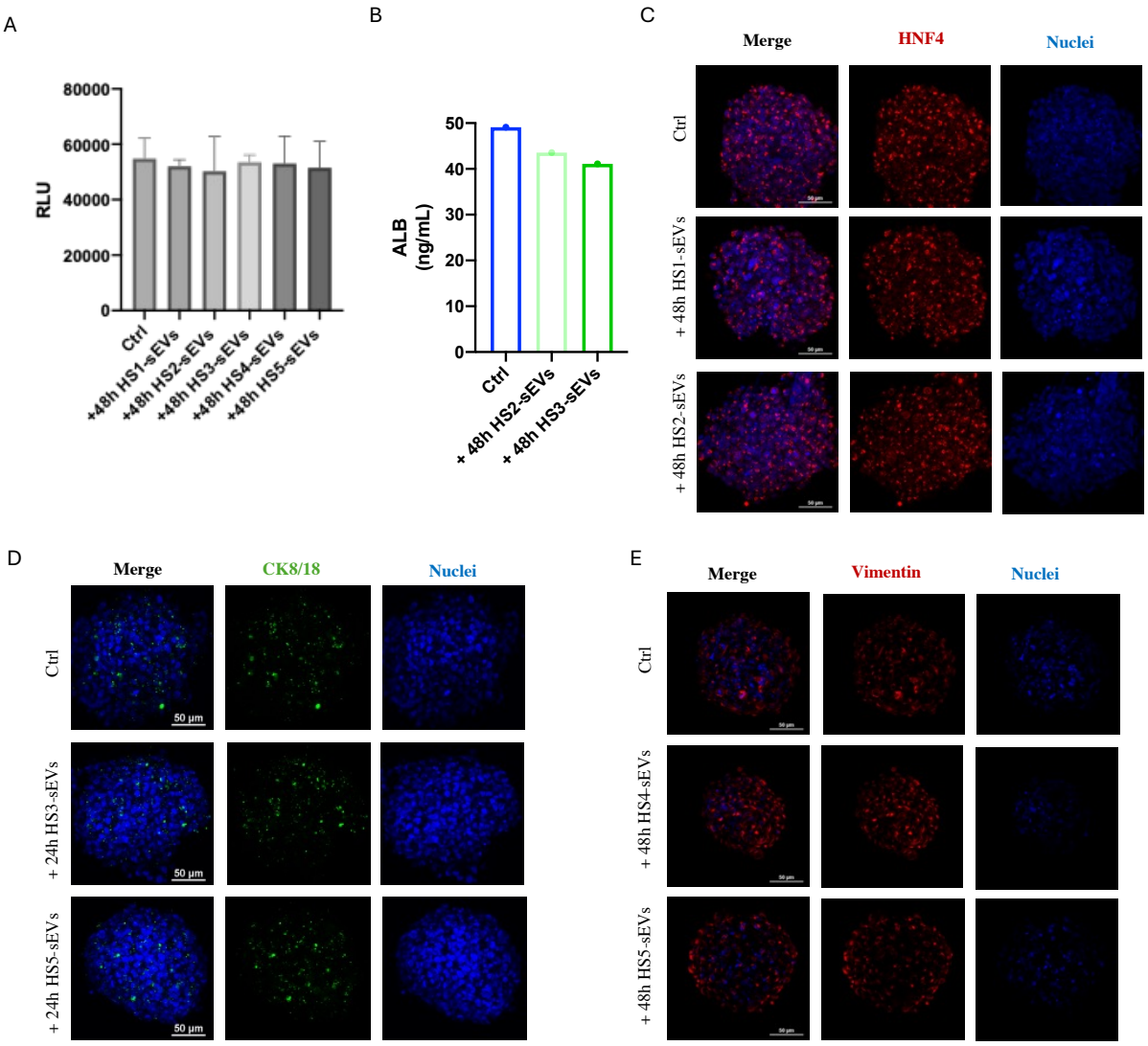
A
RLU
80000
60000
40000
20000
0
Ctrl
+48h HS1-sEVs
+48h HS2-sEVs
+48h HS3-sEVs
+48h HS4-sEVs
+48h HS5-sEVs
B
ALB (ng/mL)
50
40
30
20
10
0
Ctrl
+ 48h HS2-sEVs
+ 48h HS3-sEVs
C
Merge
HNF4
Nuclei
Ctrl
+ 48h HS1-sEVs
+ 48h HS2-sEVs
D
Merge
CK8/18
Nuclei
Ctrl
+ 24h HS3-sEVs
+ 24h HS5-sEVs
50 µm
E
Merge
Vimentin
Nuclei
Ctrl
+ 48h HS4-sEVs
+ 48h HS5-sEVs

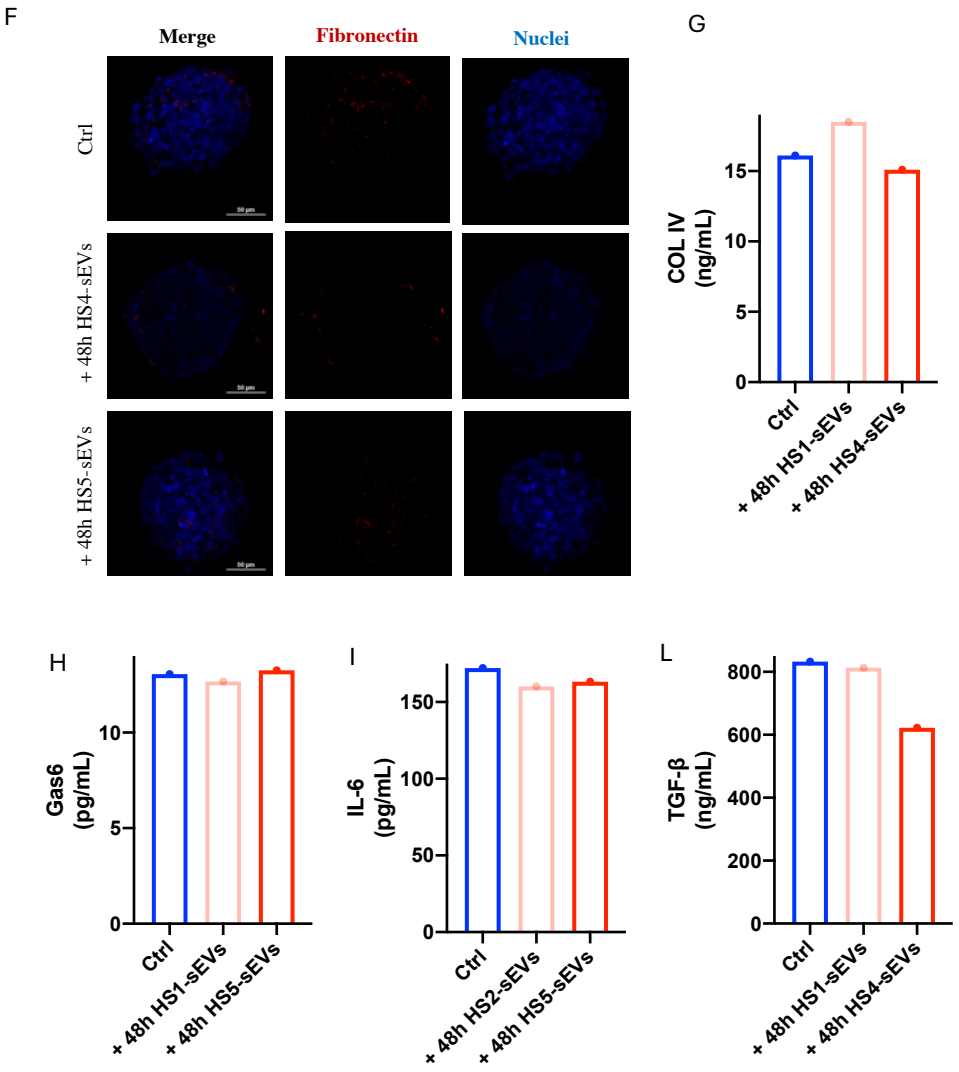

Figure 37 – **A**. Cell viability of 3D_Heps exposed to HS-sEVs isolated from five different healthy donors, assessed by RealTime-Glo assay. The histogram shows the relative luminescence units (RLU) measured at different time points (or conditions), indicating the metabolic activity and viability of the cells. Data represent the mean ± standard deviation (SD) of at least three independent experiments; **B**. ELISA assay of ALB. The histogram represents the ng/mL of ALB released into the culture medium by 3D_Heps treated or not for 48h with HS-sEVs isolated from two healthy subjects; **C**. Confocal micrographs showing HNF4 expression in 3D_Heps treated or not for 48h with HS-sEVs isolated from two healthy subjects. HNF4 is marked in red; nuclei are counterstained in blue; **D**. Confocal micrographs showing CK8/18 expression in 3D_Heps treated or not for 24h with HS-sEVs isolated from two healthy subjects. CK8/18 is marked in green; nuclei are counterstained in blue; **E**. Confocal micrographs showing Vimentin expression in 3D_Heps treated or not for 48h with HS-sEVs isolated from two healthy subjects. Vimentin is marked in red; nuclei are counterstained in blue; **F**. Confocal micrographs showing Fibronectin expression in 3D_Heps treated or not for 48h with HS-sEVs isolated from two healthy subjects. Fibronectin is marked in red; nuclei are counterstained in blue. **G.** ELISA

assay of COL IV. The histogram represents the ng/mL of COL IV released into the culture medium by 3D_Heps treated or not fot for 48h with HS-sEVs isolated from two different healthy donors. **H.** ELISA assay of Gas6. The histogram represents the pg/mL of Gas6 released into the culture medium by 3D_Heps treated or not fot for 48h with HS-sEVs isolated from two different healthy. **I.** ELISA assay of IL-6. The histogram represents the pg/mL of IL-6 released into the culture medium by 3D_Heps treated or not for 48h with HS-sEVs isolated from two different healthy donors. **L.** ELISA assay of TGF-β. The histogram represents the ng/mL of TGF-β released into the culture medium by 3D_Heps treated or not fot for 48h with HS-sEVs isolated from two different healthy donors. *Ctrl* untreated control cells.

7.8 Future outlooks: generation of heterotypic spheroids including HSCs and Heps

To develop a more comprehensive *in vitro* model that closely mimics the complex hepatic microenvironment and allows the study of the profibrotic properties of CRC-sEVs-educated Heps, heterotypic spheroids comprising different hepatic cell populations were generated. Given the well-established role of hepatic stellate cells in liver fibrosis, as extensively documented in the literature [27], and the emerging evidence from our group highlighting the key contribution of Heps in these fibrotic processes, we developed heterotypic spheroids (3D_Hep/Ste) composed of THLE-2 hepatocytes and LX-2 hepatic stellate cells.

To identify the optimal hepatocyte-to-stellate cell ratio for spheroid formation, various THLE-2:LX-2 ratios were tested, including 1:2, 1:4, 1:6, 1:8, 1:10, and 1:12. Cell viability within these spheroids was assessed using the RealTime-Glo® viability assay, which indicated that the 1:8 and 1:12 ratios yielded the highest viability (*Figure 38A*). To further validate these findings, the LIVE/DEAD™ viability assay was performed, and spheroids were analyzed via confocal microscopy. As shown in *Figure 38B*, the 1:12 ratio demonstrated superior cell viability and was therefore selected as the optimal condition for generating 3D_Hep/Ste spheroids. Once the optimal ratio between Heps and HSCs was established, we aimed to determine the specific spatial localization of each cell type within the heterotypic spheroids. To this end, genetically modified THLE-2 cells expressing Green Fluorescent Protein (THLE-2 GFP) and LX-2 cells expressing Red Fluorescent Protein (LX-2 RFP) were generated and used to develop fluorescently labeled heterotypic spheroids. Confocal microscopy analysis of the 3D_Hep/Ste spheroids (*Figure 38C*) revealed the presence of LX-2 cells embedded within the THLE-2 population, forming distinct niches where stellate cells appeared to cluster. This

polarized distribution of cells within the spheroid suggests a degree of spatial organization, which will be further investigated in future studies.

Given the extensive scientific evidence supporting the ability of hepatic stellate cells to promote Heps differentiation in co-culture, we next aim to assess whether Heps within the heterotypic spheroids exhibit enhanced differentiation. This will be evaluated through the analysis of Heps phenotypic and functional markers, including HNF4 and albumin expression. Furthermore, we intend to employ this novel 3D co-culture system to study the cellular response to CRC-sEVs. Specifically, we will investigate (i) whether exposure to CRC-sEVs alters the spatial organization of the two cell populations within the spheroids, and (ii) whether it modulates EMT markers, fibrotic mediators, and ECM protein deposition. These analyses will help determine whether the interaction between Heps and HSCs amplifies the pro-fibrotic effects that CRC-sEVs exert on each cell type individually.

Overall, the optimized heterotypic spheroids represent an advanced *in vitro* model to study hepatocyte–stellate cell crosstalk and to explore their combined contribution to liver fibrosis within the hepatic microenvironment.

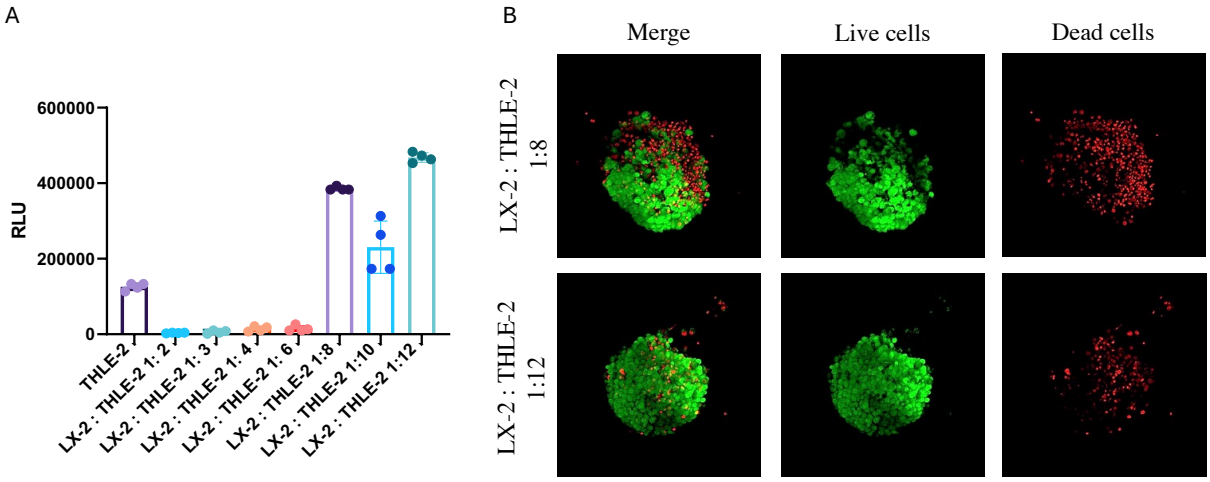

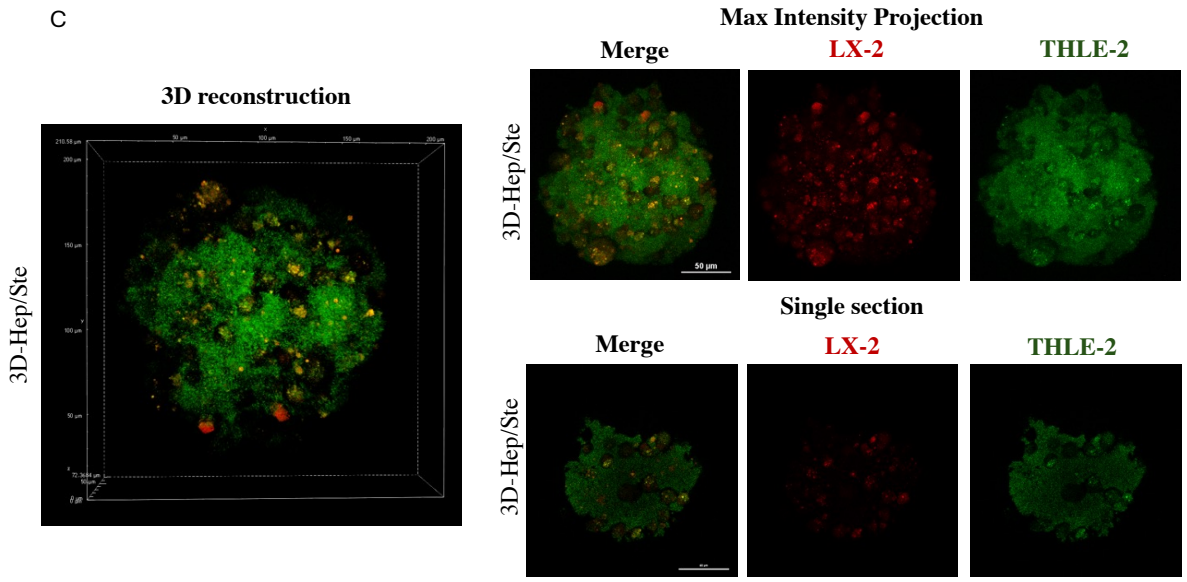

Figure 38 – **A**. Cell viability analysis using the RealTime-Glo® assay. The following LX-2 : THLE-2 cell ratios were tested: 1:2, 1:4, 1:6, 1:8, 1:10, and 1:12. Data represent mean ± standard deviation from four independent replicates. Homotypic THLE-2 spheroids were used as a viability reference **B**. Confocal microscopy images of the LIVE/DEAD™ viability assay performed on heterotypic spheroids with Heps:HSCs cell ratio 1:8 and 1:12. Images, acquired at 60X magnification, show live cells (green – Calcein-AM) and dead cells (red – Propidium Iodide). **C**. Confocal microscopy images of 3D_Hep/Ste (12:1 ratio). THLE-2 cells are labeled in green; LX-2 cells are labeled in red.

CHAPTER 8 – Material and Methods: *In vitro* tridimensional study

8.1 Cell colture mantainance

THLE-2 (ATCC, Manassas, VA), healthy human epithelial cells isolated from the left lobe of liver and immortalized with the catalytic subunit of human telomerase (hTERT), were cultured in RPMI 1640 medium (Euroclone,UK) supplemented with 10% fetal bovine serum (FBS, Euroclone UK), 1% penicillin (100 U/mL) and streptomycin (100µg/mL), epidermal growth factor (EGF) 5 ng/mL and phosphoethanolamine (PEA) 70 ng/mL at 37 ºC with 5% CO_2. Cells were maintained in flasks with a coating obtained from a solution of 0.03 mg/mL bovine collagen type I (Advanced Biomatrix, San Diego region, California, USA), and 0.01 mg/mL bovine albumin (SigmaAldrich, St Louis, MO, USA).

The isogenic CRC cell lines SW480 (ATCC CCL-228) and SW620 (ATCC CCL-227) derived respectively from a pre-metastatic primary tumor and lymph node metastasis, were used in this study. SW480 and SW620 cells were maintained in RPMI 1640 medium (Euroclone, UK) supplemented with 10% fetal bovine serum (FBS; Euroclone, UK), 2 mM L-glutamine (Euroclone, UK), 100 U/mL penicillin and 100 µg/mL streptomycin (Euroclone, UK). Before use, FBS (EU-approved South American origin, Euroclone, UK) was ultracentrifuged for 105 min at 100,000 ×g in type 70 Ti fixed-angle rotor. Fetal bovine serum is ultracentrifuged because it contains extracellular vesicles of animal origin that could contaminate the sample of interest [138].

8.2 3D_Heps development

To obtain the 3D_Heps, THLE-2 cells were seeded (1,500 cells x well) into a Ultra-Low Attachment 96-well multiwell (Corning 96-well Spheroid Microplate, Ultra-Low Attachment Surface), in 100 µL of RPMI 1640 medium (Euroclone, UK), supplemented with 10% fetal bovine serum (FBS, Euroclone UK), 1% penicillin (100 U/mL) and streptomycin (100µg/mL), 0.3 mL of epidermal growth factor (EGF) (5 ng/mL) and 0.4 mL of phosphoethanolamine (PEA) (70 ng/mL). After 3 days, 100 µL of Airway Epithelial Cell Basal Medium (ATCC, Manassas, VA) supplemented with 2X Bronchial Epithelial Cell Growth Kit (ATCC, Manassas, VA), 70 ng/mL phosphoethanolamine, 5 ng/mL epidermal growth factor (EGF), 100 U/mL penicillin and 100 µg/mL streptomycin (Euroclone, UK) without FBS were added to each well. On days 4 and 5 a partial medium change was performed by removing 100 µL of

medium from each well and replacing it with 100 µL of fresh Airway Epithelial Cell Basal Medium (ATCC, Manassas, VA) supplemented with Bronchial Epithelial Cell Growth Kit (ATCC, Manassas, VA), 70 ng/ml phosphoethanolamine, 5 ng/ml epidermal growth factor (EGF), 100 U/mL penicillin, and 100 µg/mL streptomycin (Euroclone, UK) without FBS. On day 7 the spheroids were collected for subsequent analyses.

8.3 Isolation of sEVs from SW480 cells

SEVs were isolated from the conditioned medium of SW480 cells maintained in the presence of EVs-depleted FBS. The conditioned medium of the cells was collected after 24 hours of culture and subjected to several differential centrifugations followed by ultracentrifugation. Briefly, the conditioned medium was centrifuged at 300 x g for 5 min, 3000 x g for 15 min, and 10,000 x g for 30 min; the supernatant was then ultracentrifuged for 105 min at 100,000 × g in a Type 70 Ti fixed angle rotor. Then, the pellet of sEVs obtained was resuspended in 30 µL of PBS and quantified by the Bradford assay (Pierce, Rockford, IL, USA). sEVs were stored at -20°C. The concentrations and size distribution of the sEVs measured by Nanoparticle Tracking Analysis (NTA) (NanoSight NS300, Malvern Instruments Ltd, UK) and the morphological characterization of the isolated sEVs performed by trasmission electron microscope (TEM) analysis, were described in detail in our previous study [90].

8.4 Isolation of sEVs from human plasma

To validate the results obtained with sEVs derived from CRC cells, sEVs were also isolated from plasma of CRC patients and healthy donors. Following the instructions, the Total Exosome Isolation Kit (Invitrogen) was used to isolate sEVs from 100 µL of plasma samples. The plasma was initially centrifuged for 20 min at 2000 x g and for 20 min at 10,000 x g at room temperature. The supernatant was mixed with 50 µL of 1X PBS and vortexed, and 30 µL of exosome precipitation reagent was added to the samples and vortexed again. The samples were incubated at room temperature for 10 min and centrifuged for 5 min at 10,000 × g at room temperature. Finally, the pellet of sEVs was resuspended in 1X PBS and centrifuged for 30 seconds at 10,000 × g. After isolation, sEV pellets obtained from plasma samples were resuspended in 50 µl of PBS and quantified by the Bradford assay (Pierce, Rockford, IL, USA) [139]. sEVs were stored at -20 °C.

8.5 Treatment of 3D_Heps

To assess the impact of CRC-sEVs (SW480-sEVs, CRC/P-sEVs, and HS/sEVs) on 3D_Heps, a treatment protocol was implemented. On day 5 of culture, cells were treated with approximately $1.5x10^{10}$ particles/mL of sEVs, in line with our previous study [90]. Following 24 or 48h treatment, 3D_Heps were collected for further analyses.

8.6 Scanning Electron Microscope (SEM)

Morphological characterization of 3D_Heps was performed by scanning electron microscope (SEM). On day 7, the spheroids were collected in Eppendorf tubes and washed twice with 500 µL of PBS. After washing, they were fixed with 300 µL of 2.5 % glutaraldehyde, placed in a shaking refrigerator at 4ºC, and after further washes in PBS, stored in 500 µL of 70% EtOH. SEM analysis was performed in collaboration with Prof. Maria Cristina Guerrera, University of Messina.

8.7 Preparation of 3D_Heps sections

On day 7, 3D_Heps were collected into Eppendorf tubes, washed in PBS, and fixed in 2.5% glutaraldehyde. Following fixation, samples were processed for histological analysis.. Briefly, 3D_Heps were dehydrated through a graded ethanol series, cleared in xylene, and infiltrated with molten paraffin. Samples were then embedded in paraffin blocks, sectioned at 4–7 µm thickness using a rotary microtome, and mounted onto glass slides.

8.8 Hematoxylin–eosin staining of 3D_Heps sections

Paraffin sections (4 µm) of 3D_Heps were processed for hematoxylin–eosin (H&E) staining as follows. Sections were deparaffinized by two washes in 100% xylene for 10 min each. Rehydration was performed through a graded ethanol series (100%, 95%, 80%, and 70% ethanol; 5 min each), followed by immersion in distilled water for 10 min. Sections were then stained with hematoxylin and eosin according to standard histological procedures, dehydrated, cleared, and mounted for bright-field microscopic analysis.

8.9 sEVs labeling and uptake assay

To visualize cellular internalization of sEVs in 3D_Heps, sEVs derived from the SW480 cell line were labeled with PKH26, a lipophilic dye that emits red fluorescence. Briefly, the vesicles

were incubated with the dye for 20 min in the dark at room temperature, washed in PBS after three centrifugations at 18,800 x g for 10 min, resuspended in the medium and incubated with the cells for 3, 6 and 8 h at 37 ºC. After incubation, cells were fixed in PAF 4% and stained with ActinGreenTM 488 Ready ProbesR Reagent (Thermo Fisher, Waltham, MA, USA), which binds F-actin, and Hoechst (Molecular Probes, Life Technologies, USA) to stain nuclei, and observed with confocal microscopy (Nikon A1).

8.10 RealTime-Glo™ MT Cell Viability Assay

The cell viability of 3D_Heps after 48h of treatment with the sEVs derived from CRC cells or plasma was evaluated with RealTime-Glo™ MT Cell Viability Assay, according to the kit instructions (Promega). Briefly, 100 µL of medium containing the spheroid was transferred to a 96-well plate. Next, 100 µL of MT Cell Viability Substrate 1X and NanoLuc Substrate 1X were added to each well in a 1:1 ratio, and the plate was incubated for 30 min, 1 h and 2 h at 37º C. Upon completion, luminescence was recorded with Glomax.

8.11 LIVE/DEAD™ assay

The cell viability of the spheroids was assessed using the LIVE/DEAD™ Cell Viability assay, based on staining with Calcein-AM, which penetrates live cells with intact membranes and is hydrolyzed by active intracellular esterases to produce green fluorescence, and with Ethidium Homodimer-1, which penetrates only dead cells with compromised membranes, binding to DNA and producing red fluorescence.

3D_Hep/Ste were seeded in 96-well Ultra Low Attachment plates (Corning 96-well spheroid microplate, Ultra-Low Attachment surface) at a density of 1,500 cells per well, considering LX-2:THLE-2 cell ratios of 1:8 and 1:12; on the seventh day of culture, the medium was removed and the spheroids were incubated with 100–200 µL of the staining solution (5 µL calcein and 20 µL ethidium homodimer-1 in 10 mL DPBS) for 30 minutes at room temperature, and subsequently observed under a Nikon T1 confocal microscope.

8.12 Western Blot

3D_Heps were lysed by using RIPA buffer with protease inhibitors (Thermo Fisher Scientific, Waltham, MA, USA) (1:100 dilution) for 1 h on ice. The samples were centrifuged at 18,800 x g for 15 min at 4º C in order to precipitate cellular debris and nucleic acids; the supernatant

was then recovered and quantified by the Bradford assay (Pierce, Rockford, IL, USA) (18228490). Specifically, proteins were diluted 1:20 in H_2O; 1:20 solution in H_2O of Lysis Buffer was used as a blank. To the lysates protein, Reducing Agent (10X), and Sample Buffer (4X) were added, and placed in the thermoblock for 10 min at 70°C for denaturation of the sample. Proteins were separated on Bolt 4-12% Bis-Tris Plus precast polyacrylamide gels (Invitrogen by Thermo Fisher Scientific, Waltham, MA, USA). After electrophoresis, the proteins were transferred to a nitrocellulose membrane for blotting (Amersham Protran Premium 0.45 µm NC from GE HealthCare Life Science, Little Chalfont, Buckinghamshire, UK), blocked in 1% BSA in and incubated with the primary antibodies overnight at 4°C. The primary antibodies used were: anti-HNF4 (1:300 dilution; Santa Cruz Biotechnology, Dallas, TX, USA), anti-CK8/18 (1:300 dilution; Cell Signaling Technology, Danvers, MA, USA), anti-Vimentin (1:300 dilution; Cell Signaling Technology, Danvers, MA, USA), anti-N-Cadherin (1:300 dilution; Cell Signaling Technology, Danvers, MA, USA), anti-E-Cadherin (1:300 dilution; Cell Signaling Technology, Danvers, MA, USA), anti-β-actin (1:1000 dilution; Santa Cruz Biotechnology, Dallas, Tx, USA) and anti-GAPDH (1:1000 dilution; Santa Cruz Biotechnology, Dallas, TX, USA). After five washes with Tris-buffered saline + Tween 20 (TBS/T), the membrane was incubated with horseradish peroxidase (HRP)-conjugated goat anti-rabbit or anti-mouse secondary antibodies (1:1000 dilution; Thermo Fisher Scientific, Waltham, MA, USA) at room temperature for 1 h. The protein bands were visualized by enhanced chemiluminescence (ECL™ Prime Western Blotting System Cytiva RPN2232), using the chemiluminescence solution Amersham ECL Western Blotting Detection Reagent (GE Healthcare Life Sciences), prepared shortly before detection to the instrument by mixing in a 1:1 ratio Detection Reagent 1 and Detection Reagent 2. The signal detection was carried out with the "ChemiDocTMMP" Imaging System (Bio-Rad, Milan, Italy). Densitometric analysis of Western Blot was performed with the "Image J" software.

8.13 Confocal fluorescence microscopy in whole 3D_Heps

Following treatment with CRC-sEVs, the 3D_Heps were collected in Eppendorf tubes, and washed twice with 500 µL of PBS. After washing, they were fixed with 4% Paraformaldehyde (PAF), placed in a shaking refrigerator at 4ºC, and after further washes in PBS, incubated with 1% Triton X-100 for 1h at room temperature for permeabilization. After washing, spheroids were incubated overnight at room temperature with primary antibodies: anti-HNF4 (1:50 dilution; Santa Cruz Biotechnology, Dallas, TX, USA), anti-Ecadherin (1:50 dilution; Cell

Signaling Technology, Danvers, MA, USA), anti-Fibronectin (1:50 dilution; Cell Signaling Technology, Danvers, MA, USA), anti-Ncadherin (1:50 dilution; Cell Signaling Technology, Danvers, MA, USA), anti-CK8/18 (1:50 dilution; Cell Signaling Technology, Danvers, MA, USA), anti-Vimentin (1:50 dilution; Cell Signaling Technology, Danvers, MA, USA), anti-Tenascin (1:100 dilution; Antibodies.com, Stockolm, SE, EU) and anti-ZO-1 (1:50 dilution; Santa Cruz Biotechnology, Dallas, TX, USA). Once removed the unbound primary antibody by washing three times in PBS, the samples were incubated for 6 hours with DyLight 488 or DyLight 594 secondary antibody (dilution 1:500; Thermo Fisher Scientific, Waltham, MA, USA). The unbound secondary antibody was removed by performing three more washes in PBS. Next, the staining of the nuclei with Hoechst (1:1000 dilution; Molecular Probes, Life Technologies, Carlsbad, CA, USA), and of the cytoskeleton with Actin Green (1 drop/mL; Thermo Fisher, Waltham, MA, USA) was performed by overnight incubation. Finally, the 3D_Heps were resuspended in 70% glycerol and placed inside chambers for confocal analysis. Microscopy analysis was performed using a confocal microscope (Nikon Confocal A1).

8.14 Confocal fluorescence microscopy of 3D_Heps sections

Paraffin sections (7 μm thick) of 3D_Heps were obtained as described above. For immunofluorescence analysis, sections were deparaffinized by two washes in 100% xylene for 10 min each and rehydrated through a graded ethanol series (100%, 95%, 80%, and 70%; 5 min each), followed by immersion in distilled water for 10 min. Sections were then washed in PBS for 5 min and blocked with 1% BSA in PBS. Slides were incubated overnight at 4 °C with primary anti-HNF4 antibody (1:100; Santa Cruz Biotechnology, Dallas, TX, USA). After three washes in PBS to remove unbound antibody, sections were incubated for 1 h at room temperature with DyLight 488–conjugated secondary antibody (1:300; Thermo Fisher Scientific, Waltham, MA, USA). Following three additional PBS washes, nuclei were counterstained with Hoechst (1:1000; Molecular Probes, Life Technologies, Carlsbad, CA, USA) for 30 min at 4 °C. After final PBS washes, sections were imaged using a Nikon A1 confocal microscope.

8.15 ELISA (Enzyme-Linked Immunosorbent Assay)

Protein levels of Albumin, TGF-β, IL-6, Gas6, and Collagen type IV were assessed in the conditioned medium secreted from 3D_Heps after treatment of 24 h and 48 h with sEVs derived from CRC cells or plasma. The levels of each protein of interest were quantified by ELISA

assay, using specific kit (Thermo Fisher Scientific, Waltham, MA USA). The ELISA assay was conducted following the manufacturer's instructions. Absorbance was measured with a spectrophotometer at a wavelength of 450 nm.

8.16 W8 (Physical Cytometer Cell Dinamics)

On day 7, 3D_Heps were collected in Eppendorf tubes, washed in PBS, fixed in 2.5% glutaraldehyde, and stored in 70 % EtOH by the same protocol previously described for SEM analysis. The analyses were carried out in collaboration with Aten Center, through the automated platform W8 Physical Cytometer Cell Dynamics, useful for the physical characterization of three-dimensional cell models in terms of the physical parameters of diameter and mass density.

8.17 Generation of transgenic cells

The metastatic CRC cell line SW620 was infected with the lentiviral vector Lenti-CMV-GFP-2A-Puro (Applied Biological Materials Inc.). Briefly, the cells after reaching 70% confluence were permeabilized with 8 µg/mL Polybrene (Applied Biological Materials Inc.), and incubated for 30 min. Afterwards, the cells were infected with lentiviral particles (10^7 IU/mL), choosing the most optimal infection rate. Finally, the infected cells were selected, using the dose of 2 µg/mL Puromycin (Gibco™ puromycin dihydrochloride, cat. nº A1113802, Thermo Fisher® Scientific), and the fluorescence was observed at the confocal microscope (Nikon Confocal A1).

8.18 Invasion Assay

For the invasion assay, THLE-2 cells were seeded (1,500 cells x well) into 96-well multiwell (Corning 96-well Spheroid Microplate, Ultra-Low Attachement Surface) at day 0, and following the formation of 3D_Heps (described previously), co-culture with the SW620-GFP cells was performed, by adding 1000 cells x well in 100 µl of ATCC medium, at day 7. After 72 h, the spheroids were harvested for analyses at the confocal microscope (Nikon Confocal A1).

8.19 Statistical analysis

Statistical analysis was performed using GraphPad Prism 9.5.1 software (software GraphPad, Inc., La Jolla, California). The values shown in all graphs are the mean ± standard deviation (SD) of three replications unless otherwise indicated. Statistical significance was analyzed using the Welch T test, significant values of $p \leq 0.05$.

CHAPTER 9 - In vivo study: development of zebrafish larval CRC-xenografts

With the purpose of strengthening the biological relevance of our study, in collaboration with Professor Frederik Verweij, leader of the Extracellular Vesicle Biology group in the division of Cell Biology, Neurobiology, and Biophysics at Utrecht University, zebrafish (ZF) larvae were used as alternative *in vivo* models to study CRC-sEVs' biodistribution and role in tumor progression.

9.1 Intravenous injection of CRC-sEVs in ZF larvae

To have evidence of ZF larvae suitability in visualizing CRC-sEVs path within the embryo, CRC-sEVs were inoculated directly in the bloodstream, at the level of the Duct of Cuvier, an embryonic vein structure gathering all venous blood and directly leading to the heart's sinus venosus. Being able to track the sEVs represented a crucial part of this study. In most cases, the tracking of EVs distribution *in vivo* mainly relies on the use of lipophilic and fluorescent dyes, which, however, lack of specificity [146]. Therefore, to properly track SW480-sEVs within ZF larvae, a SW480 stable line expressing the sEV-marker CD63-pHluorin was generated (*Figure 39A*) and used as a source of genetically labeled CRC-sEVs, isolated and purified from cells' conditioned media via SEC.

To undertake this preliminary attempt, 5-10 nl of a suspension of $2x10^{10}$ sEVs/mL (100.000-200.000 sEVs), dose chosen accordingly to Professor Verweij's group expertise, was inoculated in the Duct of Cuvier (*Figure 39B*) of 2 days post fertilization (2dpf) ZF transgenic line Tg(*kdrl*:mCherry-CAAX), exhibiting mCherry-labeled endothelial cells (*Figure 39C, left panel*), allowing the visualization of the embryo's vasculature. The live imaging, performed 1h after injection (1hpi), showed the presence of SW480-CD63-pHluorin-sEVs in ZF vasculature and their uptake by endothelial cells (*Figure 39C, right panel*), revealing the suitability of the model to investigate the CRC-sEVs' biodistribution.

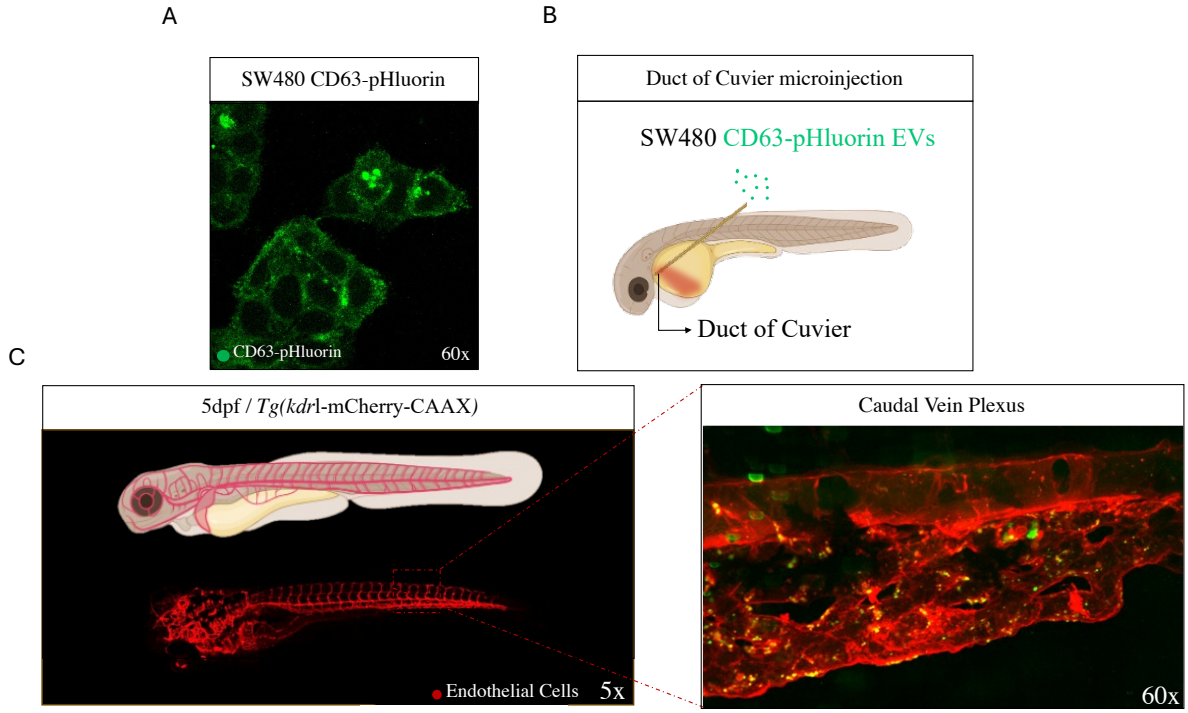

Figure 39 – **A**. Confocal micrographs showing the SW480-CD63-pHluorin stable cell line; CD63 is marked in green (60x magnification) **B**. Schematic representation of the intravenous injection of SW480 CD63-pHluorin sEVs in ZF larva's Duct of Cuvier; **C.** Left panel: imaging of 2dpf Tg(kdrl:mCherry-CAAX); endothelial cells are marked in red (5x magnification); right panel: imaging of 2dpf Tg(kdrl:mCherry-CAAX) injected in the Duct of Cuvier with SW480-CD63 pHluorin sEVs; endothelial cells are marked in red; SW480-sEVs are labelled in green; (imaging at 1hour post injection - 60x magnification).

9.2 Generation of zebrafish larvae CRC-xenografts

Once established the relevance of the model to visualize CRC-sEVs, we proceeded with our functional study aimed at unraveling the role of CRC-sEVs in liver metastasis development. To work with a more advanced system, accurately replicating the physiopathology of tumor progression, CRC-larval xenografts were generated, allowing to investigate the biodistribution of sEVs endogenously and continuously released by engrafted tumor cells and their effect on target cells. To follow SW480 cells and SW480-sEVs distribution in ZF larvae, SW480 stable lines dually expressing cytosolic cerulean and the sEV-marker CD63-pHluorin were generated (*Figure 40A*). For CRC cells engraftment, PVS, an avascular region considered the ideal injection site where to study migration and metastatic behavior, was chosen as injection site (*Figure 40B*).

The ZF transgenic line Tg(*fabp10:nls*-mCherry), exhibiting mCherry tagged Heps (*Figure 40C*) was used to study SW480-sEVs' transfer to the liver, the most common site of CRC-derived metastases. ZF larvae were injected at 2dpf in the PVS with approximately 500–1000 SW480-cerulean CD63-pHluorin cells, in line with previous literature findings [147][148]. The first day post injection (dpi) ZF xenografts presenting few cells, cardiac oedema, or with cells inside the yolk were discarded and only well-developed ones were kept for further experiments or imaging. The imaging at 3dpi revealed the presence in the PVS of a dense tumor mass and SW480-CD63-pHluorin-EVs were not only detected in ZF vasculature but also in the liver (*Figure 40D*), enhancing the relevance of ZF larval CRC-xenograft to investigate the role of CRC-sEVs in liver PMN formation and the following metastases establishment.

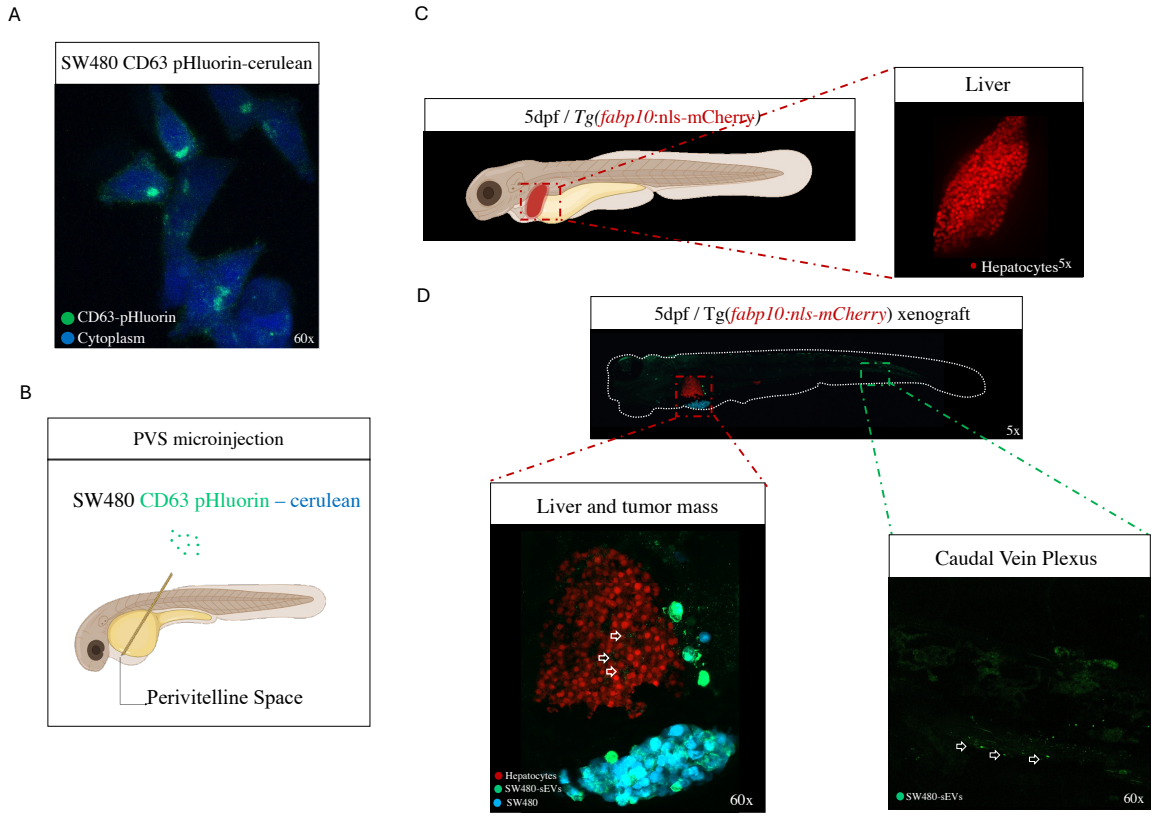

Figure 40 - **A**. Confocal micrographs of SW480-CD63-pHluorin-cerulean stable cell line CD63 is marked in green; cells are marked in blue (60x magnification) **B**. Schematic representation of SW480 CD63-pHluorin-cerulean microinjection in ZF larva's PVS; **C.** Left panel: representation of ZF transgenic line Tg(fabp10:nls-mCherry); right panel: imaging of the liver of 5dp ZF transgenic line Tg(fabp10:nls-mCherry); Heps are marked in red (5x magnification). D. Imaging of 5dpf Tg(fabp10:nls-mCherry) injected in the PVS with SW480 CD63-pHluorin-cerulean; Heps are marked in red, SW480 cells are marked in blue; SW480-sEVs are marked in green.

9.3 Future outlooks: generation of ZF larvae double CRC-xenografts

These promising results lay the ground for future investigations into the effects of CRC-derived sEVs on liver architecture and phenotypic changes in the ZF model. Specifically, we aim to evaluate whether these alterations in the liver parenchyma could facilitate the metastatic colonization of CRC cells.

To address this, we plan to incorporate the isogenic metastatic CRC cell line SW620 into our study. For cell tracking purposes, we generated a stable SW620 cell line expressing cytoplasmic cerulean (*Figure 41A*). This will allow to perform a double xenograft experiment: primary CRC cells (SW480 CD63-pHluorin) will first be engrafted into the PVS, simulating the primary tumor and releasing sEVs capable of reaching the liver, as previously demonstrated. Subsequently, SW620 cells will be injected intravenously to mimic circulating tumor cells.

An increased liver colonization by SW620 cells in ZF previously engrafted with SW480 cells would suggest that sEVs from the primary tumor induce microenvironmental changes that support metastatic seeding.

As a preliminary step, 5-10 nL of a suspension of 10^8 cells/mL of SW620-cerulean, in accordance with Professor Verweij's expertise, were microinjected into the Duct of Cuvier of ZF larvae at 2dpf to visualize their distribution (*Figure 41B*). The observed widespread metastases at 5dpf confirmed both the metastatic potential of SW620 cells and their suitability for this experimental model (*Figure 41C*).

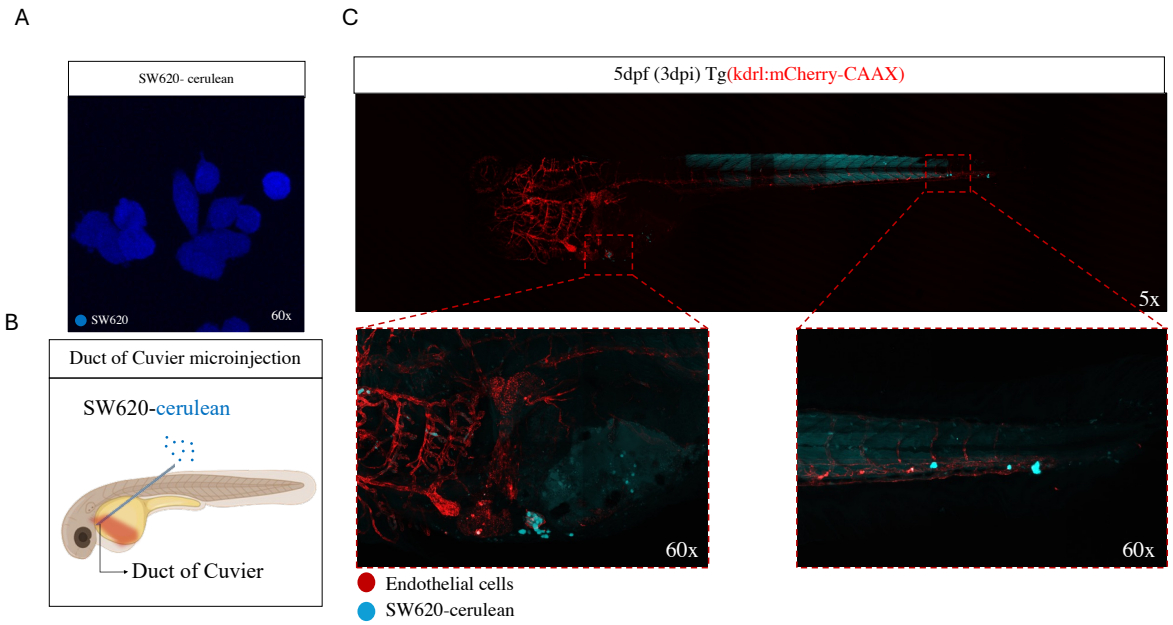

Figure 41 - A. Confocal micrographs of SW620-cerulean stable cell line; cells are marked in blue (60x magnification) **B**. Schematic representation of SW620-cerulean microinjection in ZF larva's Duct of Cuvier; **C**. Imaging of 5dpf Tg(kdrl-mCherry:CAAX) injected in the Duct of Cuvier with SW620-cerulean; endothelial cells are marked in red; SW620-cerulean are marked in blue.

CHAPTER 10 – Material and Methods: *In vivo* study

10.1 Cell culture mantainance

The isogenic CRC cell lines SW480 (ATCC CCL-228) and SW620 (ATCC CCL-227) derived respectively from a pre-metastatic primary tumor and lymph node metastasis, were used in this study. SW480 and SW620 cells were maintained in RPMI 1640 medium (Euroclone, UK) supplemented with 10% fetal bovine serum (FBS; Euroclone, UK), 2 mM L-glutamine (Euroclone, UK), 100 U/mL penicillin and 100 µg/mL streptomycin (Euroclone, UK). Before use, FBS (EU-approved South American origin, Euroclone, UK) was ultracentrifuged for 105 min at 100,000 ×g in type 70 Ti fixed-angle rotor. Fetal bovine serum is ultracentrifuged because it contains extracellular vesicles of animal origin that could contaminate the sample of interest [138].

HEK-293T cells were used as packaging cells for lentiviral particles production. Cells were mantained in DMEM (Euroclone, UK) supplemented with 10% fetal bovine serum (FBS; Euroclone, UK), 2 mM L-glutamine (Euroclone, UK), 100 U/mL penicillin and 100 µg/mL streptomycin (Euroclone, UK).

10.2 Generation of SW480 and SW620 stable cell lines

SW480 and SW620 cells were seeded in 12-well plates and mantained until 80% confluency was reached. Subsequently the cells were infected with lentiviral particles containing the sequences for CD63-pHluorin and/or cerulean. The infection was carried out in the presence of polybrene (Millipore Cat.#TR-1003-G, 10 mg/mL stock) diluted to 8 µg/mL to increase the infection rate. The lentiviral particles were removed 24h post infection, and the correctly infected cells were selected using blasticidin (ANT-DOXBL-1 RepTor Reagent Kit) diluted to 10 µg/mL. For the sorting of the stable cell line, cells were detached using trypsin, centrifuged, and resuspended in 10% FBS diluted in PBS. The cells were then sorted for GFP and/or cerulean signal using the FACSAria Cell Sorter.

10.3 Lentiviral particles production

For the production of lentiviral particles, HEK-293T cells were used as packaging cells. The cells were seeded in 10 cm^2 Petri dishes. Once they reached 50–60% confluence, the cells were transfected with a mixture of the following plasmids:

- 15 µg of the gene of interest (CD63-pHluorin and cerulean plasmids, kindly provided by Utrecht University);
- 10 µg of the psPAX2 vector, which encodes Gag, Pol, Rev, and Tat (Addgene Plasmid #12260, 2nd generation lentiviral packaging plasmid);
- 5 µg of the pMD2.G vector, which encodes the VSV-G envelope protein (Addgene Plasmid #12259);
- PEI MAX stock (PEI MAX® – Polysciences Cat.#24765-2) at a ratio of 3 µL per µg of DNA;
- Opti-MEM (Gibco™ Cat.#31985070), added to reach a final volume of 1.2 mL.

The transfection mixture was added to the cells, which were then transferred to a biosafety level II (ML-II) laboratory and incubated overnight at 37°C in 5% CO_2. The next day, the medium was removed and replaced with fresh DMEM.

On the following day, the supernatant containing the lentiviral particles was collected and filtered through 0.45 µm filters to remove cellular debris. The lentiviral suspension was then stored at −80°C.

10.4 SEVs isolation from cell cultures by SEC

SEVs were isolated from the conditioned medium collected after 48 hours of culture from SW480 cells. For collection of the conditioned medium, SW480 cells were seeded at a density of 35,000 cells/cm² in T175 flasks in RPMI 1640 culture medium (Euroclone UK), supplemented with 10% SEV-depleted FBS (Euroclone UK), 2 mM L-Glutamine (Euroclone UK), and 1% penicillin (100 U/mL) and streptomycin (100 µg/mL).

To deplete animal-derived sEVs, FBS was subjected to ultracentrifugation at 100,000 × g for 105 minutes using a fixed-angle rotor (70 Ti type). After centrifugation, the vesicle-containing pellet was discarded, and only the supernatant was collected.

Cells were then maintained in culture at 37°C with 5% CO_2 for 48 hours. Subsequently, the medium was removed and replaced with 40 mL of fresh culture medium. After an additional 24-hour culture period, the SW480-conditioned medium containing sEVs was collected and processed using the following differential centrifugation protocol:

- 300 × g for 5 minutes at 4°C to remove dead cells and cell debris
- 3,000 × g for 15 minutes at 4°C to eliminate apoptotic bodies
- 10,000 × g for 30 minutes at 4°C to remove microvesicles

The resulting supernatant was then concentrated using Amicon Ultra-15 centrifugal filter units with a 100 kDa molecular weight cut-off (Merck Millipore, UFC910008). Specifically, 40 mL of conditioned medium were concentrated by repeated centrifugation at 4°C, 4,000 × g for 40 minutes until reaching a final volume of 500 µL. This concentrate was used for extracellular vesicle isolation via size-exclusion chromatography (SEC).

SEC was performed using IZON qEVoriginal/35 nm columns (ICO-35). According to the manufacturer's instructions, the column was equilibrated at room temperature (18–24°C) and activated by adding 17 mL of sterile, filtered PBS (Euroclone). Next, the 500 µL of concentrated conditioned medium were loaded onto the column. Once fully absorbed into the resin, elution was initiated using 8.5 mL of sterile, filtered PBS.

During elution, an initial 2.9 mL exclusion volume (VOID) was collected, followed by sequential collection of 400 µL fractions. In accordance to the DLS analysis, the firs three fractions were pooled and the particle number and concentration were quantified using Nanoparticle Tracking Analysis (NTA), which tracks individual vesicles via phase contrast microscopy and Brownian motion analysis. The resulting SEVs were stored at −80°C until further use.

10.5 Zebrafish housing and maintenance

In vivo experiments have been performed in zebrafish (*Danio rerio*) embryos from 0 to 5 dpf, in accordance with European Animal Welfare Legislation "on the protection of animals used for scientific purposes", following the 3Rs principles (Convention ETS - No. 123, Directive No. 2010/63/EU). At Utrecht University, adult ZF were maintained in tanks in a continuous flow system ZebTec (Techniplast). Tanks were filled with reverse osmosis water and 15% daily water exchange, kept at 28 °C and photoperiod of 10h dark and 14h light. ZF were fed two times a day with Gemma Micron 300 (Skretting) and once with live brine shrimp. Male and female fish (1:1 ratio) were separated the night before mating and placed in the same tank with a divider separating them. The following morning, the divider was removed, and embryos were collected and transferred to 10cm petri dishes containing E3 embryo medium (5 mM NaCl, 0.17 mM KCl, 0.33 mM $CaCl_2 \cdot 2H_2O$, 0.33 mM $MgSO_4 \cdot 7H_2O$), and kept at 28°C in incubators. Undeveloped or dead embryos were discarded and the alive ones were put in fresh embryo medium, to prevent toxicity due to the release of necrotic factors. At 2 dpf, chorions were manually removed one by one under the microscope using very sharp forceps in all embryos that had not yet hatched. Subsequently embryos were injected in either the Duct of

Cuvier for sEVs intravenous injection or in PVS for CRC-xenografts generation. Prior to the injection, emrbyos were anesthesized by exposure to 164 mg/L Tricaine mesylate at pH=7 (Ethyl 3-aminobenzoate, MS-222, Sigma-Aldrich® Cat.#E10521) dissolved in embryo medium. Our experimental design did not need ethical committee approval as embryos used were beyond the stage defined as an animal experiment (≤ 5dpf). The transgenic ZF line Tg(*fabp10*a:nls-mcherry) and Tg(*kdrl*:mCherry-CAAX), previously established and maintained in Utrecht University, were used throughout the study.

10.6 Microinjection needle preparation

Microinjection needle were prepared by pulling borosilicate glass capillaries (Harvard Apparatus, 30-0019 Cat.#GC100F- 10). in a Sutter Instrument® Model P-30 vertical micropipette puller ((Heat: 500-600; FiI: 10; Velocity: 50; Delay: 60; Pull: 100)

10.7 ZF plate set up

ZF plate for micorinjection were made by using the lid of a 10cm Petri dish. A solution of 3% Agar in H_2O or 2% Agarose in H_2O has been prepared and poured in the lid of dish until reaching a bit more than a half of the lid. Once dried, vertical lines, useful for embryos alignment, were created by pouring with the same Agar/Agarose solution with a plastic Pasteur.

10.8 Intravenous injection of sEVs in zebrafish embryos

To perform intravenous injection in ZF, 2 dpf embryos were anaesthetized into a 10 cm-Petri dish with 1X Tricaine in Egg water-medium for approximately 5 min. Once anaestetized, embryo were aligned onto a 10cm-Petri dish previously coated with 2% agarose. Following this, a suspension of approximately $2x10^{10}$ sEVs/mL was loaded into a borosilicate capillary using a microloader tip (EppendorfTM, Cat.#5242956003). The borosilicate capillary was then mounted into a SYS-PV820 Pneumatic PicoPump (World Precision Instruments) set as follows: Hold pressure= vent (3 psi); Eject pressure= vent; Range= 100 ms), and oriented with the tip towards the Duct of Cuvier of the embryo, as shown in *Figure 42*. By using sharp tweezors, the tip of the capillary was cut to obtain an oblique angled-end, thin enough to penetrate the skin, without damaging the embryo. Once reached the Duct of Cuvier, a range from 5 nL to 10 nL of a $2x10^{10}$ sEVs/mL suspension was microinjected.

Following the microinjection procedure, the embryos were placed in a 10 cm Petri dish containing 1X Tricaine in Egg water medium for approximately 5 minutes to immobilize them and prevent any movement that could disrupt or reopen the injection site.

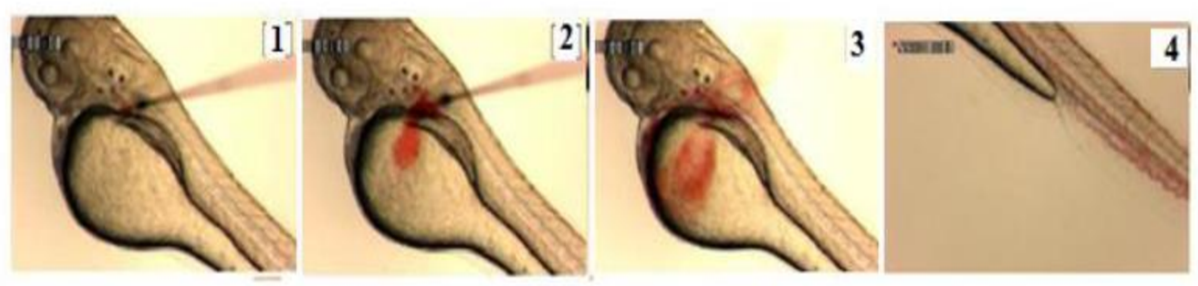

Figure 42. Representive image of ZF Duct of Cuvier injection (Image from Inflammatory effects in zebrafish (Danio rerio) exposed to gold nanoparticles, Eline Skadberg, 2015, Environmental Science, Biology).

10.9 Generation of ZF CRC larval xenografts

To generate CRC larval xenografts, CRC cells to engraft were brought at 90% confluence into a 10 cm Petri dish and after two washes in PBS 1X cells were detached with EDTA and a cell scraper and pelleted at 300 x g for 5 min at 4°C. After one wash in 1X PBS, the cell pellet was resuspended in sterile 1X PBS into a 1.5 mL-EppendorfTM tube reaching a concentration of ~0.25-0.5 x10^6 cells/µL, and kept at 4° until the injection.

ZF embryos at 2 dpf were then anaesthetized into a 10 cm-Petri dish with 1X Tricaine in Egg water-medium for 5 min. Subsequently, embryos were aligned on a 10cm Petri-dish coated with 2% agarose by using an hairpin loop. Cells were then resuspended by gentle tapping, aspirated, and loaded into a borosilicate capillary using a microloader tip (EppendorfTM, Cat.#5242956003). The tip of the capillary was cut with with sharp tweezors to create a blunt end. For the microinjection, we used SYS-PV820 Pneumatic PicoPump (World Precision Instruments) set as follows: Hold pressure= vent (3 psi); Eject pressure= vent; Range= 100 ms. The embryo's yolk was then pierced in the middle, lowering the angle of the needle, and afterwars the tip was pushed until reaching the PVS (*Figure 43*). By pressing the microinjector pedal, a volume of cells similar to the size of the embryo's eye was injected, as far as possible from the heart to prevent cardiac edema.

In case of cells clogging, the pressure was slightly increased and/or the capillary tip further cut.

During the whole procedure, a film of 1X Tricain in Egg-water has been added, to prevent embryos from drying.

.

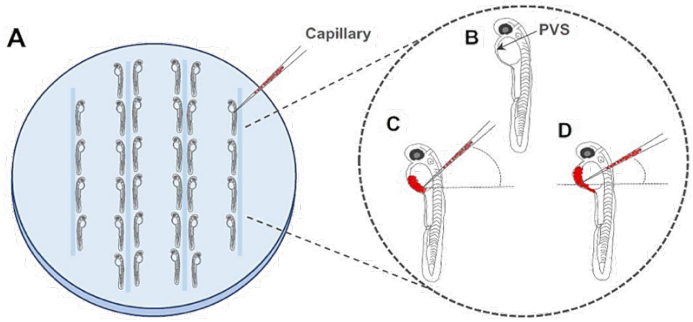

Figure 14 - Schematic representation of ZF xenograft plate set up: A. Alignment of anaesthetized embryos in 2% Agarose plate. Image from Martinez-Lopez et al., J. Vis. Exp, 2021 [130].

After injection, the xenografts were transferred to a fresh 10 cm Petri dish containing 1X Tricaine in Egg water medium and incubated for 5 minutes to minimize movement and reduce the risk of disrupting the injection site; afterward, embryos were moved to fresh Egg-water medium in a 10 cm Petri dish and incubated at 34°C, a compromise temperature between the ideal temperature for engrafted human cells growth (37°) and ZF development (28°).
The first day post injection (dpi), only well-injected ZF xenografts were selected for further sperimentation or imaging; whereas those containing few cells, presenting cardiac oedema, or with cells inside the yolk were discarded (*Figure 44*).

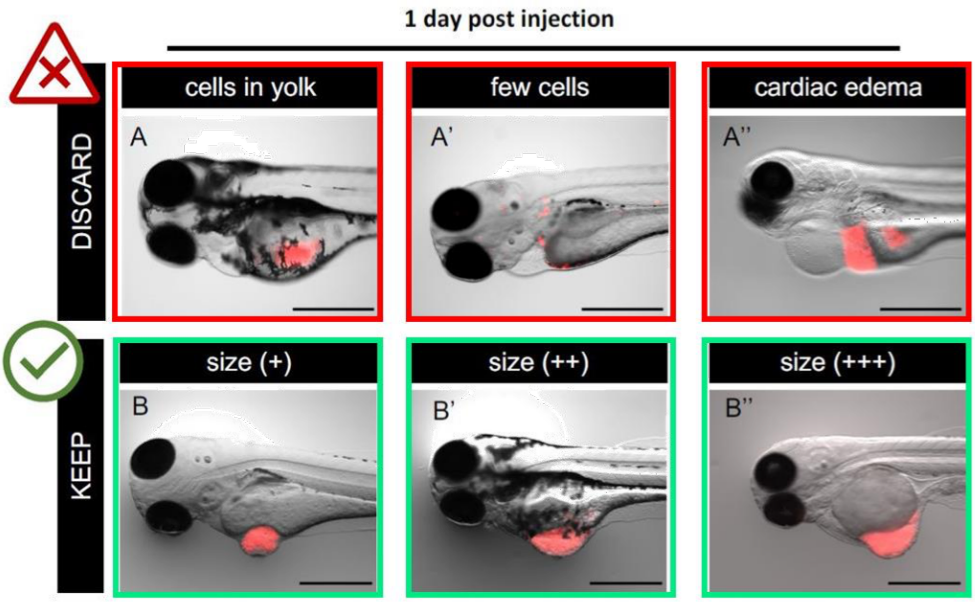

Figure 44 - Illustrative fluorescent stereomicroscope images of ZF xenografts at 1dpi, badly injected (A, A'), exhibiting oedema (A'') and well-injected (B, B', and B''). Scalebars: 500 µm. Image from Martinez-Lopez et al., J. Vis. Exp, 2021 [130].

10.10 ZF whole mount fixation and imaging

To perform the whole mount fixation of ZF embryos, embryos were euthanized by using an overdose of tricaine. Subsequently embryos were fixed overnight at 4°C in 4% paraformaldehyde (PFA) containing sucrose, ensuring that fixation does not exceed one night to minimize autofluorescence. After fixation, the embryos were rinsed three times with PBS without calcium or magnesium ions, as these can also increase autofluorescence. Next, the PBS was aspirated and the embryos suspended in 3% methylcellulose. On a cover slide, a silicone border was applied and subsequently the embryos suspended in methylcellulose were placed at the center of the coverslip. A square cover glass was then placed on top of the coverglass to seal the sample, ensuring the emrbyos are immobilized an ready for further imaging or analysis. The entire procedure is illustrated schematically in *Figure 45*.

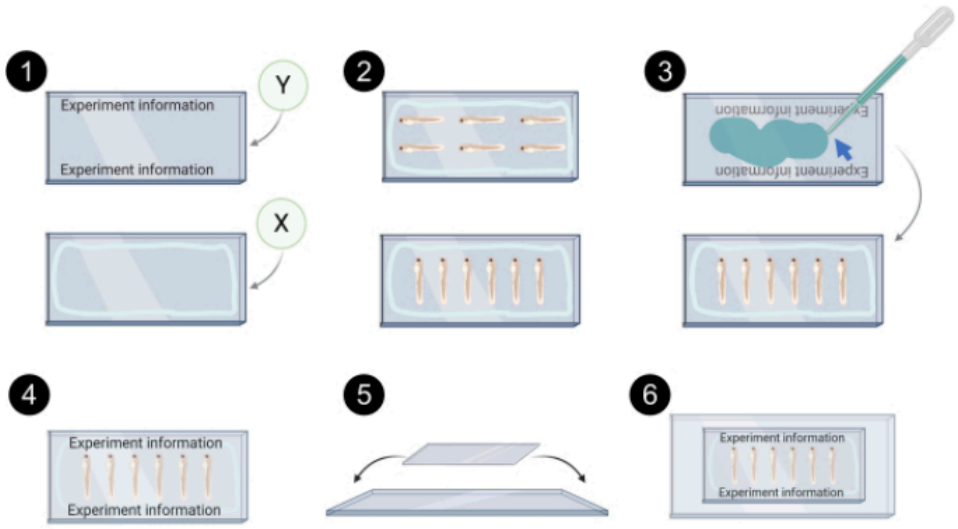

Figure 45 - Schematic representation of xenograft mounting. Image from Martinez-Lopez et al., J. Vis. Exp, 2021 [130].

10.11 ZF live-mounting

For ZF live mounting, the embryos were embedded in a solution of 2% agarose in Tricaine 1x solution. A drop of the solution embedding the embryo was placed at the bottom of a fluorodish. By using a homemade hairpin loop, the embryos were placed in the proper position for the observations needed. After the agarose 2% was completely dry, low melting agarose 0.8% has been added all over the fluorodish. Once the low melting agarose 0.8 % was dried, embryo water with Tricaine 1X was added.

CHAPTER 11 – *Conclusions*

This study provides clear evidence that Heps, traditionally considered uninvolved in the early stages of metastatic progression, actually play an active and multifaceted role in shaping the hepatic PMN associated with CRC. By demonstrating that CRC-sEVs can directly modulate Heps behavior, inducing the nuclear delivery of vescicles-associated PD-L1 and the consequent upregulation of alternative immune checkpoints VISTA and PD-L2, we reveal a novel immunomodulatory mechanism that supports an immunosuppressive microenvironment favorable to metastatic seeding.

Moreover, the adoption of a hepatocyte spheroid model provided physiologically relevant insights into the pro-fibrotic and EMT-related transformations elicited by CRC-sEV-educated Heps, highlighting their contribution to ECM remodeling and fibrogenic niche formation.

Lastly, the *in vivo* validation using the ZF larval xenograft model further confirmed the translational relevance of these findings, offering a powerful and ethically sustainable platform for dynamic visualization of metastatic niche development and for testing future therapeutic strategies.

Altogether, this work uncovers a previously underestimated role of Heps as active players of the pre-metastatic liver environment, pointing to hepatocyte–tumor crosstalk as a promising therapeutic target for intercepting metastatic initiation, thereby laying the foundation for innovative interventions in colorectal cancer.

CHAPTER 12 – *Bibliography*

[1] Alireza Ansary Moghaddam 1, Mark Woodward, Rachel Huxley, "Obesity and risk of colorectal cancer: a meta-analysis of 31 studies with 70,000 events," *Cancer Epidemiol Biomarkers Prev*, vol. 2007, no. PMID: 18086756, doi: 10.1158/1055-9965.EPI-07-0708.

[2] Zhang X, Fan H, Han S, Zhang T, Sun Y, Yang L, Li W., "Global burden of colon and rectal cancer and attributable risk factors in 204 countries and territories from 1990 to 2021," *BMC Gastroenterol.*, vol. 2025, no. PMID: 40316922, doi: 10.1186/s12876-025-03948-2.

[3] Lei Wu 1, Chao Yu, Han Jiang, Jun Tang, He-lang Huang, Jing Gao, Xin Zhang, "Diabetes mellitus and the occurrence of colorectal cancer: an updated meta-analysis of cohort studies," *Diabetes Technol Ther* ., vol. 2013, no. PMID: 23540566, doi: 10.1089/dia.2012.0263.

[4] Nguyen SP, Bent S, Chen YH, Terdiman JP., "Gender as a risk factor for advanced neoplasia and colorectal cancer: a systematic review and meta-analysis," *Gastroenterol Hepatol.*, vol. 2009, no. PMID: 19514116, doi: 10.1016/j.cgh.2009.01.008.

[5] Afzaninawati Suria Yusof 1, Zaleha Md Isa, Shamsul Azhar Shah, "Dietary patterns and risk of colorectal cancer: a systematic review of cohort studies (2000-2011)," *Asian Pac J Cancer Prev* ., vol. 2012, no. PMID: 23167408, doi: 10.7314/apjcp.2012.13.9.4713.

[6] Ollberding NJ, Nomura AM, Wilkens LR, Henderson BE, Kolonel LN., "Racial/ethnic differences in colorectal cancer risk: the multiethnic cohort study.," *Int J Cancer.*, vol. 2011, no. PMID: 21128280, doi: 10.1002/ijc.25822.

[7] Botteri E, Borroni E, Sloan EK, Bagnardi V, Bosetti C, Peveri G, Santucci C, Specchia C, van den Brandt P, Gallus S, Lugo A., "Smoking and Colorectal Cancer Risk, Overall and by Molecular Subtypes: A Meta-Analysis," *Am J Gastroenterol.*, vol. 2020, no. PMID: 32773458, doi: 10.14309/ajg.0000000000000803.

[8] Fedirko V, Tramacere I, Bagnardi V, Rota M, Scotti L, Islami F, Negri E, Straif K, Romieu I, La Vecchia C, Boffetta P, Jenab M., "Alcohol drinking and colorectal cancer risk: an overall and dose-response meta-analysis of published studies," *Ann Oncol.*, vol. 2011, no. PMID: 21307158, doi: 10.1093/annonc/mdq653.

[9] Rebuzzi F, Ulivi P, Tedaldi G., "Genetic Predisposition to Colorectal Cancer: How Many and Which Genes to Test?," *Int J Mol Sci.*, vol. 2023, no. PMID: 36768460, doi: 10.3390/ijms24032137.

[10] Brooke Dubansky, Sally Lewis and Dale Telgenhoff, “Classification and Histological Characteristics of Colorectal Cancer,” *American Society for Clinical Laboratory Science*, vol. 2024, doi: 10.29074/ascls.2022003206.

[11] Fearon ER, Vogelstein B., “A genetic model for colorectal tumorigenesis.,” *Cell.*, vol. 1990, no. PMID: 2188735, doi: 10.1016/0092-8674(90)90186-i.

[12] Rumpold H, Niedersüß-Beke D, Heiler C, Falch D, Wundsam HV, Metz-Gercek S, Piringer G, Thaler J., “Prediction of mortality in metastatic colorectal cancer in a real-life population: a multicenter explorative analysis.,” *BMC Cancer*, vol. 2020, no. PMID: 33238958, doi: 10.1186/s12885-020-07656-w.

[13] Shin AE, Giancotti FG, Rustgi AK., “Metastatic colorectal cancer: mechanisms and emerging therapeutics,” *Trends Pharmacol Sci.*, vol. 2023, no. PMID: 36828759, doi: 10.1016/j.tips.2023.01.003.

[14] Nagao K, Koshino A, Sugimura-Nagata A, Nagano A, Komura M, Ueki A, Ebi M, Ogasawara N, Tsuzuki T, Kasai K, Takahashi S, Kasugai K, Inaguma S., “The Complete Loss of p53 Expression Uniquely Predicts Worse Prognosis in Colorectal Cancer.,” *Int J Mol Sci.*, vol. 2022, no. PMID: 35328677, doi: 10.3390/ijms23063252.

[15] Zehir A, Benayed R, et al., “Mutational landscape of metastatic cancer revealed from prospective clinical sequencing of 10,000 patients.,” *Nat Med.*, vol. 2017, no. PMID: 28481359, doi: 10.1038/nm0817-1004c.

[16] Bakir B, Chiarella AM, Pitarresi JR, Rustgi AK., “EMT, MET, Plasticity, and Tumor Metastasis.,” *Trends Cell Biol.*, vol. 2020, no. PMID: 32800658, doi: 10.1016/j.tcb.2020.07.003.

[17] Aiello NM, Maddipati R, Norgard RJ, Balli D, Li J, Yuan S, Yamazoe T, Black T, Sahmoud A, Furth EE, Bar-Sagi D, Stanger BZ., “EMT Subtype Influences Epithelial Plasticity and Mode of Cell Migration.,” *Dev Cell.*, vol. 2018, no. PMID: 29920274, doi: 10.1016/j.devcel.2018.05.027.

[18] Sahai E, Astsaturov I, Cukierman E, DeNardo DG, Egeblad M, Evans RM, Fearon D, Greten FR, Hingorani SR, Hunter T, Hynes RO, Jain RK, Janowitz T, Jorgensen C, Kimmelman AC, Kolonin MG, Maki RG, Powers RS, Puré E, Ramirez DC, Scherz-Shouval R, Sherman MH, Stewart S, Tlsty TD, Tuveson DA, Watt FM, Weaver V, Weeraratna AT, Werb Z., “A framework for advancing our understanding of cancer-associated fibroblasts.,” *Nat Rev Cancer.*, vol. 2020, no. PMID: 31980749, doi: 10.1038/s41568-019-0238-1.

[19] Tommelein J, Verset L, Boterberg T, Demetter P, Bracke M, De Wever O., "Cancer-associated fibroblasts connect metastasis-promoting communication in colorectal cancer.," *Front Oncol.*, vol. 2015, no. PMID: 25853091, doi: 10.3389/fonc.2015.00063.

[20] Mantovani A, Sozzani S, Locati M, Allavena P, Sica A., "Macrophage polarization: tumor-associated macrophages as a paradigm for polarized M2 mononuclear phagocytes.," *Trends Immunol.*, vol. 2002, no. PMID: 12401408, doi: 10.1016/s1471-4906(02)02302-5.

[21] Huppert LA, Green MD, Kim L, Chow C, Leyfman Y, Daud AI, Lee JC., "Tissue-specific Tregs in cancer metastasis: opportunities for precision immunotherapy.," *Cell Mol Immunol.*, vol. 2022, no. PMID: 34417572, doi: 10.1038/s41423-021-00742-4.

[22] Allemailem KS et al., "Innovative Strategies of Reprogramming Immune System Cells by Targeting CRISPR/Cas9-Based Genome-Editing Tools: A New Era of Cancer Management.," *Int J Nanomedicine*, vol. 2023, no. PMID: 37795042, doi: 10.2147/IJN.S424872.

[23] Clark AM, Ma B, Taylor DL, Griffith L, Wells A., "Liver metastases: Microenvironments and ex-vivo models.," *Exp Biol Med (Maywood).*, vol. PMID: 27390264, doi: 10.1177/1535370216658144.

[24] Faivre J, Manfredi S, Bouvier AM., "Epidémiologie des métastases hépatiques des cancers colorectaux [Epidemiology of colorectal cancer liver metastases].," *Bull Acad Natl Med.*, vol. 2003, no. PMID: 14979048.

[25] Horn SR, Stoltzfus KC, Lehrer EJ, Dawson LA, Tchelebi L, Gusani NJ, Sharma NK, Chen H, Trifiletti DM, Zaorsky NG., "Epidemiology of liver metastases.," *Cancer Epidemiol.*, vol. 2020, no. PMID: 32562887, doi: 10.1016/j.canep.2020.101760.

[26] Olaso E, Santisteban A, Bidaurrazaga J, Gressner AM, Rosenbaum J, Vidal-Vanaclocha F., "Tumor-dependent activation of rodent hepatic stellate cells during experimental melanoma metastasis.," *Hepatology*, vol. 1997, no. PMID: 9303493, doi: 10.1002/hep.510260315.

[27] Friedman SL., "Hepatic stellate cells: protean, multifunctional, and enigmatic cells of the liver.," *Physiol Rev.*, vol. 2008, no. PMID: 18195085, doi: 10.1152/physrev.00013.2007.

[28] Mazzocca A, Coppari R, De Franco R, Cho JY, Libermann TA, Pinzani M, Toker A., "A secreted form of ADAM9 promotes carcinoma invasion through tumor-stromal interactions.," *Cancer Res.*, vol. 2005, no. PMID: 15930291, doi: 10.1158/0008-5472.CAN-04-4449.

[29] Eveno C, Hainaud P, Rampanou A, Bonnin P, Bakhouche S, Dupuy E, Contreres JO, Pocard M., "Proof of prometastatic niche induction by hepatic stellate cells.," *J Surg Res.*, vol. 2015, no. PMID: 25528682, doi: 10.1016/j.jss.2014.11.005.

[30] Copple BL, Bai S, Burgoon LD, Moon JO., "Hypoxia-inducible factor-1α regulates the expression of genes in hypoxic hepatic stellate cells important for collagen deposition and angiogenesis.," *Liver Int.*, vol. 2011, no. PMID: 20880076, doi: 10.1111/j.1478-3231.2010.02347.x.

[31] Huang WH, Zhou MW, Zhu YF, Xiang JB, Li ZY, Wang ZH, Zhou YM, Yang Y, Chen ZY, Gu XD., "The Role Of Hepatic Stellate Cells In Promoting Liver Metastasis Of Colorectal Carcinoma.," *Onco Targets Ther.*, vol. 2019, no. PMID: 31571908, doi: 10.2147/OTT.S214409.

[32] Bilzer M, Roggel F, Gerbes AL., "Role of Kupffer cells in host defense and liver disease.," *Liver Int.*, vol. 2006, no. PMID: 17105582, doi: 10.1111/j.1478-3231.2006.01342.x.

[33] Braet F, Nagatsuma K, Saito M, Soon L, Wisse E, Matsuura T., "The hepatic sinusoidal endothelial lining and colorectal liver metastases.," *World J Gastroenterol.*, vol. 2007, no. PMID: 17352008, doi: 10.3748/wjg.v13.i6.821.

[34] Benedicto A, Herrero A, Romayor I, Marquez J, Smedsrød B, Olaso E, Arteta B., "Liver sinusoidal endothelial cell ICAM-1 mediated tumor/endothelial crosstalk drives the development of liver metastasis by initiating inflammatory and angiogenic responses.," *Sci Rep.*, vol. 2019, no. PMID: 31511625, doi: 10.1038/s41598-019-49473-7.

[35] Zuo Y, Ren S, Wang M, Liu B, Yang J, Kuai X, Lin C, Zhao D, Tang L, He F., "Novel roles of liver sinusoidal endothelial cell lectin in colon carcinoma cell adhesion, migration and in-vivo metastasis to the liver.," *Gut.*, vol. 2013, no. PMID: 22637699, doi: 10.1136/gutjnl-2011-300593.

[36] Tremblay PL, Huot J, Auger FA., "Mechanisms by which E-selectin regulates diapedesis of colon cancer cells under flow conditions.," *Cancer Res.*, vol. 2008, no. PMID: 18593916, doi: 10.1158/0008-5472.CAN-08-1229.

[37] Mook OR, van Marle J, Jonges R, Vreeling-Sindelárová H, Frederiks WM, Van Noorden CJ., "Interactions between colon cancer cells and hepatocytes in rats in relation to metastasis.," *J Cell Mol Med.*, vol. 2008, no. PMID: 18208563, doi: 10.1111/j.1582-4934.2008.00242.x.

[38] Tabariès S, Dupuy F, Dong Z, Monast A, Annis MG, Spicer J, Ferri LE, Omeroglu A, Basik M, Amir E, Clemons M, Siegel PM., "Claudin-2 promotes breast cancer liver

metastasis by facilitating tumor cell interactions with hepatocytes.," *Mol Cell Biol.*, vol. 2012, no. PMID: 22645303, doi: 10.1128/MCB.00299-12.

[39] Paget S., "The distribution of secondary growths in cancer of the breast. 1889," *Cancer Metastasis Rev.*, vol. 1989, no. PMID: 2673568..

[40] Kaplan RN, Riba RD, Zacharoulis S, Bramley AH, Vincent L, Costa C, MacDonald DD, Jin DK, Shido K, Kerns SA, Zhu Z, Hicklin D, Wu Y, Port JL, Altorki N, Port ER, Ruggero D, Shmelkov SV, Jensen KK, Rafii S, Lyden D., "EGFR1-positive haematopoietic bone marrow progenitors initiate the pre-metastatic niche.," *Nature*, vol. 2005, no. PMID: 16341007, doi: 10.1038/nature04186.

[41] Huang Y, Song N, Ding Y, Yuan S, Li X, Cai H, Shi H, Luo Y., "Pulmonary vascular destabilization in the premetastatic phase facilitates lung metastasis.," *Cancer Res.*, vol. 2009, no. PMID: 19773447, doi: 10.1158/0008-5472.CAN-08-4382.

[42] Cohen N, Mundhe D, Deasy SK, Adler O, Ershaid N, Shami T, Levi-Galibov O, Wassermann R, Scherz-Shouval R, Erez N., "Breast Cancer-Secreted Factors Promote Lung Metastasis by Signaling Systemically to Induce a Fibrotic Premetastatic Niche.," *Cancer Res.*, vol. 2023, no. PMID: 37548552, doi: 10.1158/0008-5472.CAN-22-3707.

[43] Deguchi A, Maru Y., "Inflammation-associated premetastatic niche formation.," *Inflamm Regen.*, vol. 2022, no. PMID: 35780158, doi: 10.1186/s41232-022-00208-8.

[44] Patras L, Shaashua L, Matei I, Lyden D., "Immune determinants of the pre-metastatic niche.," *Cancer Cell.*, vol. 2023, no. PMID: 36917952, doi: 10.1016/j.ccell.2023.02.018.

[45] Li R, Qi Y, Jiang M, Zhang T, Wang H, Wang L, Han M., "Primary tumor-secreted VEGF induces vascular hyperpermeability in premetastatic lung via the occludin phosphorylation/ubiquitination pathway.," *Mol Carcinog.*, vol. 2019, no. PMID: 31553086, doi: 10.1002/mc.23120.

[46] Lauta VM., "A review of the cytokine network in multiple myeloma: diagnostic, prognostic, and therapeutic implications.," *Cancer*, vol. 2003, no. PMID: 12733143, doi: 10.1002/cncr.11072.

[47] Fischer JR, Darjes H, Lahm H, Schindel M, Drings P, Krammer PH., "Constitutive secretion of bioactive transforming growth factor beta 1 by small cell lung cancer cell lines.," *Eur J Cancer.*, vol. 1994, no. PMID: 7857713, doi: 10.1016/0959-8049(94)00364-b.

[48] Wendt MK, Allington TM, Schiemann WP., "Mechanisms of the epithelial-mesenchymal transition by TGF-beta.," *Future Oncol.*, vol. 2009, no. PMID: 19852727, doi: 10.2217/fon.09.90.

[49] Cao R, Bråkenhielm E, Pawliuk R, Wariaro D, Post MJ, Wahlberg E, Leboulch P, Cao Y., "Angiogenic synergism, vascular stability and improvement of hind-limb ischemia by a combination of PDGF-BB and FGF-2.," *Nat Med.*, vol. 2003, no. PMID: 12669032, doi: 10.1038/nm848.

[50] Bronzert DA, Pantazis P, Antoniades HN, Kasid A, Davidson N, Dickson RB, Lippman ME., "Synthesis and secretion of platelet-derived growth factor by human breast cancer cell lines.," *c Natl Acad Sci U S A.*, vol. 1987, no. PMID: 3039506, doi: 10.1073/pnas.84.16.5763.

[51] Niland S, Riscanevo AX, Eble JA., "Matrix Metalloproteinases Shape the Tumor Microenvironment in Cancer Progression.," *Int J Mol Sci.*, vol. 2021, no. PMID: 35008569, doi: 10.3390/ijms23010146.

[52] Weinberg F, Ramnath N, Nagrath D., "Reactive Oxygen Species in the Tumor Microenvironment: An Overview.," *Cancers (Basel).*, vol. 2019, no. PMID: 31426364, doi: 10.3390/cancers11081191.

[53] Mehnert JM, McCarthy MM, Jilaveanu L, Flaherty KT, Aziz S, Camp RL, Rimm DL, Kluger HM., "Quantitative expression of VEGF, VEGF-R1, VEGF-R2, and VEGF-R3 in melanoma tissue microarrays.," *Hum Pathol.*, vol. 2010, no. PMID: 20004943, doi: 10.1016/j.humpath.2009.08.016.

[54] Pabla B, Bissonnette M, Konda VJ., "Colon cancer and the epidermal growth factor receptor: Current treatment paradigms, the importance of diet, and the role of chemoprevention.," *World J Clin Oncol.*, vol. 2015, no. PMID: 26468449, doi: 10.5306/wjco.v6.i5.133.

[55] van Niel G, D'Angelo G, Raposo G., "Shedding light on the cell biology of extracellular vesicles.," *Nat Rev Mol Cell Biol.*, vol. 2018, no. PMID: 29339798, doi: 10.1038/nrm.2017.125.

[56] Abels ER, Breakefield XO., "Introduction to Extracellular Vesicles: Biogenesis, RNA Cargo Selection, Content, Release, and Uptake," *Cell Mol Neurobiol.*, vol. 2016, no. PMID: 27053351, doi: 10.1007/s10571-016-0366-z.

[57] Urabe F, Kosaka N, Ito K, Kimura T, Egawa S, Ochiya T., "Extracellular vesicles as biomarkers and therapeutic targets for cancer.," *Am J Physiol Cell Physiol.*, vol. 2020, no. PMID: 31693397, doi: 10.1152/ajpcell.00280.2019.

[58] Hallal S, Tűzesi Á, Grau GE, Buckland ME, Alexander KL., "Understanding the extracellular vesicle surface for clinical molecular biology," *J Extracell Vesicles*, vol. 2022, no. PMID: 36239734, doi: 10.1002/jev2.12260.

[59] Yang G et al, “Exosomes and Their Bioengineering Strategies in the Cutaneous Wound Healing and Related Complications: Current Knowledge and Future Perspectives.,” *Int J Biol Sci.*, vol. 2023, no. PMID: 37056923, doi: 10.7150/ijbs.80430.

[60] Doyle LM, Wang MZ., “Overview of Extracellular Vesicles, Their Origin, Composition, Purpose, and Methods for Exosome Isolation and Analysis.,” *Cells*, vol. 2019, no. PMID: 31311206, doi: 10.3390/cells8070727.

[61] Hinger SA, Cha DJ, Franklin JL, Higginbotham JN, Dou Y, Ping J, Shu L, Prasad N, Levy S, Zhang B, Liu Q, Weaver AM, Coffey RJ, Patton JG., “Diverse Long RNAs Are Differentially Sorted into Extracellular Vesicles Secreted by Colorectal Cancer Cells.,” *Cell Rep.*, vol. 2018, no. PMID: 30332650, doi: 10.1016/j.celrep.2018.09.054.

[62] O’Brien K, Breyne K, Ughetto S, Laurent LC, Breakefield XO., “RNA delivery by extracellular vesicles in mammalian cells and its applications.,” *Nat Rev Mol Cell Biol.*, vol. 2020, no. PMID: 32457507, doi: 10.1038/s41580-020-0251-y.

[63] Shahraki et al., “An update in the applications of exosomes in cancer theranostics: from research to clinical trials.,” *J Cancer Res Clin Oncol.*, vol. 2023, no. PMID: 37010586, doi: 10.1007/s00432-023-04701-6.

[64] Tian T, Zhu YL, Zhou YY, Liang GF, Wang YY, Hu FH, Xiao ZD., “Exosome uptake through clathrin-mediated endocytosis and macropinocytosis and mediating miR-21 delivery.,” *J Biol Chem.*, vol. 2014, no. PMID: 24951588, doi: 10.1074/jbc.M114.588046.

[65] Nanbo A, Kawanishi E, Yoshida R, Yoshiyama H., “Exosomes derived from Epstein-Barr virus-infected cells are internalized via caveola-dependent endocytosis and promote phenotypic modulation in target cells.,” *J Virol.*, vol. 2013, no. PMID: 23864627, doi: 10.1128/JVI.01310-13.

[66] Feng D, Zhao WL, Ye YY, Bai XC, Liu RQ, Chang LF, Zhou Q, Sui SF., “Cellular internalization of exosomes occurs through phagocytosis.,” *Traffic*, vol. 2010, no. PMID: 20136776, doi: 10.1111/j.1600-0854.2010.01041.x.

[67] King JS, Kay RR., “The origins and evolution of macropinocytosis.,” *Philos Trans R Soc Lond B Biol Sci.*, vol. 2019, no. PMID: 30967007, doi: 10.1098/rstb.2018.0158.

[68] Christianson HC, Svensson KJ, van Kuppevelt TH, Li JP, Belting M., “Cancer cell exosomes depend on cell-surface heparan sulfate proteoglycans for their internalization and functional activity.,” *Proc Natl Acad Sci U S A.*, vol. 2013, no. PMID: 24101524, doi: 10.1073/pnas.1304266110.

[69] Mulcahy LA, Pink RC, Carter DR., "Routes and mechanisms of extracellular vesicle uptake.," *J Extracell Vesicles.*, vol. 2014, no. PMID: 25143819, doi: 10.3402/jev.v3.24641.

[70] Samii A, Razmkhah F., "Transformation of Hematopoietic Stem and Progenitor Cells by Leukemia Extracellular Vesicles: A Step Toward Leukemogenesis.," *Stem Cell Rev Rep.*, vol. 2020, no. PMID: 32500481, doi: 10.1007/s12015-020-09975-8.

[71] Rappa G, Santos MF, Green TM, Karbanová J, Hassler J, Bai Y, Barsky SH, Corbeil D, Lorico A, "Nuclear transport of cancer extracellular vesicle-derived biomaterials through nuclear envelope invagination-associated late endosomes," *Oncotarget*, vol. PMID: 28129640, 2017, doi: DOI:%2010.18632/oncotarget.14804.

[72] Santos MF, Rappa G, Karbanová J, Kurth T, Corbeil D, Lorico A, "VAMP-associated protein-A and oxysterol-binding protein-related protein 3 promote the entry of late endosomes into the nucleoplasmic reticulum," *J Biol Chem*, vol. PMID: 30018135, 2018, doi: 10.1074/jbc.RA118.003725.

[73] Corbeil D et al., "Uptake and Fate of Extracellular Membrane Vesicles: Nucleoplasmic Reticulum-Associated Late Endosomes as a New Gate to Intercellular Communication.," *Cells*, vol. 2020, no. PMID: 32825578, doi: 10.3390/cells9091931.

[74] Kurian TK, Banik S, Gopal D, Chakrabarti S, Mazumder N., "Elucidating Methods for Isolation and Quantification of Exosomes: A Review.," *Mol Biotechnol.*, vol. 2021, no. PMID: 33492613, doi: 10.1007/s12033-021-00300-3.

[75] Théry C, Witwer KW, et al., "Minimal information for studies of extracellular vesicles 2018 (MISEV2018): a position statement of the International Society for Extracellular Vesicles and update of the MISEV2014 guidelines.," *J Extracell Vesicles.*, vol. 2018, no. PMID: 30637094, doi: 10.1080/20013078.2018.1535750.

[76] Meggiolaro A, Moccia V, Brun P, Pierno M, Mistura G, Zappulli V, Ferraro D., "Microfluidic Strategies for Extracellular Vesicle Isolation: Towards Clinical Applications.," *Biosensors (Basel)*, vol. 2022, no. PMID: 36671885, doi: 10.3390/bios13010050.

[77] De Sousa KP, Rossi I, Abdullahi M, Ramirez MI, Stratton D, Inal JM., "Isolation and characterization of extracellular vesicles and future directions in diagnosis and therapy.," *Wiley Interdiscip Rev Nanomed Nanobiotechnol.*, vol. 2023, no. PMID: 35898167, doi: 10.1002/wnan.1835.

[78] Böing AN, van der Pol E, Grootemaat AE, Coumans FA, Sturk A, Nieuwland R., "Single-step isolation of extracellular vesicles by size-exclusion chromatography.," *J Extracell Vesicles.*, vol. 2014, no. PMID: 25279113, doi: 10.3402/jev.v3.23430.

[79] Lobb R, Möller A., "Size Exclusion Chromatography: A Simple and Reliable Method for Exosome Purification," *Methods Mol Biol.*, vol. 2017, no. PMID: 28828651, doi: 10.1007/978-1-4939-7253-1_9.

[80] Peng L, Xu Q, Yin S, Zhang Y, Wu H, Liu Y, Chen L, Hu Y, Yuan J, Peng K, Lin Q., "The emerging nanomedicine-based technology for non-small cell lung cancer immunotherapy: how far are we from an effective treatment.," *Front Oncol.*, vol. 2023, no. PMID: 37182180, doi: 10.3389/fonc.2023.1153319.

[81] Wishard A, Gibb BC., "Dynamic Light Scattering - an all-purpose guide for the supramolecular chemist.," *Supramol Chem.*, vol. 2019, no. PMID: 34675465, doi: 10.1080/10610278.2019.1629438.

[82] Gross J, Sayle S, Karow AR, Bakowsky U, Garidel P., "Nanoparticle tracking analysis of particle size and concentration detection in suspensions of polymer and protein samples: Influence of experimental and data evaluation parameters.," *Eur J Pharm Biopharm.*, vol. 2016, no. PMID: 27108267, doi: 10.1016/j.ejpb.2016.04.013.

[83] Cizmar P, Yuana Y., "Detection and Characterization of Extracellular Vesicles by Transmission and Cryo-Transmission Electron Microscopy.," *Methods Mol Biol.*, vol. 2017, no. PMID: 28828660, doi: 10.1007/978-1-4939-7253-1_18.

[84] Lötvall J, Hill AF, Hochberg F, Buzás EI, Di Vizio D, Gardiner C, Gho YS, Kurochkin IV, Mathivanan S, Quesenberry P, Sahoo S, Tahara H, Wauben MH, Witwer KW, Théry C., "Minimal experimental requirements for definition of extracellular vesicles and their functions: a position statement from the International Society for Extracellular Vesicles.," *J Extracell Vesicles.*, vol. 2014, no. PMID: 25536934, doi: 10.3402/jev.v3.26913.

[85] Shao Y, Chen T, Zheng X, Yang S, Xu K, Chen X, Xu F, Wang L, Shen Y, Wang T, Zhang M, Hu W, Ye C, Yu X, Shao J, Zheng S., "Colorectal cancer-derived small extracellular vesicles establish an inflammatory premetastatic niche in liver metastasis.," *Carcinogenesis*, vol. 2018, no. PMID: 30184100, doi: 0.1093/carcin/bgy115.

[86] Hoshino A, Costa-Silva B, et al., "Tumour exosome integrins determine organotropic metastasis.," *Nature*, vol. 2015, no. PMID: 26524530, doi: 10.1038/nature15756.

[87] Costa-Silva B, Aiello NM, Ocean AJ, Singh S, Zhang H, Thakur BK, Becker A, Hoshino A, Mark MT, Molina H, Xiang J, Zhang T, Theilen TM, García-Santos G, Williams C, Ararso Y, Huang Y, Rodrigues G, Shen TL, Labori KJ, Lothe IM, Kure EH, Hernandez

J, Doussot A, Ebbesen SH, Grandgenett PM, Hollingsworth MA, Jain M, Mallya K, Batra SK, Jarnagin WR, Schwartz RE, Matei I, Peinado H, Stanger BZ, Bromberg J, Lyden D., "Pancreatic cancer exosomes initiate pre-metastatic niche formation in the liver.," *Nat Cell Biol.*, vol. 2015, no. PMID: 25985394, doi: 10.1038/ncb3169.

[88] Pucci M, Raimondo S, Urzì O, Moschetti M, Di Bella MA, Conigliaro A, Caccamo N, La Manna MP, Fontana S, Alessandro R., "Tumor-Derived Small Extracellular Vesicles Induce Pro-Inflammatory Cytokine Expression and PD-L1 Regulation in M0 Macrophages via IL-6/STAT3 and TLR4 Signaling Pathways.," *Int J Mol Sci.*, vol. 2021, no. PMID: 34829995, doi: 10.3390/ijms222212118.

[89] Brodt P., "Role of the Microenvironment in Liver Metastasis: From Pre- to Prometastatic Niches.," *Clin Cancer Res.*, vol. 2016, no. PMID: 27797969, doi: 10.1158/1078-0432.CCR-16-0460.

[90] Pucci M, Moschetti M, Urzì O, Loria M, Conigliaro A, Di Bella MA, Crescitelli R, Olofsson Bagge R, Gallo A, Santos MF, Puglisi C, Forte S, Lorico A, Alessandro R, Fontana S., "Colorectal cancer-derived small extracellular vesicles induce TGFβ1-mediated epithelial to mesenchymal transition of hepatocytes.," *Cancer Cell Int. 2023 Apr 18;23(1):77.*, doi: doi:%2010.1186/s12935-023-02916-8.

[91] William M. S. Russell and Rex L. Burch, "The Principles of Humane Experimental Technique," in *London: Methuen, 1959*.

[92] Urzì O, Gasparro R, Costanzo E, De Luca A, Giavaresi G, Fontana S, Alessandro R., "Three-Dimensional Cell Cultures: The Bridge between In Vitro and In Vivo Models.," *Int J Mol Sci.*, vol. 2023, no. PMID: 37569426, doi: 10.3390/ijms241512046.

[93] Sutherland RM, Inch WR, McCredie JA, Kruuv J., "A multi-component radiation survival curve using an in vitro tumour model.," *Int J Radiat Biol Relat Stud Phys Chem Med.*, vol. 1970, no. PMID: 5316564, doi: 10.1080/09553007014551401.

[94] Gunti S, Hoke ATK, Vu KP, London NR Jr., "Organoid and Spheroid Tumor Models: Techniques and Applications.," *Cancers (Basel).*, vol. 2021, no. PMID: 33669619, doi: 10.3390/cancers13040874.

[95] Cox CR, Lynch S, Goldring C, Sharma P., "Current Perspective: 3D Spheroid Models Utilizing Human-Based Cells for Investigating Metabolism-Dependent Drug-Induced Liver Injury.," *Front Med Technol.*, vol. 2020, no. PMID: 35047893, doi: 10.3389/fmedt.2020.611913.

[96] Mehta G, Hsiao AY, Ingram M, Luker GD, Takayama S., "Opportunities and challenges for use of tumor spheroids as models to test drug delivery and efficacy.," *J Control Release.*, vol. 2012, no. PMID: 22613880, doi: 10.1016/j.jconrel.2012.04.045.

[97] Sato K, Zhang W, Safarikia S, Isidan A, Chen AM, Li P, Francis H, Kennedy L, Baiocchi L, Alvaro D, Glaser S, Ekser B, Alpini G., "Organoids and Spheroids as Models for Studying Cholestatic Liver Injury and Cholangiocarcinoma.," *Hepatology*, vol. 2021, no. PMID: 33222247, doi: 10.1002/hep.31653.

[98] Ryu NE, Lee SH, Park H., "Spheroid Culture System Methods and Applications for Mesenchymal Stem Cells.," *Cells*, vol. 2019, no. PMID: 31842346, doi: 10.3390/cells8121620.

[99] Birey F, Andersen J, Makinson CD, Islam S, Wei W, Huber N, Fan HC, Metzler KRC, Panagiotakos G, Thom N, O'Rourke NA, Steinmetz LM, Bernstein JA, Hallmayer J, Huguenard JR, Paşca SP., "Assembly of functionally integrated human forebrain spheroids.," *Nature*, vol. 2017, no. PMID: 28445465, doi: 10.1038/nature22330.

[100] Dinh PC, Paudel D, Brochu H, Popowski KD, Gracieux MC, Cores J, Huang K, Hensley MT, Harrell E, Vandergriff AC, George AK, Barrio RT, Hu S, Allen TA, Blackburn K, Caranasos TG, Peng X, Schnabel LV, Adler KB, Lobo LJ, Goshe MB, Cheng K., "Inhalation of lung spheroid cell secretome and exosomes promotes lung repair in pulmonary fibrosis.," *Nat Commun.*, vol. 2020, no. PMID: 32111836, doi: 10.1038/s41467-020-14344-7.

[101] Koblenzer M, Weiler M, Fragoulis A, Rütten S, Pufe T, Jahr H., "Physiological Mineralization during In Vitro Osteogenesis in a Biomimetic Spheroid Culture Model.," *Cells*, vol. 2022, no. PMID: 36078105, doi: 10.3390/cells11172702.

[102] Han K, Pierce SE, Li A, Spees K, Anderson GR, Seoane JA, Lo YH, Dubreuil M, Olivas M, Kamber RA, Wainberg M, Kostyrko K, Kelly MR, Yousefi M, Simpkins SW, Yao D, Lee K, Kuo CJ, Jackson PK, Sweet-Cordero A, Kundaje A, Gentles AJ, Curtis C, Winslow MM, Bassik MC., "CRISPR screens in cancer spheroids identify 3D growth-specific vulnerabilities.," *Nature*, vol. 2020, no. PMID: 32238925, doi: 10.1038/s41586-020-2099-x.

[103] Hwang HJ, Oh MS, Lee DW, Kuh HJ., "Multiplex quantitative analysis of stroma-mediated cancer cell invasion, matrix remodeling, and drug response in a 3D co-culture model of pancreatic tumor spheroids and stellate cells.," *J Exp Clin Cancer Res.*, vol. 2019, no. PMID: 31200779, doi: 10.1186/s13046-019-1225-9.

[104] Courau T, Bonnereau J, Chicoteau J, Bottois H, Remark R, Assante Miranda L, Toubert A, Blery M, Aparicio T, Allez M, Le Bourhis L., "Cocultures of human colorectal tumor spheroids with immune cells reveal the therapeutic potential of MICA/B and NKG2A targeting for cancer treatment.," *J Immunother Cancer.*, vol. 2019, no. PMID: 30871626, doi: 10.1186/s40425-019-0553-9.

[105] Ingelman-Sundberg M, Lauschke VM., "3D human liver spheroids for translational pharmacology and toxicology," *Basic Clin Pharmacol Toxicol.*, vol. 2022, no. PMID: 33872466., doi: 10.1111/bcpt.13587.

[106] Yoo S, Lee HJ., "Spheroid-Hydrogel-Integrated Biomimetic System: A New Frontier in Advanced Three-Dimensional Cell Culture Technology.," *Cells Tissues Organs*, vol. 2025, no. PMID: 39265553, doi: 10.1159/000541416.

[107] Chae S, Hong J, Hwangbo H, Kim G., "The utility of biomedical scaffolds laden with spheroids in various tissue engineering applications.," *Theranostics*, vol. 2021, no. PMID: 34093855, doi: 10.7150/thno.58421.

[108] Park H, Seo YK, Arai Y, Lee SH., "Physicochemical Modulation Strategies for Mass Production of Extracellular Vesicle.," *Tissue Eng Regen Med.*, vol. 2025, no. PMID: 40471522, doi: 10.1007/s13770-025-00726-9.

[109] Casajuana Ester M, Day RM., "Production and Utility of Extracellular Vesicles with 3D Culture Methods.," *Pharmaceutics*, vol. 2023, no. PMID: 36839984, doi: 0.3390/pharmaceutics15020663.

[110] Lauschke VM, Shafagh RZ, Hendriks DFG, Ingelman-Sundberg M., "3D Primary Hepatocyte Culture Systems for Analyses of Liver Diseases, Drug Metabolism, and Toxicity: Emerging Culture Paradigms and Applications.," *Biotechnol J.*, vol. 2019, no. PMID: 30957976, doi: 10.1002/biot.201800347.

[111] Bell CC, Dankers ACA, Lauschke VM, Sison-Young R, Jenkins R, Rowe C, Goldring CE, Park K, Regan SL, Walker T, Schofield C, Baze A, Foster AJ, Williams DP, van de Ven AWM, Jacobs F, Houdt JV, Lähteenmäki T, Snoeys J, Juhila S, Richert L, Ingelman-Sundberg M., "Comparison of Hepatic 2D Sandwich Cultures and 3D Spheroids for Long-term Toxicity Applications:A Multicenter Study," *Toxicol Sci.*, vol. 2018, no. PMID: 29329425, doi: 10.1093/toxsci/kfx289.

[112] Bell CC, Hendriks DF, Moro SM, Ellis E, Walsh J, Renblom A, Fredriksson Puigvert L, Dankers AC, Jacobs F, Snoeys J, Sison-Young RL, Jenkins RE, Nordling Å, Mkrtchian S, Park BK, Kitteringham NR, Goldring CE, Lauschke VM, Ingelman-Sundberg M., "Characterization of primary human hepatocyte spheroids as a model system for drug-

induced liver injury, liver function and disease.," *Sci Rep.*, vol. 2016, no. PMID: 27143246, doi: 10.1038/srep25187.

[113] Kozyra M, Johansson I, Nordling Å, Ullah S, Lauschke VM, Ingelman-Sundberg M., "Human hepatic 3D spheroids as a model for steatosis and insulin resistance.," *Sci Rep.*, vol. 2018, no. PMID: 30250238, doi: 10.1038/s41598-018-32722-6.

[114] Tostões RM, Leite SB, Serra M, Jensen J, Björquist P, Carrondo MJ, Brito C, Alves PM., "Human liver cell spheroids in extended perfusion bioreactor culture for repeated-dose drug testing.," *Hepatology*, vol. 2012, no. PMID: 22031499, doi: 10.1002/hep.24760.

[115] Shibuya K, Watanabe M, Goto R, Zaitsu M, Ganchiku Y, Taketomi A., "The Efficacy of the Hepatocyte Spheroids for Hepatocyte Transplantation.," *Cell Transplant.*, vol. 2021, no. PMID: 33900126, doi: 10.1177/09636897211000014.

[116] Gwon K, Choi D, de Hoyos-Vega JM, Baskaran H, Gonzalez-Suarez AM, Lee S, Hong HJ, Nguyen KM, Dharmesh E, Sugahara G, Ishida Y, Saito T, Stybayeva G, Revzin A., "Function of hepatocyte spheroids in bioactive microcapsules is enhanced by endogenous and exogenous hepatocyte growth factor.," *Bioact Mater.*, vol. 2023, no. PMID: 37266448, doi: 10.1016/j.bioactmat.2023.05.009.

[117] *Hamilton F. An account of the fishes found in the river Ganges and its branches. London: Constable & Co.; 1822*.

[118] Yubin Liu, Dongliang Li, Zhen Yuan, "Photoacoustic Tomography Imaging of the Adult Zebrafish by Using Unfocused and Focused High-Frequency Ultrasound Transducers," *Appl. Sci.*, vol. 2016, doi: 10.3390/app6120392.

[119] Streisinger G, Walker C, Dower N, Knauber D, Singer F., "Production of clones of homozygous diploid zebra fish (Brachydanio rerio).," *Nature*, vol. 1981, no. PMID: 7248006, doi: 10.1038/291293a0.

[120] Hyenne V, Ghoroghi S, Collot M, Bons J, Follain G, Harlepp S, Mary B, Bauer J, Mercier L, Busnelli I, Lefebvre O, Fekonja N, Garcia-Leon MJ, Machado P, Delalande F, López AA, Silva SG, Verweij FJ, van Niel G, Djouad F, Peinado H, Carapito C, Klymchenko AS, Goetz JG., "Studying the Fate of Tumor Extracellular Vesicles at High Spatiotemporal Resolution Using the Zebrafish Embryo.," *Dev Cell.*, vol. 2019, no. PMID: 30745140, doi: 10.1016/j.devcel.2019.01.014.

[121] Verdi V, Bécot A, van Niel G, Verweij FJ., "In vivo imaging of EVs in zebrafish: New perspectives from 'the waterside'.," *FASEB Bioadv. ì*, vol. 2021, no. PMID: 34761174, doi: 10.1096/fba.2021-00081.

[122] Shimizu N, Shiraishi H, Hanada T., “Zebrafish as a Useful Model System for Human Liver Disease.,” *Cells*, vol. 2023, no. PMID: 37759472, doi: 10.3390/cells12182246.

[123] von Hellfeld, Rebecca & Brotzmann, Katharina & Baumann, Lisa & Strecker, Ruben & Braunbeck, Thomas., “Adverse effects in the fish embryo acute toxicity (FET) test: a catalogue of unspecific morphological changes versus more specific effects in zebrafish (Danio rerio) embryos,” *Environmental Sciences Europe*, vol. 2020, doi: 10.1186/s12302-020-00398-3.

[124] Choe CP, Choi SY, Kee Y, Kim MJ, Kim SH, Lee Y, Park HC, Ro H., “Transgenic fluorescent zebrafish lines that have revolutionized biomedical research.,” *Lab Anim Res.*, no. PMID: 34496973, doi: 10.1186/s42826-021-00103-2.

[125] Li N, Felber K, Elks P, Croucher P, Roehl HH., “Tracking gene expression during zebrafish osteoblast differentiation.,” *Dev Dyn.*, vol. 2009, no. PMID: 19161246, doi: 10.1002/dvdy.21838.

[126] Nguyen AT, Emelyanov A, Koh CH, Spitsbergen JM, Lam SH, Mathavan S, Parinov S, Gong Z., “A high level of liver-specific expression of oncogenic Kras(V12) drives robust liver tumorigenesis in transgenic zebrafish.,” *Dis Model Mech.*, vol. 2011, no. PMID: 21729876, doi: 10.1242/dmm.007831.

[127] Bambino K, Morrison J, Chu J., “Hepatotoxicity in Zebrafish Larvae,” *Methods Mol Biol.*, vol. 2019, no. PMID: 31069672, doi: 10.1007/978-1-4939-9182-2_9.

[128] Costa B, Estrada MF, Gomes A, Fernandez LM, Azevedo JM, Póvoa V, Fontes M, Alves A, Galzerano A, Castillo-Martin M, Herrando I, Brandão S, Carneiro C, Nunes V, Carvalho C, Parvaiz A, Marreiros A, Fior R., “Zebrafish Avatar-test forecasts clinical response to chemotherapy in patients with colorectal cancer.,” *Nat Commun.*, vol. 2024, no. PMID: 38839755, doi: 10.1038/s41467-024-49051-0.

[129] Cornet C, Dyballa S, Terriente J, Di Giacomo V., “ZeOncoTest: Refining and Automating the Zebrafish Xenograft Model for Drug Discovery in Cancer.,” *Pharmaceuticals (Basel).*, vol. 2019, no. PMID: 31878274, doi: 10.3390/ph13010001.

[130] MJ Vis Exp. artinez-Lopez M, Póvoa V, Fior R., “Generation of Zebrafish Larval Xenografts and Tumor Behavior Analysis.,” *2021*, vol. PMID: 34223839, doi: 10.3791/62373.

[131] Verweij FJ, Revenu C, Arras G, Dingli F, Loew D, Pegtel DM, Follain G, Allio G, Goetz JG, Zimmermann P, Herbomel P, Del Bene F, Raposo G, van Niel G., “Live Tracking of Inter-organ Communication by Endogenous Exosomes In Vivo.,” *Dev Cell.*, vol. 2019, no. PMID: 30745143, doi: 10.1016/j.devcel.2019.01.004.

[132] Mühlbauer M, Fleck M, Schütz C, Weiss T, Froh M, Blank C, Schölmerich J, Hellerbrand C., "PD-L1 is induced in hepatocytes by viral infection and by interferon-alpha and -gamma and mediates T cell apoptosis.," *J Hepatol.*, vol. 2006, no. PMID: 16876901, doi: 10.1016/j.jhep.2006.05.007.

[133] Qu QX, Xie F, Huang Q, Zhang XG, "Membranous and Cytoplasmic Expression of PD-L1 in Ovarian Cancer Cells," *Cell Physiol Biochem*, vol. 2017, no. PMID: 29055949, doi: 10.1159/000484109.

[134] Ukpo OC, Thorstad WL, Lewis JS Jr., "B7-H1 expression model for immune evasion in human papillomavirus-related oropharyngeal squamous cell carcinoma," *Head Neck Pathol*, vol. 2013, no. PMID: 23179191, doi: 10.1007/s12105-012-0406-z.

[135] Gao Y, Nihira NT, Bu X, Chu C, Zhang J, Kolodziejczyk A, Fan Y, Chan NT, Ma L, Liu J, Wang D, Dai X, Liu H, Ono M, Nakanishi A, Inuzuka H, North BJ, Huang YH, Sharma S, Geng Y, Xu W, Liu XS, Li L, Miki Y, Sicinski P, Freeman GJ, Wei W., "Acetylation-dependent regulation of PD-L1 nuclear translocation dictates the efficacy of anti-PD-1 immunotherapy," *Nat Cell Biol*, vol. PMID: 32839551, 2020, doi: doi:%2010.1038/s41556-020-0562-4.

[136] Wu F, Gu Y, Kang B, Heskia F, Pachot A, Bonneville M, Wei P, Liang J., "PD-L1 detection on circulating tumor-derived extracellular vesicles (T-EVs) from patients with lung cancer," *Transl Lung Cancer Res*, vol. 2021, no. PMID: 34295653, doi: 10.21037/tlcr-20-1277.

[137] Santos MF, Rappa G, Karbanová J, Fontana S, Bella MAD, Pope MR, Parrino B, Cascioferro SM, Vistoli G, Diana P, Cirrincione G, Arena GO, Woo G, Huang K, Huynh T, Moschetti M, Alessandro R, Corbeil D, Lorico A, "Itraconazole inhibits nuclear delivery of extracellular vesicle cargo by disrupting the entry of late endosomes into the nucleoplasmic reticulum," *J Extracell Vesicles.*, vol. PMID: 34429859, 2021, doi: 10.1002/jev2.12132.

[138] Urzì O, Olofsson Bagge R, Crescitelli R., "The dark side of foetal bovine serum in extracellular vesicle studies.," *J Extracell Vesicles*, vol. 2022, no. PMID: 36214482, doi: 10.1002/jev2.12271.

[139] Théry C, Amigorena S, Raposo G, Clayton A, "Isolation and characterization of exosomes from cell culture supernatants and biological fluids," *Curr Protoc Cell Biol*, vol. 2006, no. PMID: 18228490, doi: 10.1002/0471143030.cb0322s30.

[140] Watt AJ, Garrison WD, Duncan SA., “HNF4: a central regulator of hepatocyte differentiation and function.,” *Hepatology. 2003 Jun;37(6):1249-53.*, doi: doi:%2010.1053/jhep.2003.50273.

[141] Acharya P, Chouhan K, Weiskirchen S, Weiskirchen R., “Cellular Mechanisms of Liver Fibrosis.,” *Front Pharmacol. 2021 May 6;12:671640.*, doi: doi:%2010.3389/fphar.2021.671640.

[142] Bhattacharyya S, Midwood KS, Varga J., “Tenascin-C in fibrosis in multiple organs: Translational implications.,” *Semin Cell Dev Biol. 2022 Aug;128:130-136.*, doi: doi:%2010.1016/j.semcdb.2022.03.019.

[143] Li Y, Zhao J, Yin Y, Li K, Zhang C, Zheng Y., “The Role of IL-6 in Fibrotic Diseases: Molecular and Cellular Mechanisms.,” *Int J Biol Sci. 2022 Aug 29;18(14):5405-5414.*, doi: doi:%2010.7150/ijbs.75876.

[144] Bárcena C, Stefanovic M, Tutusaus A, Joannas L, Menéndez A, García-Ruiz C, Sancho-Bru P, Marí M, Caballeria J, Rothlin CV, Fernández-Checa JC, de Frutos PG, Morales A., “Gas6/Axl pathway is activated in chronic liver disease and its targeting reduces fibrosis via hepatic stellate cell inactivation.,” *J Hepatol. 2015 Sep;63(3):670-8.*, doi: doi:%2010.1016/j.jhep.2015.04.013.

[145] Xu F, Liu C, Zhou D, Zhang L., “TGF-β/SMAD Pathway and Its Regulation in Hepatic Fibrosis.,” *J Histochem Cytochem. 2016 Mar;64(3):157-67.*, doi: doi:%2010.1369/0022155415627681.

[146] Lai CP, Kim EY, Badr CE, Weissleder R, Mempel TR, Tannous BA, Breakefield XO, “Visualization and tracking of tumour extracellular vesicle delivery and RNA translation using multiplexed reporters,” *Nat Commun*, vol. 2015, no. PMID: 25967391, doi: 10.1038/ncomms8029.

[147] Metsäniitty M, Hasnat S, Öhman C, Salo T, Eklund KK, Oscarsson J, Salem A, “Zebrafish larvae as a model for studying the impact of oral bacterial vesicles on tumor cell growth and metastasis,” *Hum Cell*, vol. 2024, no. PMID: 39138804, doi: 10.1007/s13577-024-01114-6.

[148] Camilla Maria Fontana, Hien Van Doan, “Zebrafish xenograft as a tool for the study of colorectal cancer: a review,” *Cell Death Dis*, vol. 2024, no. PMID: 38195619, doi: 10.1038/s41419-023-06291-0.

Aknowledgements

My PhD has been an incredible journey, and I have cherished every single moment of it. At the beginning, I felt a mix of enthusiasm and uncertainty about myself. Today, I am proud to say that while some insecurities remain, my enthusiasm has never faded. For this growth, I owe my deepest thanks to many extraordinary people.

First and foremost, I would like to express my sincere gratitude to Prof. Simona Fontana, my mentor throughout these years. Her guidance has been fundamental not only for this important project, but also for my personal growth, teaching me how to embrace my flaws and to accept that not everything is under my control.

A heartfelt thank you goes to Dr. Marzia Pucci. Her unique combination of guidance and friendship has been invaluable. Her advice, both in research and in life, made these three years much more manageable, and I owe her so much.

A special and sencere thank you goes to Prof. Riccardo Alessandro, who welcomed me into this wonderful lab. His constant presence, support, and encouragement to always take the next step meant a lot to me and to my research.

A huge thanks to my brothers Marcuccio and Peppino, my companions throughout these years. Thank you for teaching me that difficult moments exist, but that having good friends by your side truly makes the difference.

A big thank you to Vichi for staying by my side through both good and bad times, sharing laughter and tears.

A special thank you to Gabriele, first my trainee, then my friend, and eventually some sort of brother-in-law. Thank you for supporting me with your balanced presence, profound, and light at the same time.

I would like to thank Prof. Alice Conigliaro, Prof. Chiara Corrado, Prof. Stefania Raimondo, Nima, Robi, Giuli, Giuliana, Anto, Marti, Deni, Aurora, and every member of the lab for making my time in Via Divisi truly unforgettable.

A special thank you goes to Fred, for being such an important part of this journey, even if only for a short time. Thank you for being such a great mentor at the beginning and such a dear friend in the end.

A sencere thank you to Bárbara, my work wife, for taking care of me when I needed it the most and for inspiring me in becoming a kind person and a rigorous scientist.

A special thank you to Lenny and Daan, my *Drankjes Doen* mates. Thank you for introducing me to a new version of myself that I will never forget or let go of.

A huge thank you to Anna, Jelle, Misko, and all the members of Frederik's lab for welcoming me so warmly and for the beautiful moments we shared together.

A special thank you to Giulione, by my side since our Master's degree, and now defending our PhDs together. I wish to both of us that this is only the beginning.

Thank you to Peppe, a lifelong friend, sitting next to me in the front row back at school, and side by side again today, even though life now has a different rhythm and flavor.

A special thank you to Amelia, Sergio, Flavia, and Ivan, whose love, care, and support throughout these years have meant so much to me. Thank you for celebrating my successes and for standing by me through my failures.

A heartfelt thank you to my family, my mom, my dad, and my sister, for understanding that being happy and loving what I do was the most important thing, and for supporting me when I felt like that was not enough.

Last, but certainly not least, thank you Richi, for your quiet support, for never trying to fix me but simply staying close while I learned how to do it myself. These years have been a roller coaster, thank you for never getting off and for doing so with a smile and deep love that I return with all of myself.